RICE UNIVERSITY

Development and Evaluation of Approaches for Quantitative Optical Molecular Imaging of Neoplasia

by

Kelsey Jane Rosbach

A THESIS SUBMITTED
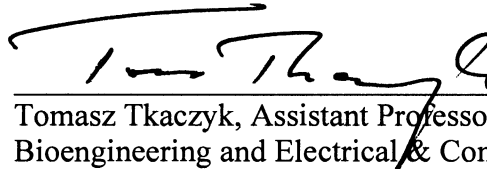IN PARTIAL FULFILLMENT OF THE
REQUIREMENTS FOR THE DEGREE
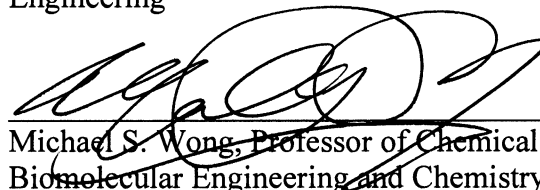
Doctor of Philosophy

APPROVED, THESIS COMMITTEE:

Rebecca R. Richards-Kortum, Chair
Stanley C. Moore Professor of Bioengineering
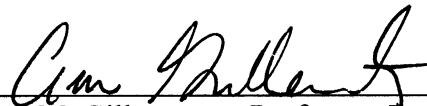
Tomasz Tkaczyk, Assistant Professor of
Bioengineering and Electrical & Computer
Engineering

Michael S. Wong, Professor of Chemical and
Biomolecular Engineering and Chemistry

Ann M. Gillenwater, Professor, Department of
Head and Neck Surgery, Division of Surgery, The
University of Texas MD Anderson Cancer Center

HOUSTON, TEXAS
May, 2011

ABSTRACT

Development and Evaluation of Approaches for Quantitative Optical

Molecular Imaging of Neoplasia

by

Kelsey Jane Rosbach

This thesis develops and evaluates three approaches for quantitative molecularly-targeted optical imaging of neoplasia. The first approach focuses on widefield imaging of biomarkers near the tissue surface for early detection applications; this approach is demonstrated in freshly resected oral tissue. Most oral cancers are not detected until the disease has spread, but topical application of targeted imaging agents allows rapid visualization of biomarker expression, giving real-time, objective information. Epidermal growth factor receptor (EGFR) expression was quantified in patient samples using fluorescent epidermal growth factor. Dysplasia (n=4) and cancer (n=13) had an average 2.3-fold and 3.8-fold increase in signal compared to normal tissue. EGFR expression was assessed along with metabolic activity using a fluorescent glucose analog, 2-NBDG, in 9 patient samples. A classification algorithm using quantitative image features resulted in an area under the curve (AUC) of 0.83, though the main advantage of this technique may be to understand spatial heterogeneity of biomarker expression and how this correlates with disease.

The next approach focuses on high-resolution optical imaging through a needle to detect metastases in lymphoid tissue for clinical staging applications; this approach is

demonstrated in resected lymph nodes from breast cancer patients. These patients often require removal of nodes, but an optical imaging strategy using topical application of imaging agents in vivo may classify nodes as normal or metastatic, thus reducing unnecessary removal of normal nodes and improving metastasis detection. Proflavine, a nuclear dye, was topically applied to 43 nodes. A classification algorithm developed from quantitative image features distinguished normal lymphoid tissue from metastases with an AUC of 0.84.

Because optical imaging is depth limited, the final approach combines high-resolution optical imaging with magnetic resonance imaging (MRI) for multimodal evaluation of deep tissue. An imaging agent functional in both optical and MRI was developed by co-loading fluorescent EGFR antibodies and gadolinium-based contrast agents in silicon discs. These discs accumulate in tumors, resulting in localized delivery of imaging agents.

The research presented here can be applied to understanding tumor biology and biomarker heterogeneity, with the future clinical goal of improving identification of disease and determination of appropriate therapy for cancer patients.

ACKNOWLEDGEMENTS

I would like to thank my parents for always encouraging my education – they have supported me and let me focus on school as my job and for that I am very grateful. But I also really appreciate them supporting me and encouraging me in other endeavors – piano lessons, soccer teams, learning to cook, and every craft project under the sun! They have helped me understand the importance of balance in my life so that I can find joy and success in aspects other than my schoolwork, which has been important in maintaining a positive attitude during my time in grad school. I'd like to thank my brother, Dan, for his encouragement and interest in how things were going at Rice; he's always been so thoughtful.

I would like to thank my friends, Mallory, Nikky, and Lori who I knew from Georgia Tech – I'm so glad you moved to Houston! And the rest of the girls night group: Nastassja and Kim, Wednesday night dinners made the week so much better! Lowrie, who believes in me so much that she has addressed postcards and letters to me as "Dr. Kelsey" ever since my first semester in grad school, thank you so much! Nadhi has been a constant support in the lab, thank you for always being willing to proofread my writing or listen to me complain or eat lunch with me, your friendship has definitely made my experience much more enjoyable. Thanks also to the rest of the lab members for long mornings spent waiting for tissue samples, for lunch conversations, or feedback during meetings – the collaborative environment (and sense of humor) was always so helpful!

Thanks to Chris Gemmiti, who taught me that my grades don't have to be perfect to get into grad school, helped me with my application, and has believed in me since then. Thanks to Colin, who encourages me when I need it and distracts me when I need

it, and accepted the months I spent away in Connecticut without a fuss. Thanks to Bill McLaughlin (and Josh MacHattan who invited me to the Carestream dinner!), who was interested in my research and found a way for me to come to Woodbridge for an industrial internship.

And finally, I would like to thank Rebecca – she is such an amazing role model and I still don't know how she does it all. Thank you for all the guidance you've given me over the years. You always have the best advice on questions from paper organization to work/life balance to big picture goals – thank you for looking out for me and making sure I stayed on track with interesting, attainable projects. I have learned so much during my time in the lab, and appreciate the time you've spent with me to help me develop critical thinking skills that I will use the rest of my life!

TABLE OF CONTENTS

LIST OF FIGURES

LIST OF TABLES

CHAPTER 1: INTRODUCTION

1.1 Project Overview

This thesis develops and evaluates approaches for quantitative molecularly-targeted optical imaging of dysplasia and cancer. The first approach focuses on widefield optical imaging of biomarkers near the tissue surface for early detection applications. The next approach focuses on high-resolution optical imaging through a needle to detect metastases in lymphoid tissue for clinical staging applications. The final approach combines high-resolution optical imaging with magnetic resonance imaging (MRI) for multimodal evaluation of tumors far below the tissue surface.

The problem of cancer cannot be overstated: the World Health Organization (WHO) reports that cancer killed 7.6 million people in 2005, accounting for over 13% of total deaths worldwide and making it a major global health problem [1]. This thesis demonstrates applications of optical imaging with molecularly-targeted contrast agents in clinical samples from two types of tissue: first in oral mucosa from oral squamous cell carcinoma patients, and next in lymph nodes from breast cancer patients. Development of a multimodal imaging agent is described, and future clinical applications for cancer are suggested but are not yet performed in this exploratory study.

1.2 Specific Aims

The primary goal of my research was to apply molecularly-targeted imaging agents onto relevant clinical samples in order to develop and evaluate quantitative optical imaging approaches for neoplasia. The quantitative information obtained from

fluorescence images indicated the presence of known biomarkers of dysplasia and cancer, which could then be assessed for correlations between biomarker expression and the presence of disease or examined to determine the heterogeneity of biomarker expression. To demonstrate how optical imaging with targeted contrast agents may be used as a tool for studying biomarker expression and predicting the presence of disease, the following specific aims were set:

(1) Demonstrate the potential of non-invasive topical delivery of an epidermal growth factor-Alexa 647 (EGF-Alexa 647) conjugate to image changes in epidermal growth factor receptor (EGFR) expression associated with oral neoplasia. In this aim, I performed a series of pre-clinical analyses to evaluate the optical contrast achieved following topical delivery of EGF-Alexa 647 in a variety of model systems, including cells, three dimensional tissue cultures, and intact human tissue specimens using widefield and high-resolution fluorescence imaging. Images were collected from seventeen different oral cancer patients: eight pairs of normal and abnormal biopsies and nine resected tumors were examined. The studies in this aim demonstrated that the EGF-dye conjugate could be uniformly delivered throughout the oral epithelium with a penetration depth exceeding 500 microns and incubation time of less than 30 minutes. Following EGF-Alexa 647 incubation, the presence of oral neoplasia was associated with a 1.5-6.9 fold increase in fluorescence contrast as compared to grossly normal mucosa from the same patient with both widefield and high-resolution fluorescence imaging.

(2) Map out detailed biomarker expression of both EGFR and metabolic activity in freshly resected human specimens of oral cancer and dysplasia to demonstrate concurrent visualization of multiple biomarkers, examine the heterogeneity of their

expression, and predict the presence of disease. In this aim, I topically applied both EGF-Alexa 647 and 2-NBDG (a fluorescent glucose analog used as a metabolic activity indicator) to the epithelial surface of nine patients and used widefield imaging to capture the molecularly-targeted fluorescent signal. 286 total 50 x 50 pixel-sized regions with a uniform histopathologic diagnosis ranging from normal, mild dysplasia, moderate dysplasia, and severe dysplasia to cancer were quantitatively analyzed to extract statistical features used to train a linear discriminant classification algorithm. When the developed algorithm was tested on the same set of regions, it had an area under the curve (AUC) of 0.83. When the classification algorithm was applied using a higher cut-off for posterior probability, regions of disease were predicted that contained mostly neoplasia either 99% (using a posterior probability range of 0.80-1.00) or 95% (using a posterior probability range of 0.60-0.79) of the time. This aim demonstrated a proof of concept of using information from multiple biomarkers to predict the presence of disease, and also described the potential use of understanding biomarker heterogeneity in both basic cancer research and in clinical management of cancer patients.

(3) Perform a pilot study to evaluate the potential of high-resolution fiber optic microscopy (HRFM) to identify lymph node metastases in breast cancer patients. In this aim, I collected 43 lymph nodes from 14 consenting breast cancer patients and topically applied proflavine dye to lymph nodes ex vivo to allow visualization of nuclei. 242 images were collected at 105 sites with confirmed histopathologic diagnosis. Quantitative statistical features were calculated from images, assessed with one-way ANOVA, and were used to develop a classification algorithm with the goal of objectively discriminating between normal and metastatic tissue. A classification algorithm using

mean image intensity and skewness achieved sensitivity of 79% (27/34) and specificity of 77% (55/71). This aim demonstrated the technical feasibility and diagnostic potential of HRFM with fluorescent contrast in the ex vivo evaluation of lymph nodes from breast cancer patients.

(4) Investigate the combination of previously developed molecularly-targeted optical imaging agents with contrast agents of other imaging modalities. In this aim, I co-loaded EGFR antibody conjugated to Alexa Fluor 647 along with a variety of gadolinium-based contrast agents (Gd-CAs) into small pores in silicon discs. Sequential loading of first the Gd-CA followed by the antibody-dye conjugate resulted in a multimodal contrast agent that can be detected by both optical and magnetic resonance imaging (MRI). A fluorometer was used to quantify the efficiency of antibody-dye loading for several combinations of type of Gd-CA and silicon disc pore size. The combination with the highest loading efficiency and consistency was co-loading Magnevist®, a clinically approved Gd-CA, with the antibody-dye conjugate into silicon discs with a 10 nanometer pore size. This aim characterized the combination of a molecularly-targeted optical imaging agent with a gadolinium-based MRI contrast agent that may eventually be used in multimodal imaging applications in cancer research.

1.3 Dissertation Overview

Chapters two, three and four focus on the optical imaging approach of using widefield imaging with molecularly-targeted contrast agents to look at surface biomarker expression for early detection applications in oral cancer. The second chapter provides background on the problem of oral cancer; the majority of this text appeared in my thesis proposal, but has been updated to include current literature in the field as well. This

chapter provides motivation and background for the studies applied to oral cancer, the application that represents the bulk of my research focus. The third chapter includes a paper that I published in *Neoplasia* in 2009 describing the topical application of EGF-Alexa 647 to paired biopsies and intact tissue specimens from oral cancer patients. The fourth chapter demonstrates optical molecular imaging of multiple biomarkers in epithelial neoplasia, specifically, EGFR expression and metabolic activity in oral mucosa. This chapter will form the basis of a future publication. The fifth chapter shifts focus to an optical imaging approach that uses high-resolution imaging through a needle for the application of clinical staging. It includes a paper that I published in *Biomedical Optics Express* in 2010 describing a pilot study to investigate the potential of high-resolution imaging of proflavine fluorescence to classify lymph nodes from breast cancer patients as either normal lymphoid tissue or metastatic tissue. The sixth chapter describes an imaging approach that could be applied in a deep tissue tumor setting through the development and characterization of a multimodal contrast agent for both MRI and high-resolution optical imaging. The combination of modalities helps address the depth limitations of optical imaging. The seventh chapter provides summary, conclusions and future directions for the dissertation.

CHAPTER 2: BACKGROUND: ORAL CANCER

2.1 Motivation and Significance

With over 300,000 new cases being diagnosed every year, cancer of the oral cavity is a major global health problem [2, 3]. Surveillance Epidemiology and End Results (SEER) data estimated that in 2010 in the United States alone, 36,540 new cases of oral cancer were diagnosed, and 7,880 deaths occurred due to the disease [4]. However, the majority of new oral cancer cases occur in developing countries, especially in India and other areas of Southeast Asia. In these regions, oral cancer comprises over one-third of all new malignancies and is one of the most common forms of cancer [5, 6]. The WHO estimates that oral cancer is the world's eighth most common malignancy [7]. The incidence of oral cancer has been increasing in parts of the world, and has remained fairly constant in the United States and Europe [8, 9].

In the United States, the average 5-year survival rate for all oral cancer patients has remained steady for the past 50 years at approximately 50%. However, expected survival is largely dependant on the stage at which the cancer is diagnosed and treated [10]. As shown in Figure 2-1, patients with locally confined disease have a much higher survival rate than patients with regional spread or distant metastases. Unfortunately, since early symptoms are rare, over 60% of patients with oral cancer are not diagnosed until their disease is in stage III or IV, meaning the cancer is no longer locally confined [11]. Once the disease has spread, much more aggressive treatment is required, resulting in associated morbidities that affect normal function and quality of life. The surgery required to remove a large, advanced tumor may interfere with speech, mastication, or

deglutition, and can also affect physical appearance. Survival rates are even lower in the developing world, and the associated morbidities of treatment cannot be dealt with as effectively. Therefore, earlier detection of oral cancer has the potential to dramatically improve survival and quality of life for all patients.
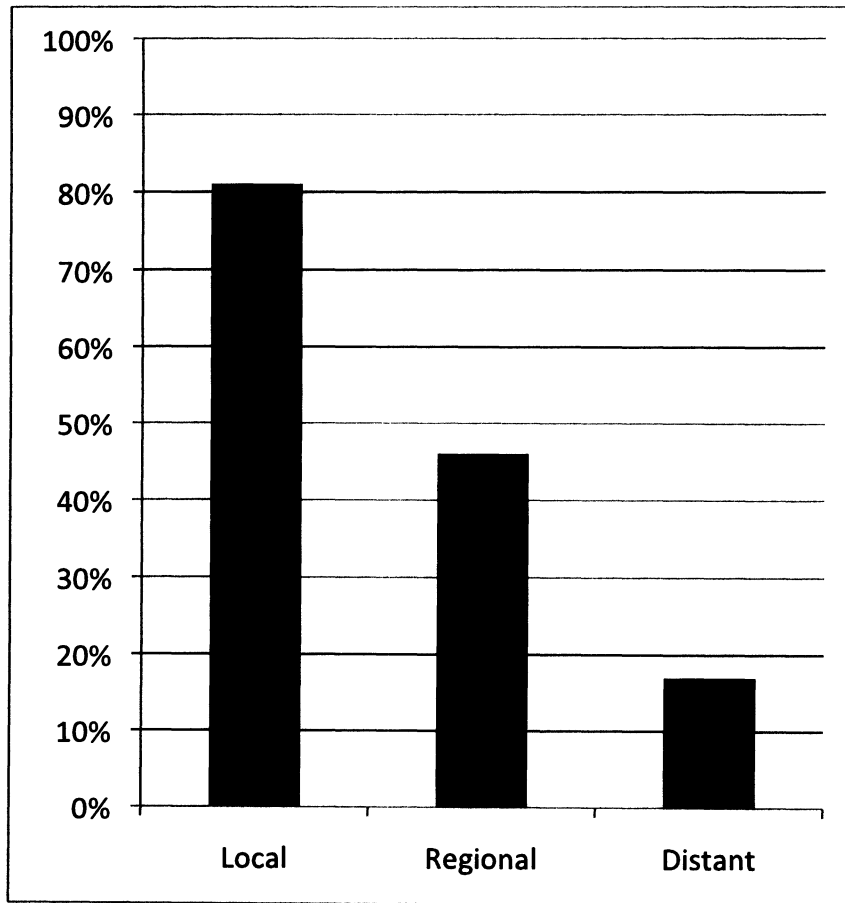
Figure 2-1. 5-year survival rates of oral cancer patients in the United States based on extent of tumor spread show the impact of early detection on prognosis.

2.2 Oral Cavity

2.2.1 Normal Histology

The oral cavity has a stratified squamous epithelium lining [12]. This mucosa is composed of tightly packed epithelial cells that differ morphologically and molecularly depending on the depth beneath the surface. The deepest cells on the basement membrane layer are undifferentiated and are constantly proliferating. The more superficial cells, however, are specialized according to the function and type of the mucosa in a particular area. The oral cavity has three main types of mucosa: masticatory mucosa, lining mucosa, and specialized mucosa.

Masticatory mucosa is present on the gingiva and hard palate. It has either a keratinized or para-keratinized stratified squamous epithelium, resulting in nuclei that are either no longer present or highly pyknotic in cells at the superficial layer. There are four distinct layers of the masticatory mucosa. The stratum basale is the deepest, basal layer that contains undifferentiated cells responsible for cell proliferation. These basal cells are small with prominent nuclei and are cubiodal or columnar in shape. New cells produced in this layer are pushed up to create subsequent layers of mucosa. Stratum spinosum is the next layer, consisting of larger cells that are polyhedron-shaped. More keratin filaments are present in this layer, and membrane-coating granules (MCG) appear near the top of this layer. More MCGs are present in the next layer, the stratum granulosum. This layer is characterized by flat cells with small nuclei and densely packed keratin filaments. MCGs fuse with cell membranes and release their contents into the cells at the top of this layer, forming the boundary between the stratum granulosum and the surface keratinized layer. The density of the keratin filaments and the thickening of the cell

membrane at the surface create a thick, tough layer that reduces the permeability of the masticatory mucosa.

Lining mucosa is found on the lips, cheeks, alveolar mucosal surface, floor of mouth, inferior surfaces of the tongue, and soft palate. It covers muscle, bone, and glands, and is generally non-keratinized. It consists of three layers. The deepest layer again is the stratum basale, a single layer of cells resting on the basal lamina that is responsible for cell proliferation. The stratum spinosum is similar to that of masticatory mucosa and is several cells thick. The stratum superficiale of lining mucosa displays some cell membrane thickening, keratin filaments, and MCG fusion associated with masticatory mucosa, but is more permeable.

Specialized mucosa is associated with the sensation of taste and so is only present on the dorsal surface of the tongue. It contains papillae and taste buds responsible for generating the chemical sensation of taste.

2.2.2 Precancerous Pathology

While normal, healthy oral mucosa appears pink, red or white regions that appear may have the potential for malignant transformation. Leukoplakia (white patches) and erythroplakia (red patches) are clinical diagnoses of grossly abnormal tissue that often indicate dysplasia, a precursor to cancer [7, 13]. Dysplasia is a transitional state between benign growth and malignancy, but does not always progress to cancer. It is characterized by cytological changes including variability in nuclear size and shape, increased nuclear staining by dyes, increased ratio of nuclear versus cytoplasmic size, increased mitotic activity, and lack of the cytoplasmic features associated with normal differentiated cells of the tissue [14]. In dysplastic epithelium, the relative numbers of

the cell types associated with the epithelial layers are no longer observed, drastically affecting overall tissue architecture. These changes generally begin near the basement membrane and can eventually affect the tissue throughout the entire thickness of the epithelium. The severity of dysplasia is determined by the level of the epithelium affected. In mild dysplasia, only the lower one-third of the epithelium contains abnormal cells, while in moderate dysplasia, the lower two-thirds of the epithelium displays pre-malignant changes. Severe dysplasia occurs when the entire epithelium contains cells displaying abnormal cytologic features. If a region of severe dysplasia experiences malignant transformation throughout the entire epithelium, but has not invaded beneath the basement membrane, the lesion is defined as carcinoma-in-situ.

2.2.3 Cancerous Pathology

Once the abnormal cells are no longer confined within the epithelium, the lesion has progressed to invasive carcinoma, or cancer [14]. Malignant cells are able to invade into the space beneath the basement membrane, where they continue to proliferate locally and may also spread to other regions of the body. 90-95% of carcinomas found in the oral cavity are squamous cell carcinomas, meaning they are tumors that arise from cells of the epithelium [15]. The most common sites for squamous cell carcinomas are the tongue (30%), lip (17%), and floor of mouth (14%) [16]. These tumors are usually well or moderately well differentiated, meaning they retain some similarity both architecturally and cytologically to the tissue of origin. Cells of these tumors are commonly arranged in broad sheets and large nests [14]. Cells of well-differentiated tumors form keratin, often leading to masses of keratin called keratin pearls. Well-differentiated tumors have a better prognosis than poorly differentiated tumors, which no

longer resemble the tissue of origin. Poorly differentiated tumors do not form keratin pearls, and have a high nuclear to cytoplasmic ratio.

2.2.4 Benign Oral Lesions

In addition to the precancerous and cancerous states described above, there are many benign oral mucosal abnormalities. These include lichen planus, candidiasis, submucosal fibrosis, and frictional hyperkeratosis among others. Often these conditions look similar under white light to premalignant lesions, and can cause inflammation at the site of the lesion. These can be confounding factors for detection and diagnosis of oral dysplasia and cancer.

2.3 Current Detection Strategies

2.3.1 Conventional Oral Examination

The standard method for oral cancer screening has long been dentists or physicians performing a conventional oral examination. This exam is performed under normal white light and consists of visual inspection of the oral cavity by a healthcare professional, followed by palpation of suspicious lesions. While some published studies indicate a high degree of sensitivity, specificity, and positive predictive value of the conventional oral exam [17-21], other publications suggest that this type of examination has limited value [22, 23]. The expertise of the healthcare professional plays a major role in the value of a conventional oral exam as a screening tool: two pilot studies showed that general dentists had a 71-74% sensitivity of detecting relevant oral mucosal lesions as compared to a specialist's diagnosis [24, 25]. In developing countries with less available medical expertise, a conventional oral exam may be even less effective.

The shortcomings of a conventional oral exam stem from the fact that 5-15% of the general population have oral mucosal abnormalities; only a small fraction of these are actually malignant [26-28]. The oral lesions that have the most relevance to oral cancer are leukoplakia and erythroplakia, clinical diagnoses that refer to white or red patches, respectively. Approximately 10-15% of patients who present with leukoplakia will have their lesions histologically categorized as mild or moderate dysplasia, and about 5% will receive a diagnosis of severe dysplasia or carcinoma in situ [13]. The remaining leukoplakia patients have a slightly increased risk of developing a malignancy at that site, and should be monitored [29, 30]. Oral erythroplakia is much more rare, but is usually histologically diagnosed as severe dysplasia, carcinoma in situ, or invasive carcinoma [7]. A clinician is unable, however, to definitively differentiate between stages of disease with a conventional oral exam alone, and a biopsy must be taken. The final shortcoming of the oral exam is that it may be unable to detect malignancies underlying normal mucosa. One study found that 36% of patients with a new head and neck squamous cell carcinoma showed histologic evidence of dysplasia or microinvasive cancer in clinically normal mucosa from the corresponding contra-lateral anatomic site [31].

2.3.2 Gold Standard of Diagnosis

The biopsy is considered the gold standard of diagnosis for oral cancer. This method requires the removal of a portion of the suspicious lesion, followed by fixation, slicing, hematoxylin and eosin (H&E) staining, and diagnosis by a pathologist [32]. This process can take about a week, is invasive for the patient, and requires major resources including equipment and professional expertise [30, 33]. It presents an inconvenience,

expense, and delay of treatment in developed countries, and is not feasible on a large scale in the developing world.

2.3.3 Detection Aids

Other methods to aid in detection of oral cancer have been investigated, including brush cytology, toluidine blue staining, and light-based detection systems. Brush cytology uses an approach similar to the Papanicolaou smear: a stiff brush scrapes epithelial cells from the suspicious region and these cells are stained and examined for features such as increased nuclear to cytoplasmic ratio [34]. This is a less invasive, less expensive method of examining lesions with low cancer risk [31, 35-38]. However, it still requires laboratory equipment and expert cytologists. Overall, oral cytology has demonstrated a limited sensitivity and specificity, and a high occurrence of false negative results [39].

Toluidine blue is a vital dye that has been used *in vivo* to stain nucleic acids and reveal abnormal tissue. It has been used in the oral cavity for decades as a screening tool or as an adjunct to a visual exam [40-42]. However, low specificity has prevented toluidine blue from becoming a standard screening tool in the United States [43-45].

Light-based detection is another strategy that is being employed to assist in the detection of oral cancer. Two commercially available systems, the ViziLite Plus and the MicroLux DL, use tissue reflectance imaging to enhance oral lesion detection [46-50]. The patient's mouth is rinsed with acetic acid and then visually examined using a blue-white light source [11]. While normal epithelium appears slightly bluish under illumination, abnormal epithelium experiences distinct aceto-whitening due to cellular dehydration and compaction of the nucleus. However, studies suggest that while the

sensitivity of these systems may be high, the specificity and positive predictive value is low, preventing this tool from becoming widely accepted in clinical practice [51, 52]. Several benign conditions such as leukoedema and frictional keratosis also experience aceto-whitening [46].

Other light-based detection systems use autofluorescence rather than reflectance to detect abnormal tissue. Cellular alterations that occur due to malignant transformation can alter the concentration of naturally occurring fluorophores in tissue, thus resulting in a change in autofluorescence of the region. Both imaging and spectroscopy devices have been shown to distinguish between normal and malignant tissue [53-55]. However, imaging systems may be more practical for screening for oral cancer because a much larger area can be observed at one time as opposed to the small region that can be examined at a single time with the optical fibers used in spectroscopy [56]. The VELscope is a commercially available device that uses narrow-emission tissue fluorescence to visually detect abnormal lesions [57-59]. The tissue is excited at 400-460 nm, and normal tissue appears pale green when viewed through the narrow-band filter provided with the instrument. Abnormal tissue, however, displays a loss of autofluorescence and appears dark next to the normal tissue. One of the first studies using this instrument (published in 2006) reported extremely high values of sensitivity and specificity for the VELscope, but in this study all the lesions were also recognized by the conventional oral exam under white light [58]. In a 2010 study of 156 patients, the reported VELscope sensitivity was 50% and specificity was 38.9% [51]. In this study, the VELscope again did not identify any abnormal sites that were not detected under white light inspection alone. In a 2011 analysis, Awan et al. reported a VELscope

sensitivity of 84.1% and specificity of 15.3% after examining a set of 126 patients with premalignant or benign oral abnormalities [60]. The high prevalence of confounding factors and the low specificity of the VELscope prevent this device from distinguishing between low-risk and high-risk lesions in the oral cavity, limiting its use as a screening tool for oral cancer.

2.4 Contrast Agents

Epithelial tissue contains various sources of endogenous contrast that arise from the morphological and molecular features of the tissue. These features can be altered along the path of cancerous progression, and so measuring these features has been important to delineate stages along that progression. As described previously, reflectance imaging can be used to observe changes in tissue architecture as an indication of dysplasia or cancer. Fluorescence imaging and spectroscopy can measure loss of autofluorescence that occurs in abnormal oral tissue. These inherent changes in reflectance and fluorescence arise as neoplasia alters cellular characteristics such as inter-nuclear spacing and fluorophore concentration. These endogenous sources of contrast can be used to distinguish between normal and abnormal tissue.

While endogenous contrast has been useful, the optical detection of cancer can be enhanced with exogenous contrast agents that also highlight morphological and molecular changes within tissue. Exogenous contrast agents have a much brighter optical signature and so are more sensitive to small changes in tissue as compared to endogenous contrast. This may allow for earlier detection and characterization of abnormal oral lesions. In addition, exogenous contrast agents are able to target specific molecules of interest that cannot be detected with endogenous contrast.

The exogenous contrast agents that will be used in the studies reported in this thesis are described below. The advantages of fluorescent contrast agents include the small size of the fluorophore, the bright optical signal, the choice of excitation and emission wavelengths, and the ability to detect the signal with low cost light sources such as light emitting diodes (LEDs) [61, 62]. Fluorescent dyes are very small, and so are able to penetrate through multiple layers of tissue. This relative ease of delivery makes them well suited to stain both cells and tissue.

2.4.1 Agents Targeted to the Epidermal Growth Factor Receptor

The human epidermal growth factor (EGF) is a small peptide consisting of 53 amino acids, and is about 6 kDa in size. It is the natural ligand to the epidermal growth factor receptor (EGFR) on the extracellular surface of cells. Although EGFR is present in normal proliferating cells [63], the receptor is over-expressed in 50-98% of all oral squamous cell carcinomas, and is associated with early tumorigenesis, making it an excellent biomarker for oral cancer [64-69]. Cancer cells up-regulate this growth receptor so that they can achieve self-sufficiency in growth signals, which is one of the hallmarks of cancer [70]. Tumor EGFR levels have been shown to correlate tumor size and clinical stage [64, 65, 68], and can serve as a prognostic indicator for overall disease-free survival [66].

EGF-Alexa 647 consists of an Alexa Fluor 647 carboxylic ester dye (Invitrogen, CA) conjugated to human EGF peptide (Calbiochem, MA) at the peptide's primary amine groups. This conjugate is purified using size exclusion chromatography and dialysis to remove any free dye from the labeled peptide. The Alexa Fluor dye excites at 647 nm and emits at 670 nm. This dye was chosen because these wavelengths

correspond to regions of the spectrum with low endogenous optical signal [62]. This contrast agent allows fluorescent imaging of EGFR. Fluorescently labeled EGF has been used *in vivo* previously for imaging of mammary tumors in mice [71, 72].

An alternate way to target EGFR is to use an antibody to the receptor. A fluorescent EGFR antibody can be prepared by conjugating an Alexa Fluor 647 dye to the amine groups on the antibody. This contrast agent is purified using size exclusion chromatography to remove any free dye from the labeled antibody. Fluorescent anti-EGFR has been used to detect the receptor in tissue using imaging or spectroscopy [61, 73-76].

2.4.2 2-NBDG

2-(N-(7-nitrobenz-2-oxa-1,3-diazol-4-yl)amino)-2-deoxyglucose (2-NBDG) is a commercially available fluorescent glucose analog consisting of a glucose molecule attached to a fluorescent dye, shown in Figure 2-2 [77]. It is a small molecule with a molecular weight of 342.26 g/mol. 2-NBDG's fluorophore excites at 470 nm, and emits with a peak at 550 nm. The excitation emission matrix (EEM) for 2-NBDG is shown in Figure 2-3. This contrast agent was developed as a fluorescent indicator of glucose uptake activity in cells [77, 78]. The glucose component allows 2-NBDG to be transported through the GLUT transporters and be internalized by live cells, resulting in cytoplasmic fluorescence. This contrast agent has been used to visualize the level of cellular metabolism, a characteristic that is increased in the rapidly growing and dividing cells of dysplasia and cancer [79]. High metabolism and the associated increased cytoplasmic fluorescence from 2-NBDG can therefore identify cells experiencing the uncontrolled growth associated with neoplasia. 2-NBDG is an optical analog of [18]F-

FDG, which is routinely used in positron emission tomography (PET). While 2-NBDG is

not yet approved for human use, ^{18}F-FDG has been used as a contrast agent for PET for

many years without significant deleterious side effects.
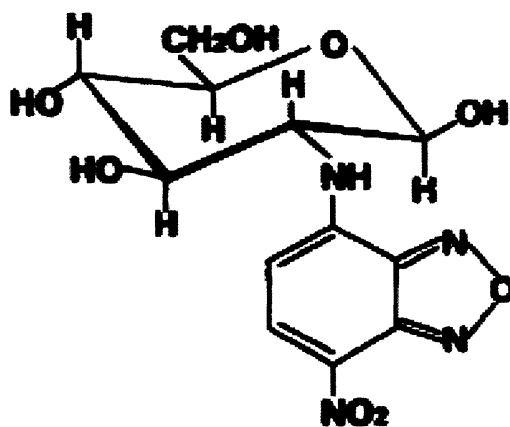
Figure 2-2. Chemical structure of 2-NBDG
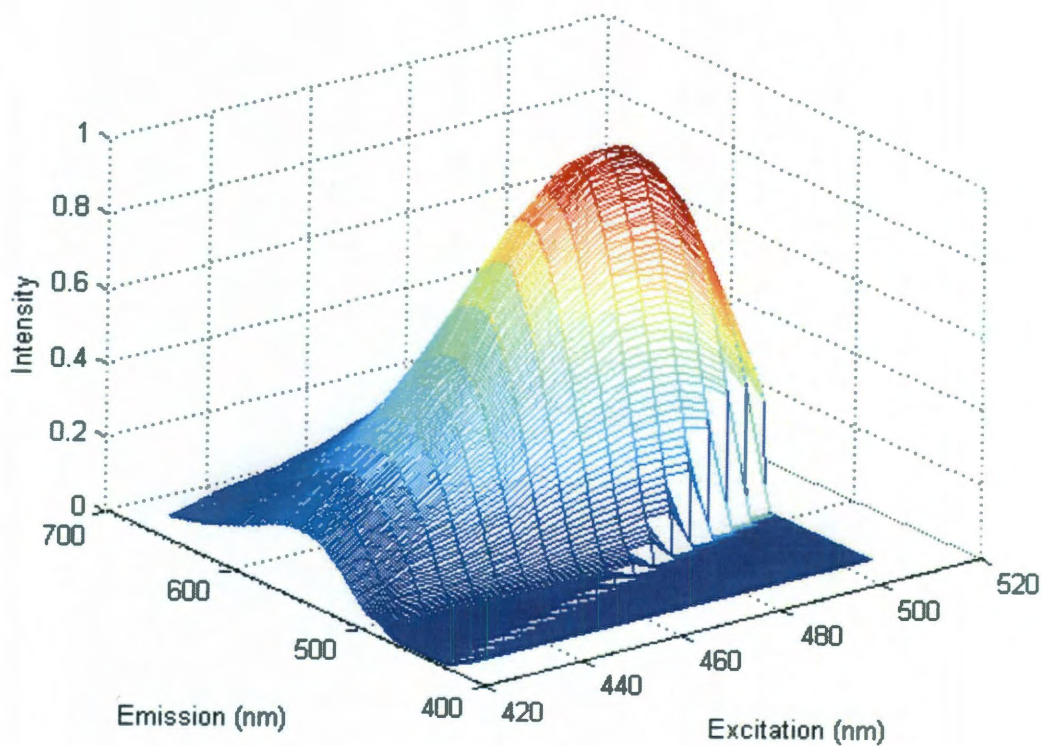
Figure 2-3. Excitation emission matrix of 2-NBDG, intensity is normalized to a maximum value of 1

2.4.3 Proflavine

Like other acridine compounds, proflavine binds reversibility and non-covalently to nucleic acids by intercalating between adjacent base pairs [80]. Its chemical structure is shown in Figure 2-4. Although proflavine is not molecular-specific, its binding to DNA distinguishes nuclei from the cytoplasm of the cell. High-resolution fluorescent imaging of this agent in tissue can give information about inter-nuclear spacing and nuclear to cytoplasmic ratio, both important metrics used in the histological diagnosis of cancer. Proflavine has a broad excitation range with its peak at around 430 nm, and emits light with a peak around 515 nm. The excitation emission matrix for proflavine is shown in Figure 2-5. Proflavine has been used clinically as a topical antibacterial agent, and has

also been used topically in humans in an investigational in vivo study of gastrointestinal cancer [81, 82]. While acriflavine is not currently FDA approved, an investigational new drug (IND) application has been filed and accepted for a few specific in vivo protocols for head and neck and gastrointestinal cancer patients.
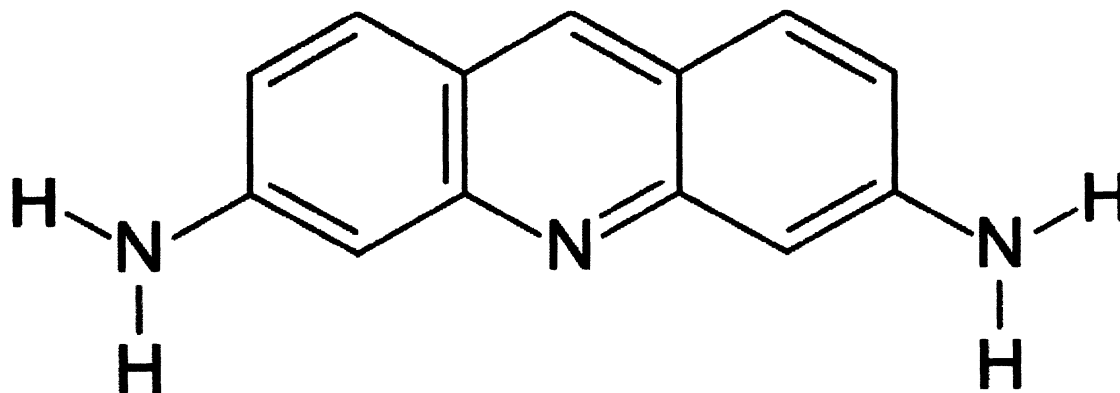
Figure 2-4. Chemical structure of proflavine
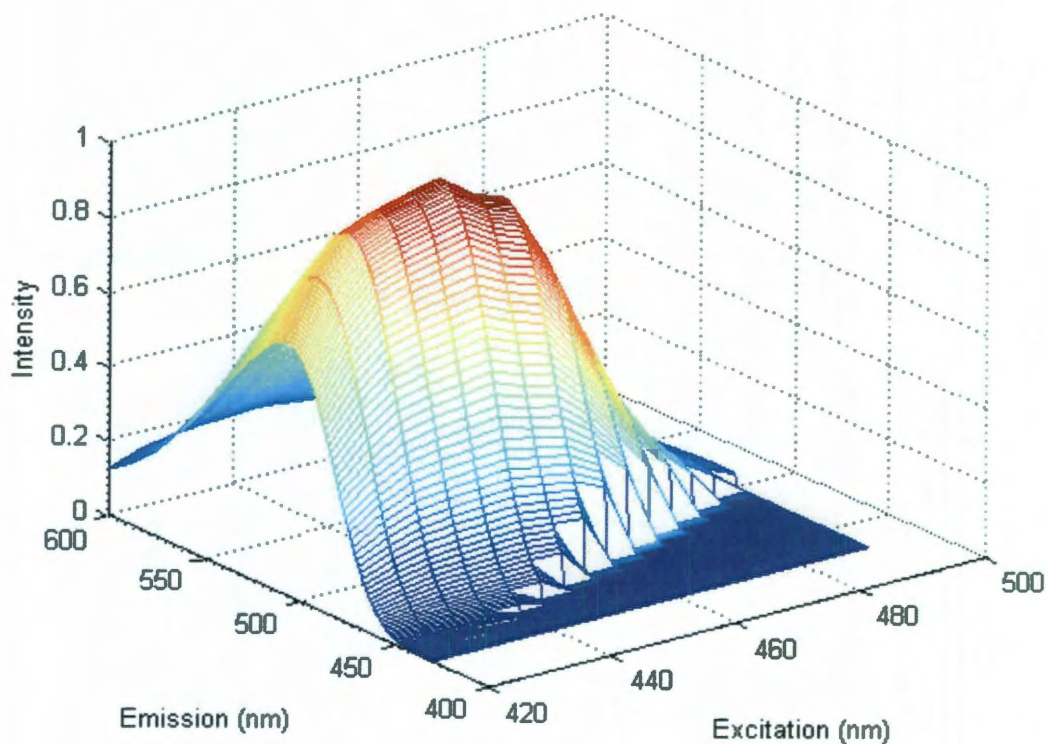
Figure 2-5. Excitation emission matrix of proflavine, intensity is normalized to a maximum value of 1

When used in combination, the contrast agents described here can provide information about tissue architecture and about functional, molecular-specific alterations that occur due to neoplasia.

2.5 Optical Systems

2.5.1 Multi-spectral Digital Microscope

The Multispectral Digital Microscope (MDM) is a wide-field fast-acquisition imaging device that is capable of capturing white light and fluorescent images. It consists of a commercially available dental surgical microscope, a mercury arc-lamp light source, excitation and emission filter wheels, two scientific-grade high-resolution color

CCD cameras, a computer, and custom adaptors needed to modify the microscope [83]. The field of view of the device depends on the magnification setting but can range between one and four centimeters. Figure 2-6 shows the optical diagram of this instrument.

Illumination filter wheel

CCD

XBO

Collection

filter wheel
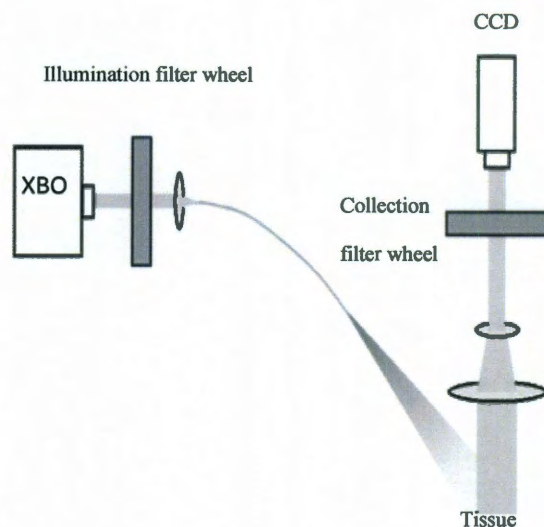
Tissue

Figure 2-6. Optical diagram of the Multispectral Digital Microscope

The MDM has been used in clinical pilot studies to examine the endogenous contrast present in normal versus precancerous and cancerous tissue [83]. Cancer and precancer display a loss of autofluorescence in a broad portion of the spectrum due to alterations in the concentration of endogenous fluorophores in the tissue in response to neoplasia. Example images of abnormal tissue from the oral cavity demonstrating this loss of fluorescence in a few different wavelengths are shown in Figure 2-7.
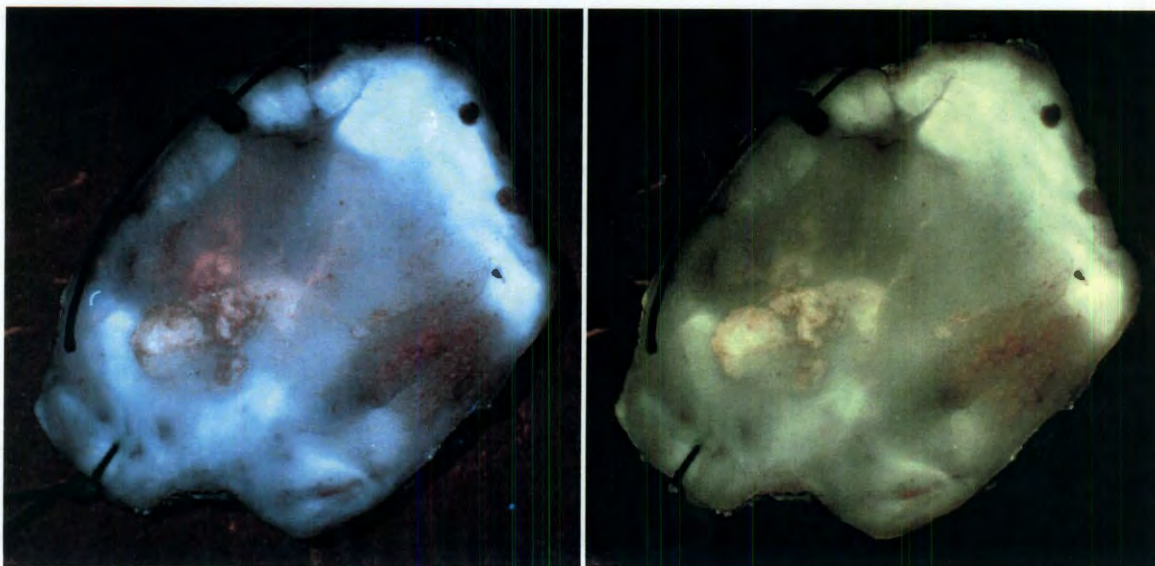
Figure 2-7. Example MDM images of oral mucosa with mild to moderate dysplasia in the regions showing loss of autofluoresence

While endogenous contrast exists, using the exogenous contrast agents proposed here could potentially improve the ability of the MDM to detect cancerous lesions. The molecular-specific agents provide information about the lesions that cannot be obtained through autofluorescence imaging alone, which may help to distinguish cancer from other confounding conditions such as leukoplakia, inflammation, and hyperkeratosis. Since the MDM is able to image fluorescence over a wide field of view, the oral cavity could be quickly surveyed to detect abnormal regions.

2.5.2 High Resolution Microendoscope

The high resolution microendoscope (HRME) is a fiber-optic fluorescence imaging system capable of sub-cellular resolution [84]. It consists of an LED light source, a flexible fiber-optic bundle, a 10x/0.25 NA microscope objective lens, and a CCD camera. The LED emits light centered at 455 nm (20 nm FWHM). Fluorescence emission from the sample is collected through the fiber optic bundle, transmitted through

a 475 nm cut-off dichroic mirror, and imaged onto a CCD camera via a tube lens. The field of view depends on the size of the fiber bundle, but can range from 350 to 750 microns. The resolution of the instrument is less than 4 microns. The optical design is shown in Figure 2-8.
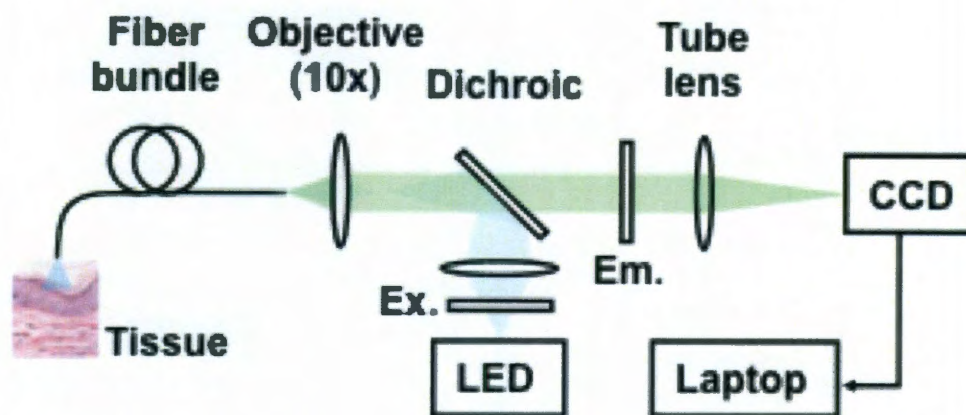
Figure 2-8. Optical design of the high resolution microendoscope (figure adapted from Rosbach et al., 2010 [85])

The HRME has been used with proflavine as a contrast agent to image nuclear size and spacing in *ex vivo* oral and esophagus tissue samples in clinical pilot studies [86]. Nuclear to cytoplasmic ratio can be assessed, which is an important metric in histopathologic diagnosis. The advantage of the HRME over traditional histopathology is that the tissue can be imaged in real time, allowing a faster diagnosis that does not require tissue removal. The small size of the fiber bundle also means that the HRME can be inserted through a needle and used for imaging sub-surface tissue. This aspect makes HRME imaging with proflavine contrast accessible to deeper tissues; this idea is extended to imaging lymph nodes from breast cancer patients in a study described in this thesis. An example HRME image of normal lymphatic tissue is shown in Figure 2-9.
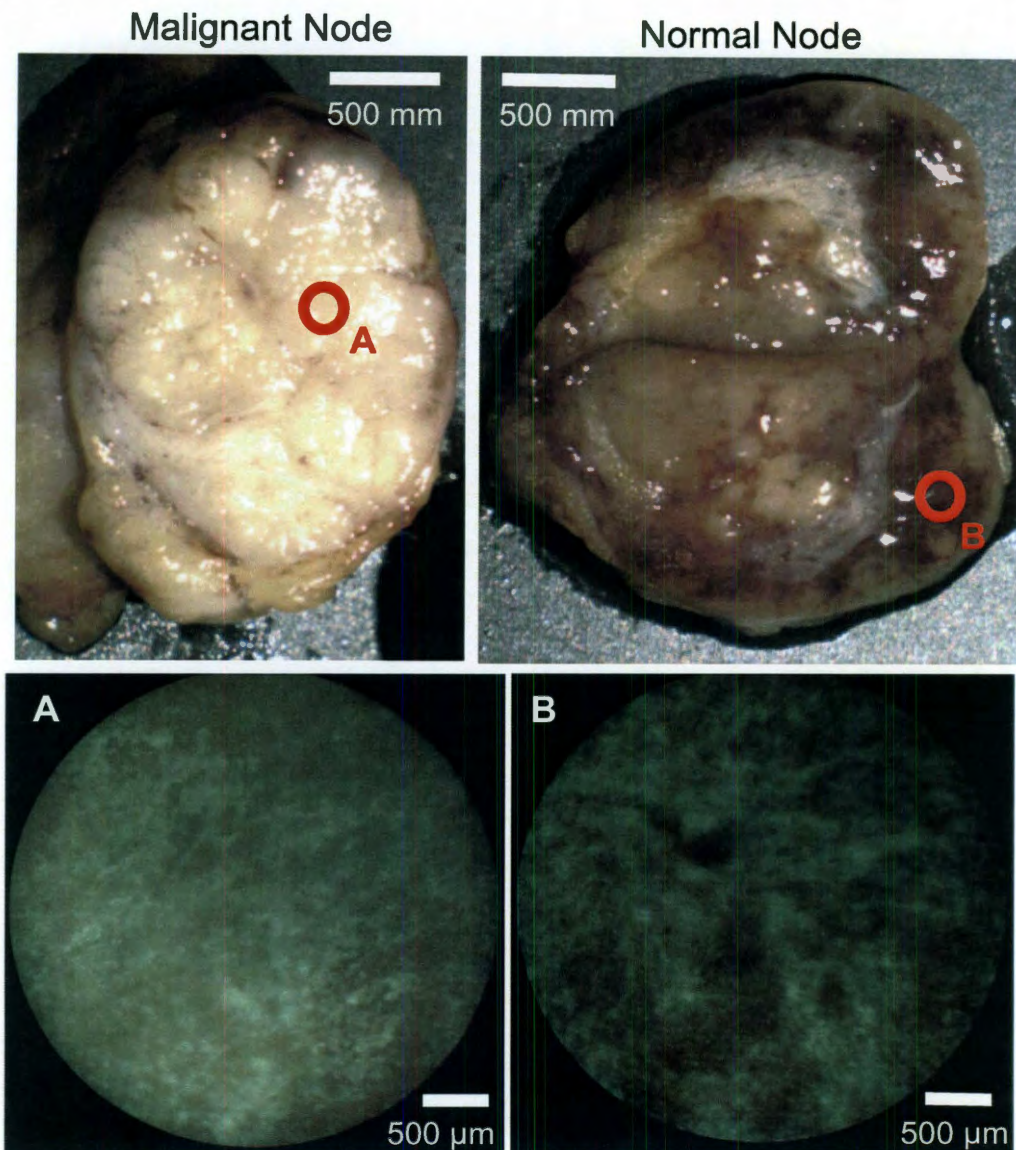
Figure 2-9. (A) HRME image taken from a malignant lymph node (B) HRME image taken from normal lymphoid tissue, photograph of nodes shown above was taken with the MDM with the site of HRME imaging indicated with a red circle

2.6 Conclusions

Because of the high prevalence of confounders in the oral cavity and the lack of specificity of current detection aids, optical molecular imaging could serve as an important tool for examining biomarker expression levels in disease and confounding states to help identify features that correlate with the presence of disease. The availability of molecular-specific information from optical imaging may help improve the specificity of screening and elucidate the role biomarkers play in the disease process.

CHAPTER 3: OPTICAL MOLECULAR IMAGING OF EGFR EXPRESSION TO IMPROVE DETECTION OF ORAL NEOPLASIA[1]

3.1 Abstract

Background: The development of non-invasive molecular imaging approaches has the potential to improve management of cancer. Methods: In this study, we demonstrate the potential of non-invasive topical delivery of an epidermal growth factor-Alexa 647 (EGF-Alexa 647) conjugate to image changes in epidermal growth factor receptor (EGFR) expression associated with oral neoplasia. We report a series of pre-clinical analyses to evaluate the optical contrast achieved following topical delivery of EGF-Alexa 647 in a variety of model systems, including cells, three dimensional tissue cultures, and intact human tissue specimens using widefield and high-resolution fluorescence imaging. Data was collected from seventeen different oral cancer patients: eight pairs of normal and abnormal biopsies and nine resected tumors were examined. Results: The EGF-dye conjugate can be uniformly delivered throughout the oral epithelium with a penetration depth exceeding 500 microns and incubation time of less than 30 minutes. Following EGF-Alexa 647 incubation, the presence of oral neoplasia is associated with a 1.5-6.9 fold increase in fluorescence contrast as compared to grossly normal mucosa from the same patient with both widefield and high-resolution fluorescence imaging. Conclusions: Results illustrate the potential of EGF-targeted fluorescent agents for *in vivo* molecular imaging, a technique that may aid in the

---

diagnosis and characterization of oral neoplasia and allow real-time detection of tumor margins [87].

3.2 Introduction

Non-invasive, molecular-specific imaging has the potential to improve management of oral neoplasia by allowing characterization of specific molecular alterations, facilitating the individualized selection of therapy, and enabling real-time evaluation of treatment response [88-94]. Genetic changes that occur during carcinogenesis lead to altered gene expression and protein levels as compared to normal cells. A number of promising molecular biomarkers of early oral neoplasia have been identified [95-99], including several specific mutations and molecular abnormalities that occur during the transition from normal mucosa to dysplasia to invasive carcinoma [100-104]. These molecules can serve as biomarkers for early detection strategies and follow up of high-risk individuals. Although these data herald a breakthrough for deciphering the mechanisms of oral carcinogenesis, they were obtained through analytical techniques requiring tissue from invasive biopsies or surgical resections. Unfortunately, there are currently no techniques available to rapidly screen for these changes at the point-of-care.

The clinical use of molecular imaging in cancer patients has focused primarily on positron emission tomography (PET). PET uses ^{18}F-FDG (fluorodeoxyglucose) or ^{18}F-FLT (3'-Deoxy-3'-^{18}F-fluorothymidine) as contrast agents to provide images with molecular information and is now routinely used for staging and assessment of treatment response in cancer patients [105-107]. While PET imaging has important clinical advantages, it has had a limited role in cancer screening and early detection due to its

limited spatial resolution and cost associated with cyclotron and radio-imaging facilities. An additional major drawback of PET is radiation exposure to the patient.

Optical imaging of tissue autofluorescence has emerged as a strategy for detection and diagnosis of oral lesions [108, 109], and is favorable due to its ability to image tissue with high spatial (less than 1 micron lateral resolution) and temporal resolution (usually video rate) using low-cost, portable devices. However, performance of autofluorescence imaging systems does not always represent an improvement over common white light inspection [110]. Combined fluorescence diagnosis using both autofluorescence and 5-aminolevulinic acid (5-ALA)-induced protoporphyrin IX (PPIX) fluorescence shows improved sensitivity and specificity over autofluorescence alone, but cannot be performed as quickly [110, 111]. Permeation of 5-ALA through mucosa is highly variable, especially in the presence of keratin, and as a result, keratinized oral lesions, especially those exhibiting hyperkeratosis, may be more difficult to diagnose [112].

An alternative approach is optical molecular imaging [6, 93, 113-115] which combines the advantages of molecular-specific imaging with the strengths of optical imaging. For clinical application, a successful optical molecular imaging strategy must solve several challenges: it must utilize a contrast agent which can be effectively and safely delivered to a target tissue *in vivo*, and it must yield images of tissue in real time with the desired spatial resolution and field of view, with a high signal to noise ratio. Optical imaging of fluorescent contrast agents has been used previously to discriminate cancer cells from normal cells, such as the chlorotoxin:Cy5.5 contrast agent [25]. While this agent binds to multiple types of cancer cells, it is not specific for a single target.

The epidermal growth factor receptor (EGFR) is an established biomarker for detection of oral neoplasia [116-119] and also has potential prognostic value [120]. Although EGFR is present in proliferating cells in normal tissue [121] there is marked over-expression during progression to dysplasia and cancer [122]. An estimated 50-98% of oral cancers overexpress EGFR [64, 65, 67, 68, 123]. EGFR expression was a strong prognostic indicator for overall and disease-free survival in patients with advanced head and neck squamous cell carcinoma enrolled in a radiotherapy study and was highly predictive for local-regional relapse but not distant metastases [66].

The goal of this study was to develop and evaluate the potential of a topically delivered optical contrast agent to image EGFR expression for use in the early detection of oral neoplasia. We report a series of pre-clinical analyses to assess the potential of topically delivered EGF-Alexa 647 for molecular imaging of oral neoplasia; we evaluate the resulting optical contrast achieved in cells, three dimensional tissue cultures, paired clinically normal and abnormal biopsies, and surgically resected oral tumors. High-resolution fluorescence imaging was used in biopsy specimens to evaluate the ability of the contrast agent to be delivered throughout the epithelium, and also to quantitatively assess image contrast. Widefield fluorescence imaging was used to assess the spatial heterogeneity of EGFR expression in resected tumors and to quantify the increase in fluorescence intensity of abnormal tissue. High resolution and widefield imaging of contrast provide complementary information that may be useful for better classification of disease state, detection of disease margins, and understanding spatial heterogeneity of biomarker expression. Contrast values achieved in the tissue specimens were compared

to the results of histopathologic diagnosis and immunohistochemical (IHC) analysis of EGFR expression.

3.3 Materials and Methods

3.3.1 Preparation of EGF-Alexa 647

To prepare EGF-Alexa 647 conjugate, EGF peptide (Calbiochem, MA) was labeled with Alexa 647-carboxylic ester (Invitrogen, CA) and purified using size exclusion chromatography and dialysis. This two-step purification was used to completely remove free dye from the labeled peptide; purification was monitored by spectroscopy. Murine derived recombinant EGF peptide was used for the studies in cells, tissue phantoms and biopsies, and human derived recombinant EGF peptide was used for the resected oral lesions. Control experiments (including cells and tissue phantoms) were performed to ensure these data could be combined.

3.3.2 Incubation and Imaging of Cells and Tissue Phantoms

To demonstrate the specificity of EGF-Alexa 647 based contrast agent, we incubated two cell lines with the conjugate. 1483 cells (provided by Dr. Lotan, M. D. Anderson Cancer Center) were selected as a representative EGFR positive cell line, while MDA-MB-435 cells (ATCC, VA) were selected as a representative EGFR negative cell line. The cells were incubated with EGF-Alexa 647 (0.01 mg/ml) for 30 minutes at 37 °C and imaged live using a Zeiss LSM 510 confocal microscope (excitation at 633 nm, and emission filter band pass 650-700 nm). To further demonstrate specificity of the contrast agent, 1483 cells were first blocked with 1% BSA for 30 minutes and then incubated for one hour on ice with equimolar amounts of both EGF-Alexa 647 and anti-EGFR antibody (monoclonal antibody clone 108, Baylor College of Medicine) labeled

with Alexa 488 (Invitrogen, CA). Additionally, a competition assay was performed in which 1483 cells were incubated for one hour on ice with EGF-Alexa 647 and unlabeled EGF. Incubation on ice was conducted to limit intracellular uptake of EGF receptors. The unlabeled EGF was added in concentrations of 0x, 0.1x, 1x, and 10x the molar concentration of EGF-Alexa 647. 1483 cells were also incubated with rhodamine-labeled 3 kD dextran, a nonspecific fluorescent agent with a similar size as EGF peptide. Concentration and incubation conditions for cells with dextran were identical to cells with EGF-Alexa 647. Appropriate power and gain settings to image the rhodamine-labeled dextran with the confocal microscope were determined by first imaging a well with dextran that had not yet been washed, and adjusting settings to detect a strong fluorescence signal from these wells. These settings were then used to image cells that were incubated with dextran and washed.

To assess the potential ability to topically deliver EGF-Alexa 647, a three-dimensional tissue culture system was used. Tissue phantoms were prepared by placing a suspension of approximately 10 million 1483 or 435 cells in a collagen matrix [124]. Phantoms were cultured for 24 hours in a cylindrical chamber (Transwell Chambers, Costar, MA) prior to subsequent incubation and imaging. The EGF-dye conjugate was topically delivered to only the top surface area of the tissue phantom (0.05 mg/ml). After 30 minutes of incubation, tissue phantoms were washed in excess media to remove unbound contrast agent. Following incubation, tissue phantoms were sliced transversely using a Krumdieck tissue slicer (Alabama Research & Development) (200-300 microns thick) and imaged using a Zeiss LSM 510 confocal fluorescence microscope using the same settings used for cell imaging.

3.3.3 Topical delivery of EGF- Alexa 647 in Clinical Samples

To demonstrate the potential of EGF-Alexa 647 to detect oral neoplasia, the conjugate was topically applied to fresh tissue samples obtained from oral cancer patients. Paired sets of clinically normal and abnormal oral biopsies (n=8) were used initially to ensure translation of results from cells and tissue phantoms into human tissue. Once we confirmed contrast agent binding in biopsies, freshly resected oral tumors (n=9) were also incubated with the agent and analyzed. Patients gave written informed consent to participate, and the study was reviewed and approved by the Institutional Review Boards at the University of Texas M. D. Anderson Cancer Center and Rice University. EGF-Alexa 647 (0.05 mg/ml conc. in 1X phosphate buffered saline, pH 7.4) was topically applied to these tissue samples in the presence of 10% dimethylsulfoxide (DMSO). DMSO was used as a permeation enhancer to improve delivery of the EGF-Alexa 647 conjugate through the epithelium of these tissue samples [125-127]. Samples were incubated with EGF-Alexa 647 for 30 minutes, washed with 1X phosphate buffered saline, and imaged using a widefield fluorescence imaging system with appropriate excitation and emission filters. Widefield imaging was used to survey the tissue because it has a large field of view (~5 x 7 cm for these instruments). The biopsies were imaged with the CRiMaestro™ (Woburn, MA), a planar multispectral widefield imaging device. The resected oral tumors were imaged with a multispectral digital microscope, consisting of a modified widefield dental microscope capable of imaging in reflectance and fluorescence modes [83]. Appropriate control experiments were performed to ensure that data from these devices could be combined. To compare the increase in fluorescence intensity of incubated tissue, both pre-incubation and post–incubation images were

acquired. The pre-incubation image provided a measure of autofluorescence background signal from tissue. Following widefield imaging, the biopsy samples were sliced transversely to a thickness of 200-300 microns and imaged in both reflectance (to locate epithelial and stromal regions of tissue slices) and fluorescence (to detect contrast agent) modes using a confocal microscope (Zeiss LSM 510). This high-resolution imaging was used to assess penetration depth of the EGF-dye conjugate. All tissue was returned to the Pathology Department of the University of Texas M. D. Anderson Cancer Center for hematoxylin and eosin (H&E) staining and IHC processing. IHC staining for EGFR was performed by the Research Histology Core Laboratory at M. D. Anderson following standard protocol with a standard EGFR antibody (clone 31G7 mouse anti-human, Zymed).

To further validate the specificity of EGF-Alexa 647 in oral tissues, a resected oral lesion was incubated with rhodamine-labeled 3-kDa dextran in 10% DMSO as a nonspecific fluorescent agent with a similar size as EGF peptide. The concentrations of fluorescently labeled dextran and incubation conditions were identical to the experiments performed with EGF-Alexa 647.

3.3.4 Quantification of Imaging Data

Widefield fluorescence images of the oral tissue samples obtained pre- and post-incubation were quantitatively analyzed using Photoshop 7.0 to calculate the mean fluorescence intensity (MFI) across the tissue surface. A differential contrast value was calculated by finding the ratio of the increase in the MFI of neoplastic tissue after incubation relative to the increase in the MFI of normal tissue. For the biopsies, paired sets of abnormal and normal biopsies from the same patients were used together; for the

resected oral lesions, a head and neck surgical oncologist identified regions of clinically neoplastic and normal tissue from white light images of the lesions. The physician was blinded to the results of fluorescence imaging. Differential contrast was calculated for each clinical sample; results were compared to histology and IHC staining for EGFR.

Portions of the normal epithelium in the resected tumors displayed characteristics of hyperkeratosis or hyperplasia. While these conditions are benign, they may affect the autofluorescence patterns and act as confounding factors in diagnostic strategies based on autofluorescence alone [53, 128]. Additionally, the thickened epithelium may result in entrapment of contrast agent, leading to artificially high differential contrast values. To investigate the specificity of the differential contrast approach with EGF-Alexa 647 and ensure that these conditions will not negatively affect our performance, differential contrast was calculated for regions of hyperkeratosis (n=4) and hyperplasia (n=4) as identified from histology slides by an expert head and neck pathologist. The epithelium in these regions was otherwise normal with no signs of dysplasia or cancer. Differential contrast was calculated for hyperkeratotic and hyperplastic regions relative to the same normal regions that were used previously; there was no overlap between these normal regions and regions of hyperkeratosis or hyperplasia. Differential contrast was also calculated for the tissue incubated with the rhodamine-labeled dextran as another control to investigate the specificity of EGF-Alexa 647.

High-resolution confocal fluorescence images of biopsy slices incubated with EGF-Alexa 647 were also analyzed to quantitatively calculate the MFI in the epithelial region of normal and dysplastic samples and regions containing tumor cells for tumor specimens. A ratiometric contrast value was calculated for each set of paired biopsies by

dividing the MFI of the clinically abnormal tissue by the MFI of the corresponding clinically normal sample. Results were compared to the histologic diagnosis of each biopsy set.

3.4 Results

Confocal fluorescence images of 1483 cells (EGFR positive) incubated with the EGF-Alexa 647 conjugate showed bright red fluorescence localized at the cell membrane; in contrast, images of MDA-MB-435 cells (EGFR negative) incubated with the agent did not show detectable signal under the imaging conditions used here (data not shown). 1483 cells incubated with both EGF-Alexa 647 and anti-EGFR antibody labeled with Alexa 488 showed co-localization of fluorescence signal at the cell membrane as shown in Figure 3-1 (upper). The competition assay with EGF-Alexa 647 and the unlabeled EGF showed a decrease in fluorescence signal with increasing concentrations of unlabeled EGF as shown in Figure 3-1 (lower). In addition, control experiments were also conducted using fluorescently labeled dextran. Images of cells incubated with rhodamine-labeled 3-kDa dextran did not show any binding to or retention of the nonspecific agent in cells.

EGF-Alexa 647 **EGFR Ab-Alexa 488**

White Light **Overlay**

0x   0.1x   1x   10x

Amount of unlabeled EGF added relative to EGF-Alexa 647
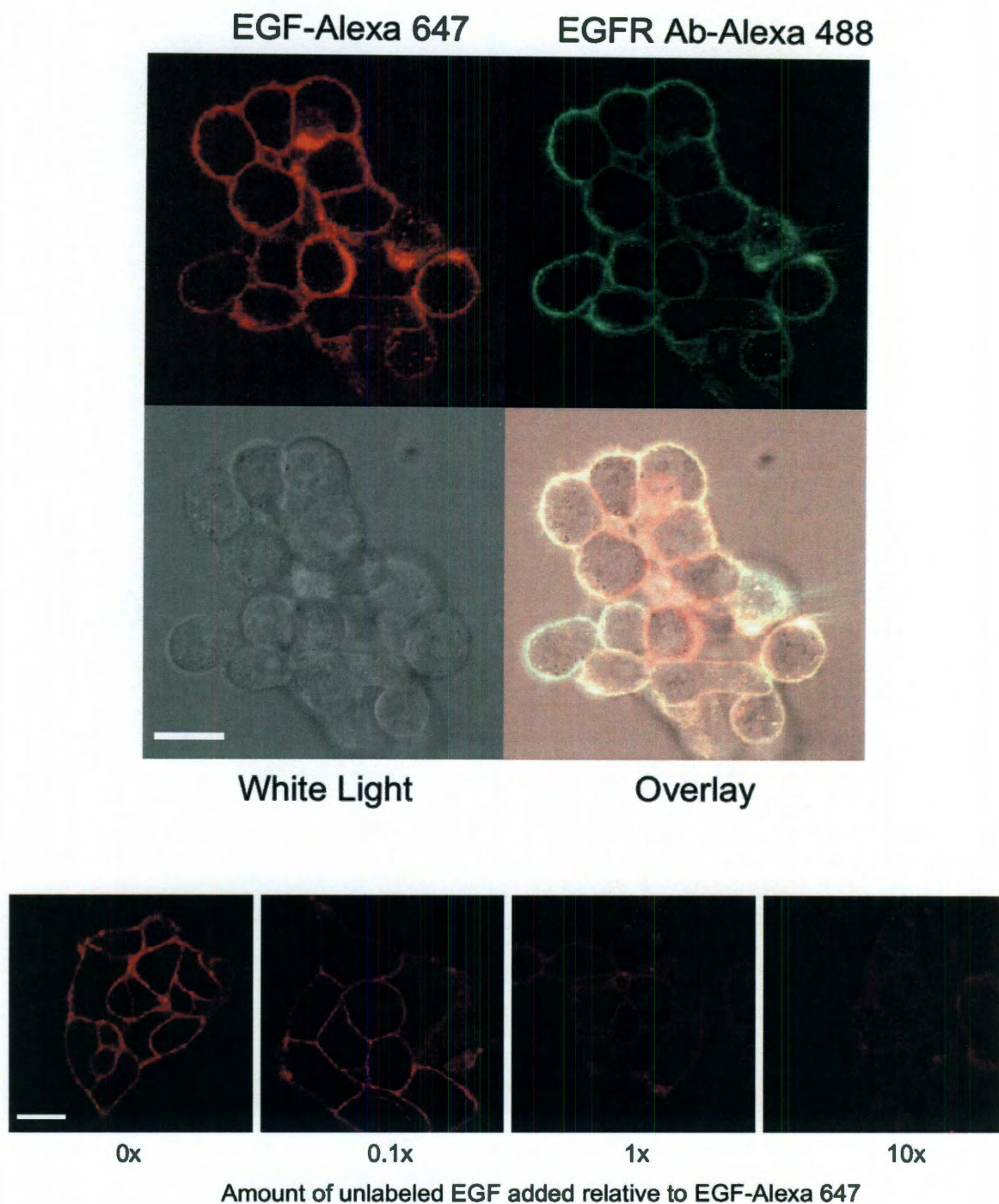
Figure 3-1. (Upper panel): EGFR positive 1483 cells co-incubated with EGF-Alexa 647 (red) and an anti-EGFR antibody labeled with Alexa 488 (green) showing co-localization of fluorescence at the cell membrane. Scale bar is 20 microns. (Lower panel):

Competition assay of 1483 cells incubated with EGF-Alexa 647 and unlabeled EGF added at concentrations of 0X, 0.1X, 1X and 10X the amount of EGF-Alexa 647. Scale bar is 20 microns.

To evaluate whether the EGF-Alexa 647 conjugate could be delivered topically, initial experiments were carried out in three dimensional tissue phantoms. Figure 3-2 shows confocal fluorescence images of two transversely sliced tissue phantoms that were incubated with EGF-Alexa 647 before slicing. Fluorescence signal was observed throughout the phantom containing the EGFR positive 1483 cells, while no fluorescence signal was observed in the phantom containing the EGFR negative 435 cells. In some of the 1483 cells, internalization of the contrast agent was observed. These results demonstrate that selective targeting of EGFR receptors can be achieved in this model system with topical delivery and that excess contrast agent can be easily removed with a simple washing step.
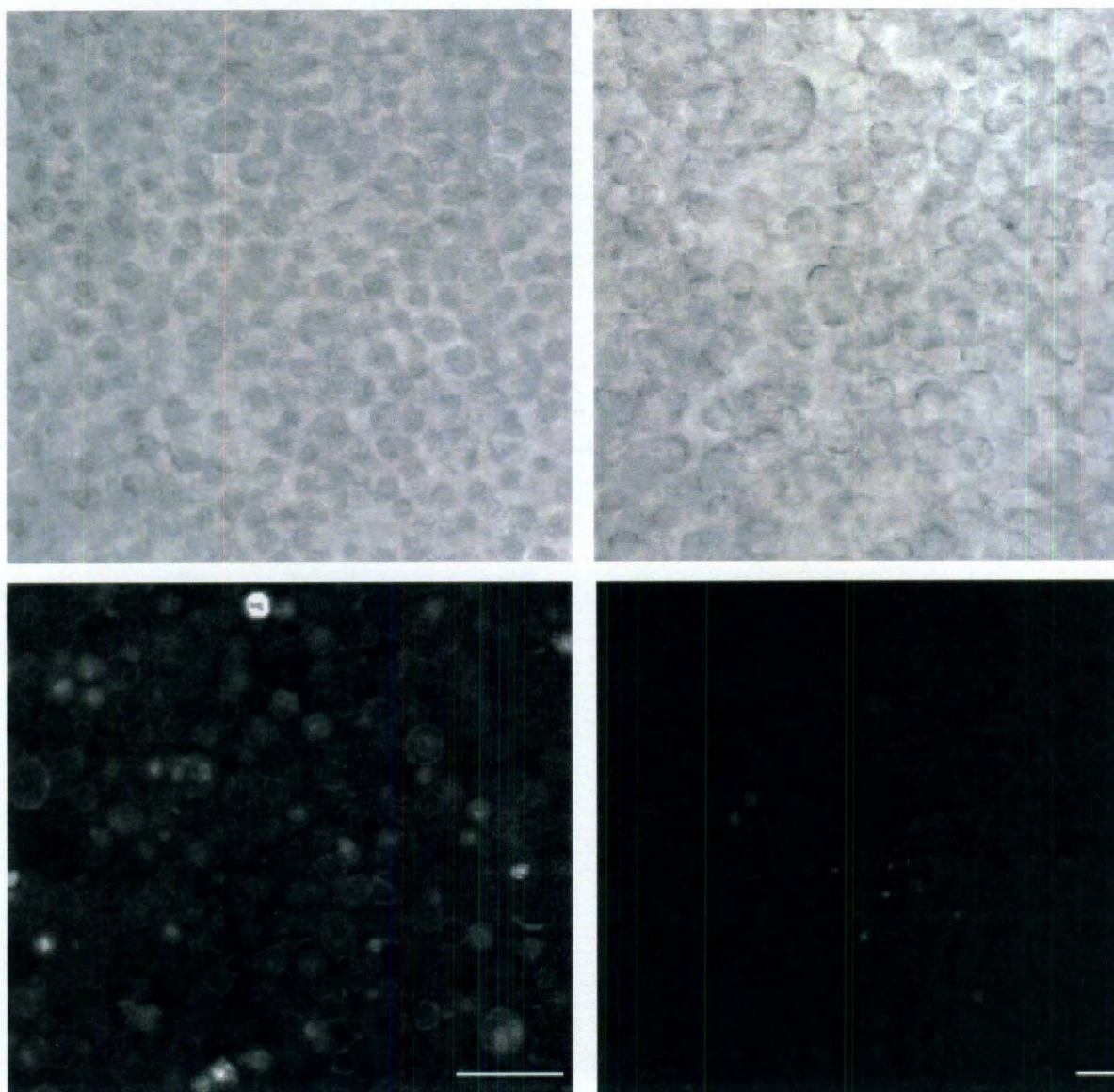
EGFR Positive Tissue Phantom   EGFR Negative Tissue Phantom

Figure 3-2. High-resolution white light and fluorescence confocal images of three-dimensional tissue culture phantoms incubated with the EGF-Alexa 647 conjugate. Scale bars are 100 microns.

Next, EGF-Alexa 647 was topically delivered to fresh oral biopsies and resected lesions to demonstrate its ability to bind to human tissue. Figure 3-3A shows the white light widefield image of a representative tissue sample with the clinically neoplastic region outlined in yellow and a representative normal region outlined in blue. Figure

3-3B shows the widefield fluorescence image obtained after topical delivery of EGF-Alexa 647 and removal of excess contrast agent. A pre-incubation image was obtained using the same instrument parameters in order to estimate levels of auto-fluorescence signal from the tissue sample; the background autofluorescence at these wavelengths was very low. Following incubation with the contrast agent, the fluorescence image shows greater fluorescence intensity in the neoplastic region as compared to the normal region. Fluorescence observed on the edges of this specimen occurs as an artifact of surgical cautery. Fluorescence intensity of the representative normal region and the neoplastic region is shown quantitatively in Figure 3-3C, which compares the mean fluorescence intensity pre- and post-incubation of each region. Figure 3-3D shows the results of IHC staining for EGFR in tissue taken from neoplastic and normal regions. The results show strong staining indicating a high level of EGFR throughout the neoplastic region as compared with only weak staining localized to the basal layer of the epithelium indicating a low level of EGFR in the normal region. The IHC analysis is in agreement with the results from widefield imaging on resected lesions. Pathological diagnosis for this representative case was invasive squamous cell carcinoma.

A

B

C

D

<div style="text-align: center">Neoplastic Region   Normal Region</div>
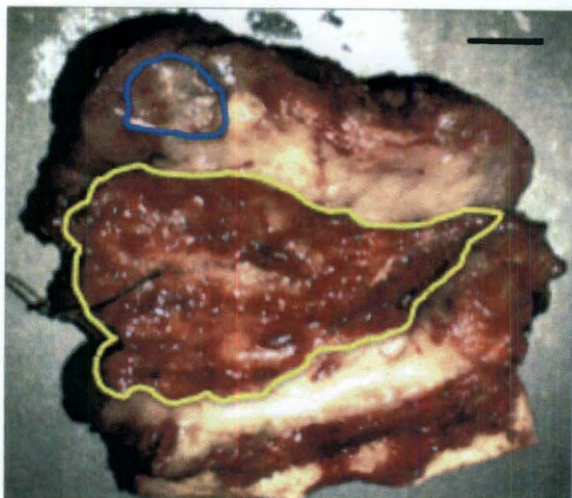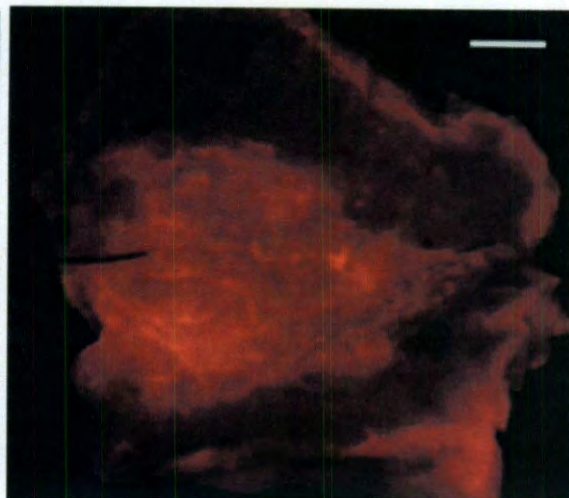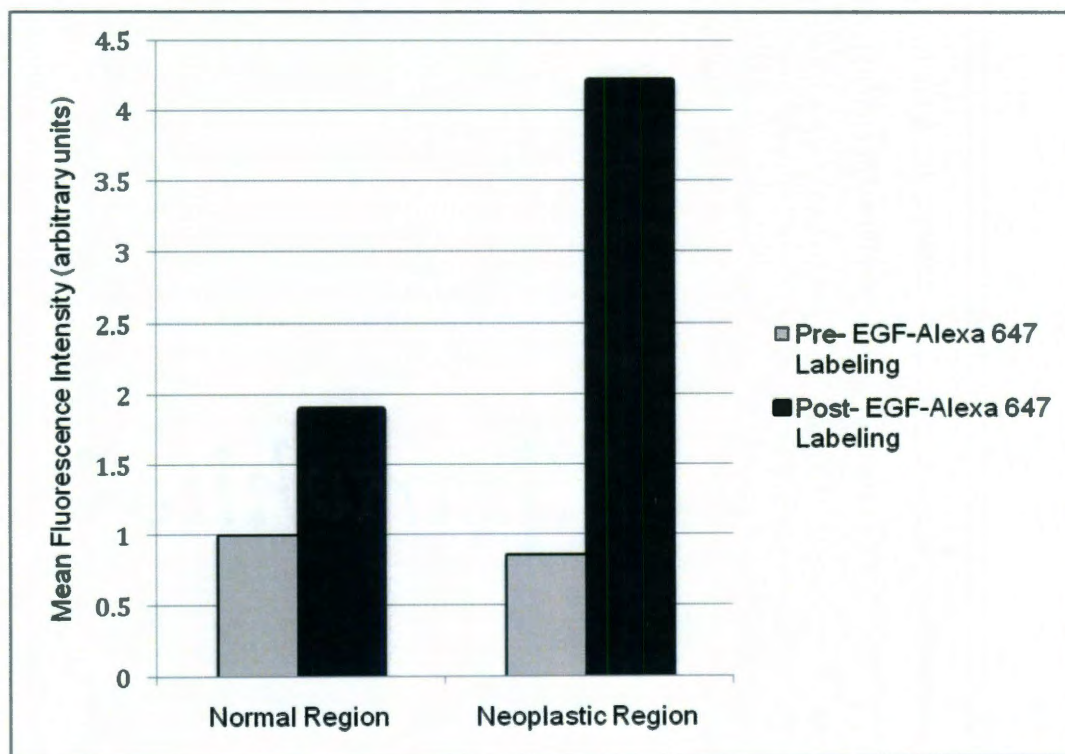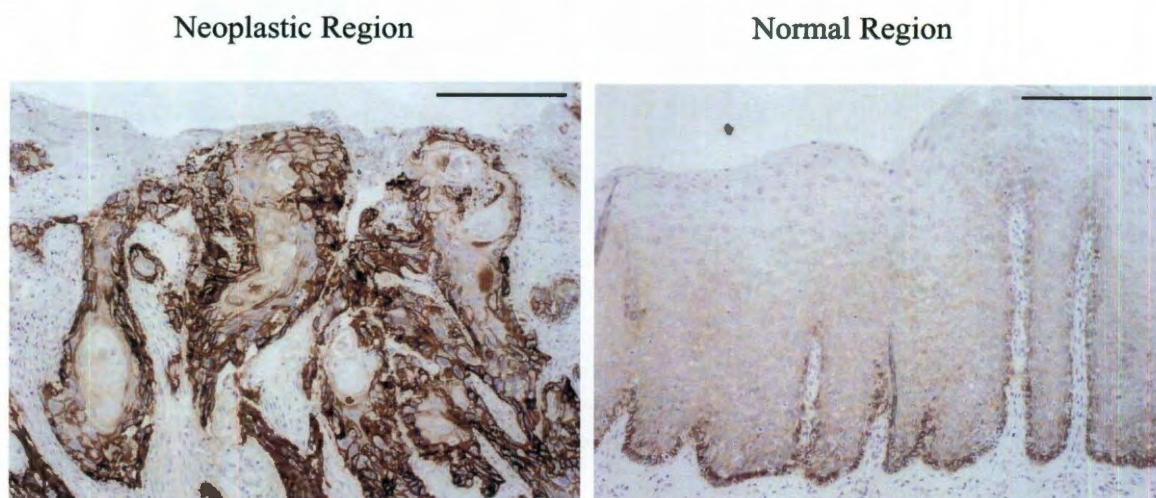
Figure 3-3. (A): Widefield white light image of resected oral lesion. The neoplastic region as selected by an expert clinician blinded to the results of fluorescence imaging is outlined in yellow; the representative normal region is outlined in blue. The histologic diagnosis was invasive cancer. Scale bar is 1 cm. (B): Widefield fluorescence image of the same sample obtained after topical delivery of EGF-Alexa 647 and washing to remove excess dye. Scale bar is 1 cm. (C): MFI of neoplastic and normal regions pre- and post-incubation. All values are normalized to the intensity of the normal region pre-labeling. (D): EGFR IHC stained sections from within the neoplastic and normal regions in the sample. Scale bars are 200 microns.

The resected oral lesion labeled with 3-kDa dextran as a nonspecific fluorescent agent is shown in Figure 3-4 in white light, after incubating with the rhodamine-labeled dextran, and after incubating with EGF-Alexa 647. Background fluorescence was subtracted out using pre-incubation images. No visible non-specific fluorescence is observed after incubation with dextran; after incubation with EGF-Alexa 647, the neoplastic region shows bright fluorescence. The orange pathology ink on the tissue results in the fluorescence seen on the tissue edges in Figure 3-4B. Pathological diagnosis for this sample was invasive carcinoma.

A) White Light
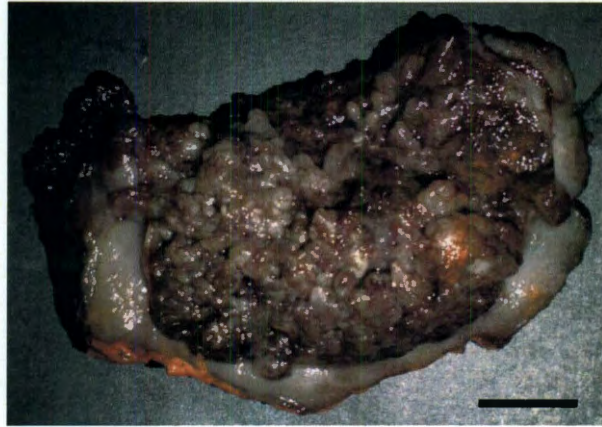
B) Post- incubation with rhodamine-labeled 3 kD dextran
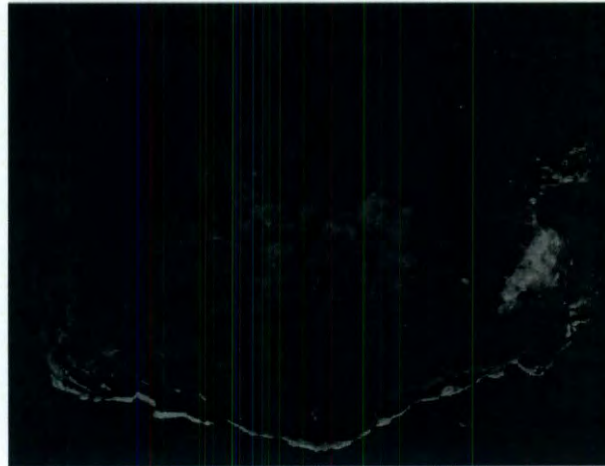
C) Post- incubation with EGF-Alexa 647

Figure 3-4. (A): Widefield white light image of resected oral lesion with neoplastic region outlined in yellow. Scale bar is 1 cm. (B): Fluorescence image of tissue after incubation with rhodamine-labeled 3kD dextran. The orange pathology ink is the cause of fluorescence observed near the edges of the tissue. (C): Fluorescence image of tissue after incubation with EGF-Alexa 647.

A differential contrast value was calculated for each clinical sample to quantitatively compare fluorescence intensity increases in neoplastic and normal tissue. Figure 3-5 shows the differential contrast achieved for each specimen; the histopathologic diagnosis is also indicated. For samples with moderate to severe dysplasia (n=4), the differential contrast ranged from 1.6 to 3.9 with an average of 2.3. For samples with cancer (n=13), the differential contrast ranged from 2.0 to 6.9 with an average of 3.8.
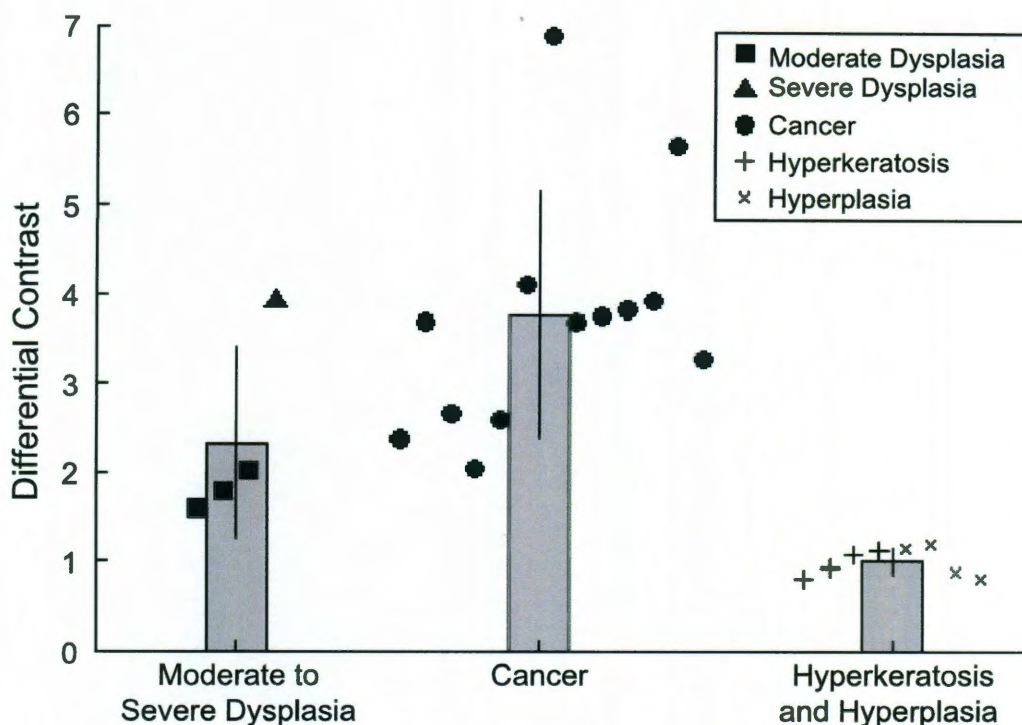
Figure 3-5. Differential contrast values calculated from widefield fluorescence images of fresh oral tissue incubated with EGF-Alexa 647 conjugate. Each data point represents a pair of tissue specimens from a single patient. The bars represent the average differential contrast and standard deviation for tissue with moderate to severe dysplasia (n=4) and tissue with cancer (n=13). Differential contrast values for regions of hyperkeratosis and hyperplasia (n=8) are also indicated.

To quantitatively examine the specificity of EGF-Alexa 647, regions of hyperkeratosis (n=4) and hyperplasia (n=4) were assessed for differential contrast value. The differential contrast obtained for these regions ranged from 0.8 to 1.2 with an average of 1.0. The contrast value of each region is also shown in Figure 3-5. To calculate a differential contrast value of the tissue incubated with dextran, images were taken at a long enough exposure time to detect a fluorescence signal. The fluorescence at this higher exposure, however, was fairly homogenous, as indicated by the calculated differential contrast of 1.04. Following incubation of the tissue with EGF-Alexa 647, the

differential contrast calculated (using the same regions of neoplastic and normal tissue) was 3.27.

After widefield imaging of tissue samples, we obtained high-resolution confocal fluorescence images of transverse tissue slices prepared from biopsies incubated with EGF-Alexa 647. The aim of high-resolution imaging was to assess the tissue distribution of topically delivered EGF-Alexa 647 conjugate. Figure 3-6 shows images a representative pair of biopsies after incubation. Figure 3-6A shows images (fluorescence and IHC) of a clinically abnormal sample diagnosed as cancer, while Figure 3-6B shows images of a clinically and histologically normal sample from the same patient. The fluorescence images highlight significant differences in the contrast agent signal of the two samples; the cancer specimen showed strong uniform fluorescence around epithelial cell membranes. In contrast, the normal sample shows only weak fluorescence around epithelial cells near the basement membrane. The images in Figure 3-6A and Figure 3-6B demonstrate permeation of contrast agents to depths in excess of 500 microns. No residual, non-specific fluorescence was observed in these images, suggesting that excess fluorescent contrast agent can be removed with simple washing. The results of high-resolution optical imaging of EGFR expression in these clinical samples were validated using IHC analysis. The IHC images show strong expression of EGFR in the clinically abnormal biopsy but not in the corresponding normal sample.

Fluorescence   Immunohistochemistry

A) Cancer

B) Normal

C)
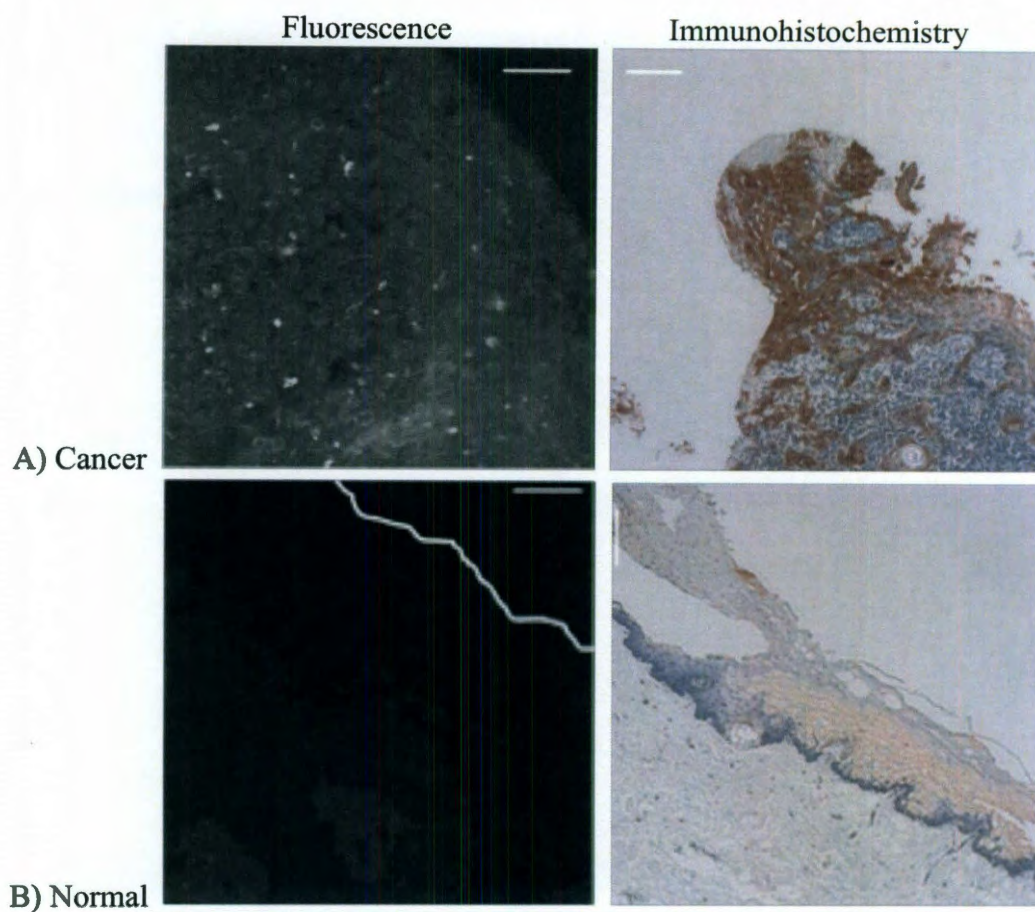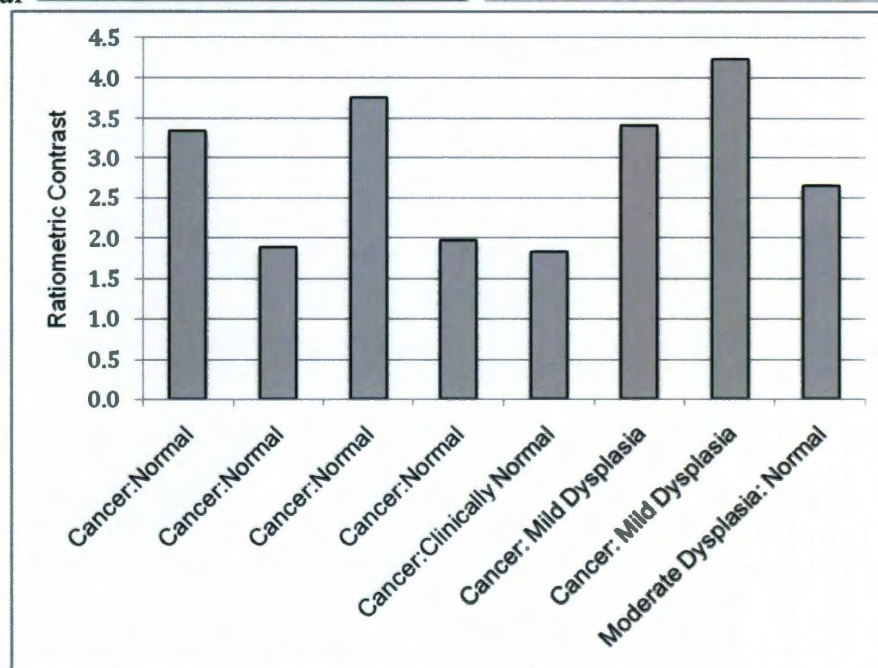
Figure 3-6. (A): Confocal fluorescence image and IHC image of a clinically abnormal specimen incubated with topically applied EGF-Alexa 647 conjugate. The histologic diagnosis was invasive cancer. Scale bars are 100 microns. (B); Confocal fluorescence image and IHC image of a corresponding clinically and histologically normal specimen from the same patient incubated with topically applied EGF-Alexa 647 conjugate. The white line denotes the surface of the epithelium. Scale bars are 100 microns. (C): Ratiometric contrast ratio calculated from high-resolution fluorescence images of eight biopsy pairs incubated with EGF-Alexa 647 conjugate. Histologic diagnosis is indicated for each pair.

A ratiometric contrast value was calculated for each set of paired biopsies (n=8 pairs) to quantitatively compare MFI from the high-resolution fluorescence images of these samples. The ratiometric contrast for each biopsy set is shown in Figure 3-6C; the histopathology diagnosis is also indicated. The contrast is greater than 1.5 in all cases and ranges between 2-4 for most samples.

3.5 Discussion

In this study we evaluated the potential to image the expression of EGFR following topical delivery of fluorescently labeled EGF peptide for detection of oral neoplasia. We investigated the image contrast and topical delivery that could be achieved with this labeled peptide in both widefield and high-resolution imaging, translating results from cells and tissue phantoms to intact human tissue specimens.

In widefield fluorescence images of fresh oral tissue diagnosed as moderate or severe dysplasia, we observed an average 2.3 fold increase in the fluorescence signal in neoplastic tissue as compared to normal tissue. For samples diagnosed as cancer, we observed an average 3.8 fold increase in fluorescence signal. The variability of differential contrast value between samples is expected due to patient-patient variability and also differences in levels of EGFR expression in different sites within the oral cavity.

We also observed some overlap in differential contrast values between dysplasia and cancer. Despite these variations, differential contrast values can distinguish neoplasia from normal tissue; every neoplastic sample had a contrast value greater than 1.5. Our calculated contrast values are consistent with previous studies, which have shown that EGFR expression level increases approximately 2-5 fold with the development of neoplasia. The increase in EGF-Alexa 647 staining intensity is also consistent with the degree of staining observed in IHC analysis.

Widefield imaging observations of differential contrast are paralleled by high-resolution imaging observations of ratiometric contrast. Neoplastic oral biopsies showed a 2-4 fold higher fluorescence signal than paired normal biopsies. At the same time, normal specimens are associated with a small increase in fluorescence after topical application of EGF-dye. We attribute this change to two possible factors. The first is the basal level of EGFR in normal oral epithelium, which can contribute to the increase in fluorescence signal by specific targeting. Second, we observed entrapment of some fluorescence contrast agent in the keratinized superficial layer of some specimens. This entrapment of EGF-dye was observed in the case of a few biopsy specimens, and could not be removed by simple washing steps. However, when differential contrast was calculated for regions of hyperkeratosis with underlying normal epithelium, and in regions of hyperplasia, the average differential contrast value was 1.0, which would be expected for a normal region. All regions of hyperkeratosis or hyperplasia had contrast values lower than any regions with moderate to severe dysplasia or cancer. In this study, neoplastic samples are therefore consistently associated with higher EGF staining than normal samples, even those with a thickened keratin layer or thickened epithelium.

Incubating tissue with the nonspecific fluorescent agent (rhodamine-labeled dextran) resulted in a differential contrast value of 1.04, which is significantly lower than any neoplastic sample. This result clearly demonstrates that EGF-Alexa 647 specifically targets neoplasia.

We selected the EGF peptide to target the EGF receptor rather than an anti-EGFR antibody, which has been used in previous studies to label transverse sections of tissue slices. The EGF peptide (~6 kDa) is significantly smaller than antibodies (~150 kDa), and due to its small size it has increased tissue permeability and clearance of unbound contrast agent can be achieved with simple washing steps. Topical delivery of EGF peptide based contrast agents has the potential to overcome significant difficulties associated with targeting pre-invasive disease in oral tissue using IV delivery or sub-cutaneous injections. In IV based delivery, the distribution of molecular contrast agents is controlled in large part by blood circulation. Since the epithelial layer is avascular, direct delivery of contrast agents to epithelial cells is limited using IV delivery. In addition, losses during circulation, especially for small peptides, can further reduce the effective concentration [129]. IV injected contrast agents typically require 24-48 hours of circulation time to achieve significant specific targeting of in tumor models. This significant delay can limit their use for screening. Further, many of the macromolecular contrast agents such as peptides are susceptible to degradation during such long incubation intervals [130].

One of the potential limitations in selecting naturally occurring growth factor ligands for molecular imaging applications is their ability to activate downstream cell signaling for proliferation. This observation has recently been reported using labeled

human EGF-peptide in implanted tumor cell lines [72]. To overcome this potential limitation, it is possible to select targeting peptides using library based screening approaches. Studies have shown the potential to select EGFR targeting peptides with reduced proliferative activity as compared to the natural EGF ligand [131, 132].

A potential limitation of widefield imaging alone is that it may be difficult to determine a precise margin of disease, especially if the tumor extends in the sub-mucosa, since the vast majority of photons collected with the current widefield imaging device come from the superficial three millimeters of tissue. However, widefield images are useful since they allow a quick survey of a large region of tissue and can be used to locate lesions and estimate disease margins. Even regions of moderate dysplasia that might not be obvious clinically displayed contrast agent binding that could be visualized with widefield fluorescence imaging. Once an approximate margin is determined from widefield images, high-resolution imaging can be used to refine this margin. Fiber optic confocal systems can be placed on or inserted beneath the tissue surface to allow assessment of contrast agent binding to cells along the perimeter, and therefore be used to determine a precise margin and detect sub-mucosal tumor extension.

In summary, we have demonstrated non-invasive topical delivery of a molecular contrast agent to image changes in EGFR expression in oral neoplasia. Using a combination of widefield and high-resolution imaging we obtain quantitative contrast ratios to differentiate clinically neoplastic tissues from normal samples in both biopsies and resected oral lesions. The imaging results are in agreement with the pathological diagnosis as well as the IHC analysis. Results suggest that molecular imaging of EGFR is

a non-invasive approach that may have the potential to aid in molecular diagnosis and characterization of oral neoplasia in a clinical setting.

3.6 Acknowledgement

CHAPTER 4: OPTICAL MOLECULAR IMAGING OF MULTIPLE BIOMARKERS OF EPITHELIAL NEOPLASIA: EGFR EXPRESSION AND METABOLIC ACTIVITY IN ORAL MUCOSA

4.1 Abstract

Background: Biomarkers of cancer can indicate the presence of disease and also serve as therapeutic targets. An optical imaging approach using molecularly-targeted contrast agents can map out expression of multiple biomarkers simultaneously and with high spatial resolution. This tool examines biomarker expression level and heterogeneity, which have implications for improved disease detection and personalized medicine. Methods: To examine how biomarker expression correlates with the presence of disease in this proof-of-concept study, two clinically relevant biomarkers, epidermal growth factor receptor (EGFR) expression and metabolic activity, were assessed in nine samples of freshly resected oral mucosa using the topically applied optical imaging agents EGF-Alexa 647 (to target EGFR) and 2-NBDG (to target metabolic activity). Quantitative features were calculated from the resulting fluorescence images and compared to histopathology maps of the tissue. Results: The EGF-Alexa 647 signal reflected EGFR expression level as indicated by immunohistochemistry. A classification algorithm developed using linear discriminant analysis resulted in an area under the curve of 0.83. Regions with a posterior probability from 0.80-1.00 contained >50% neoplasia 99% (84/85) of the time. Conclusions: This study demonstrates a proof-of-concept of how non-invasive optical imaging can be used as a tool to study expression level of multiple

biomarkers and their heterogeneity across a large mucosal surface area, and how biomarker characteristics correlate with the presence of neoplasia. Applications of this approach include predicting regions with the highest likelihood of disease, elucidating the role of biomarker heterogeneity in cancer biology, and identifying patients who will respond to targeted therapy.

4.2 Introduction

The molecular changes that accompany the progression of tissue throughout the dysplasia to carcinoma sequence can serve as diagnostic aids, therapeutic targets, surrogate end-points in clinical trials, or as an indication of recurrence [101, 133-135]. Many promising biomarkers of neoplasia have been identified and investigated. For example, in breast cancer patients, estrogen receptor positivity as indicated by immunohistochemistry (IHC) is not only associated with improved prognosis but also qualifies the patient for targeted hormonal therapy such as tamoxifen [136]. When it was recently discovered that 90% of gastrointestinal stromal tumors have an activating mutation in the KIT (CD117) receptor tyrosine kinase gene, a KIT inhibitor known as imatinib was developed which dramatically improved patient survival [137]. In ovarian cancer patients, serum level of CA125 is a well-established biomarker for monitoring treatment response or relapse [138]. While these examples highlight successful integration of biomarker information with disease management, the full picture of the role biomarkers play in cancer biology, the heterogeneity of their expression, and the implications biomarkers have on clinical management of patients is not always fully understood. We need a better understanding of the in vivo expression and the spatial and

temporal heterogeneity of these biomarkers and how they correlate with the presence of disease.

To develop this understanding, we need the ability to simultaneously map out the distribution of multiple biomarkers across a large mucosal surface in vivo. An optical molecular imaging approach using targeted contrast agents is well suited for non-invasive imaging of eight or more biomarkers in distinct spectral bands with high spatial resolution, and may serve as an important tool in better understanding the role of biomarkers in the disease process [139]. The current gold standard of assessing protein expression, IHC, has some limitations, including the need to remove the tissue of interest for assessment and difficulty in reporting quantitative biomarker expression levels [140]. IHC is also unable to examine more than a single biomarker per slide, unless the proteins of interest lie in distinct compartments within the cell such as one marker in the nucleus and one in the cytoplasm. Information from multiple biomarkers frequently outperforms information from a single marker alone [136]. Breast cancer presents a good example of this in clinical practice, where estrogen receptor, progesterone receptor, and HER2/neu expression are all routinely assessed for prognosis and selection of therapy. High-throughput methods to measure mRNA expression can simultaneously assess thousands of genetic indicators of disease, and though they are good screening tools to determine which biomarkers may be of interest in a particular cancer type, they generate more information than is clinically relevant and cannot provide information about spatial distribution.

This study demonstrates a proof-of-concept of how non-invasive optical imaging with multiple topically applied targeted contrast agents could be used to study the

heterogeneity of biomarker expression and its correlation with the presence of neoplasia across a large mucosal surface area. The oral cavity was chosen as an organ site due to its accessibility to optical imaging, and the two clinically relevant biomarkers that were assessed in this study include the epidermal growth factor receptor (EGFR) and metabolic activity. Quantitative features of biomarker images are compared to the gold standard of histopathology. One example of how this approach may serve as an adjunctive tool to quantify and study biomarker expression and heterogeneity is discussed.

EGFR is one of the most commonly studied biomarkers in cancers of the oral cavity because it is widely overexpressed in oral squamous cell carcinoma and dysplasia [141]. Though the reported percentage of patients with overexpression of EGFR varies between studies, a review from Lippman et al. indicates that 80-100% of patients with premalignant or malignant oral lesions have high EGFR expression [104]. EGFR expression level also increases with the progression of disease [69, 142-144]. A recent study from Taoudi Benchekroun et al. found that 71% of oral premalignant lesions display high EGFR expression levels, which correlated with a greater risk of developing oral cancer. Quantitative IHC studies reveal that the factor of overexpression of EGFR ranges from approximately 1.7- to 3-fold increase in dysplasia and cancer [69, 142, 145]. A similar level of overexpression was also observed in targeted molecular imaging studies [74, 87]. The prevalence of EGFR expression makes it a useful target for both detection and treatment; in fact, the EGFR inhibitor cetuximab is FDA approved for head and neck cancer therapy.

Another clinical biomarker for oral cancer is increased metabolic activity. Metabolism is elevated in dysplasia and cancer due to rapid cell growth and division, so

glucose transporters (GLUTs) are often overexpressed or operate at a higher activity level. In a study by Kunkel et al., 100% (40/40) of oral cancers expressed GLUT-1 by IHC, and Mellanen et al. found that every tumor sample they examined expressed either GLUT-1 or GLUT-3 mRNA [146, 147]. Ayala et al. found GLUT-1 overexpression in 50% of their oral cancer specimens [148], Tian et al. observed that 73.7% of samples had moderate to strong GLUT-1 expression [149], and Ohba et al. discovered that overexpression of GLUT-1 in the invasion front is associated with the tumor depth and prognosis [150].

4.3 Materials and Methods

4.3.1 Preparation of Fluorescent Imaging Agents

To assess EGFR expression, the natural ligand of EGFR, the epidermal growth factor (EGF), was conjugated to a fluorescent dye. Purified human-derived recombinant EGF peptide (Calbiochem, San Diego, CA) was conjugated to Alexa Fluor 647-carboxylic ester (Invitrogen, Carlsbad, CA). Excess free dye was removed by size exclusion chromatography followed by dialysis. The resulting EGF-Alexa 647 imaging agent was diluted to a final concentration of 25 µg/mL in sterile 1X phosphate buffered saline (PBS) with 10% dimethylsulfoxide (DMSO) as a permeation enhancer. Specificity studies in both cells and resected human tissue have been previously performed and published with EGF-Alexa 647, demonstrating the ability of this agent to specifically target EGFR in cell culture and in oral mucosa [87].

A fluorescently labeled glucose molecule was used to assess metabolic activity. 2-(N-(7-nitrobenz-2-oxa-1,3-diazol-4-yl)amino)-2-deoxyglucose (2-NBDG) is a commercially available optical glucose analog (Invitrogen, Carlsbad, CA). 2-NBDG was

diluted to a concentration of 0.16 mM in sterile 1X PBS. Multiple published studies have used 2-NBDG as a metabolic activity indictor. Tumor cells in culture have been shown to take up approximately 5 times the amount of 2-NBDG compared to non-malignant cells, and competition assays with free glucose decreased the amount of 2-NBDG that was taken up [79]. A recent study by Sheth et al. demonstrated the comparability of 2-NBDG to FDG-PET imaging in several preclinical examples, and Nitin et al. demonstrated the potential use of 2-NBDG for detecting neoplasia in clinical specimens, in which dysplasia and cancer displayed a 2- to 5-fold increase in fluorescence intensity compared to normal tissue [151, 152].

4.3.2 Application of Fluorescent Imaging Agents onto Clinical Samples

To evaluate the ability of 2-NBDG and EGF-Alexa 647 to identify neoplasia in human oral tissue, freshly resected clinical specimens were obtained from patients undergoing surgery at M. D. Anderson Cancer Center. These patients gave written informed consent to participate in the study, which was approved by the Institutional Review Boards at both M. D. Anderson Cancer Center and Rice University. Neoplastic tissue was obtained immediately following surgical resection and taken to a lab for contrast agent application and subsequent imaging.

To assess autofluorescence before the application of any fluorescent contrast agents, the tissue was imaged with a multispectral digital microscope (MDM), a widefield imaging system that has been described in detail previously [83]. Briefly, the MDM is a dental microscope that has been modified with fluorescence excitation and emission filters and a mercury-argon light source; it is capable of imaging in both reflectance and fluorescence modes. It has a large field of view (~5 x 7 cm) and can

achieve a lateral spatial resolution up to 0.016 mm. Pre-incubation images of the tissue were taken using standard white light setting and the filter configurations for 2-NBDG (ex. 475, em. 550) and EGF-Alexa 647 (ex. 650, em. 670) to allow later subtraction of tissue autofluorescence from post-incubation images.

After autofluorescence imaging, 2-NBDG solution was topically applied to the epithelial surface of the resected oral tissue and placed in an incubator at 37 °C for 20 minutes. Following incubation with 2-NBDG, the tissue was briefly rinsed with sterile 1X PBS to remove any excess unbound fluorescent contrast agent. The tissue was again imaged with the MDM using the filter configurations for 2-NBDG and EGF-Alexa 647. Next, EGF-Alexa 647 in 10% DMSO was topically applied to the epithelial surface of the tissue and incubated for 20 minutes at 37 °C. The tissue was briefly rinsed with sterile 1X PBS and imaged using appropriate filter settings on the MDM.

Once imaging was complete, the entire tissue was returned to the Pathology Department of M. D. Anderson Cancer Center. The tissue was processed following standard procedures: the tissue was thinly sliced anterior to posterior and placed into cassettes for H&E staining. Locations of pathology cuts were documented and the portion of the tissue that was placed into each cassette was recorded to allow for future correlation to pathology. Neither 2-NBDG nor EGF-Alexa 647 affects histopathology processing or staining.

4.3.3 Creation of Histopathology Maps

To compare the results of widefield imaging with the gold standard of histopathology, a two-dimensional color-coded pathology map was synthesized for each clinical specimen. To create this map, all the H&E slides for each specimen were

reviewed with an expert Head and Neck Pathologist blinded to the optical images (MW). The diagnosis across the entire epithelium was recorded for each slide. This expert diagnosis from the slide was assumed to represent the diagnosis for the entire thickness of the thin piece of tissue that was placed in the corresponding cassette. The diagnoses of normal epithelium; mild, moderate, and severe dysplasia; and cancer were all assigned a unique color code. Based on detailed notes of where the tissue was sliced and the diagnosis across the epithelium for each piece of tissue, the color-coded histopathology map was created as an overlay on top of the white light image of the clinical specimen. The resulting two-dimensional histopathology map was used as a gold standard to compare with the widefield fluorescence images. Creation of a histopathology map is not standard practice in pathology, and in order to create an accurate map, the tissue had to have a fairly flat surface, slicing had to be strictly monitored and documented, and a detailed pathology reading across the entire surface had to be obtained and recorded. All the tissue samples used in this study met these criteria.

4.3.4 Immunohistochemistry to confirm EGFR expression

The Research Histology Core Laboratory at M. D. Anderson Cancer Center performed immunohistochemical staining for EGFR on multiple specimens in order to confirm that imaging results correlated with the gold standard indicator for the presence of EGFR. A standard staining protocol was followed using the Research Histology Core Laboratory's standard antibody for EGFR (clone 31G7 mouse antihuman; Zymed, South San Francisco, CA). An expert Head and Neck Pathologist reviewed these slides to grade the intensity of staining across the entire epithelial surface. The scale used for assessment of intensity of EGFR immunostaining was from zero to three. Score 0

indicated no staining or non-specific staining, score 1 was used for weak staining of >10% of cells, score 2 indicated moderate staining of >10% of cells, and score 3 indicated strong and complete staining of >10% of cells [153].

Immunohistochemistry for GLUT expression was not compared with fluorescence imaging results with 2-NBDG because while IHC can reveal GLUT expression level, it cannot assess GLUT activity level. Previous studies have not found a significant correlation between overexpression of glucose transporters and standardized uptake values of FDG in FDG-PET imaging, a widely accepted clinical method of analyzing metabolic activity [149, 154].

4.3.5 Quantitative Analysis of Fluorescence Images

Post-incubation fluorescence images of both 2-NBDG and EGF-Alexa 647 were analyzed using Matlab R2010b software (The MathWorks, Natick, MA) to identify trends that might distinguish between diagnostic categories. All images pre- and post-incubation were aligned using a built-in image registration algorithm. The fluorescence images were converted to grayscale and background autofluorescence was subtracted. For each clinical sample, multiple square regions 50 x 50 pixels in size were selected, using the histopathology map as a guide to ensure that each region selected contained a uniform diagnosis and that regions did not overlap. Statistical features were calculated and compared to feature values from regions of normal tissue to determine if these characteristics were altered in neoplastic tissue. These features included mean intensity, standard deviation, skewness, kurtosis, and the coefficient of variation within each region. Additionally, a Matlab edge detection algorithm using the Canny method was applied to the bulk fluorescence image in order to detect where sharp gradients in

intensity occurred because this may also serve as a measure of heterogeneity of biomarker expression. The length of this edge line divided by the number of pixels in the region was calculated for all selected regions and considered a candidate feature in the classification algorithm.

4.3.6 Development of a Classification Algorithm

To discriminate normal from neoplastic regions of interest based on these quantitative feature values, a classification algorithm was developed using linear discriminant analysis. The algorithm used all of the 50 x 50 pixel regions for both training and testing. Features were selected sequentially to identify which were most useful in distinguishing neoplastic tissue from normal tissue. Only three features were chosen in order to avoid over-training of the algorithm. Sensitivity, specificity, and area under the receiver operator characteristic curve (AUC) were calculated.

4.3.7 Application of Classification Algorithm to a New Data Set to Predict Regions with the Highest Likelihood of Disease

We examined the ability of this algorithm to identify regions of interest with the highest likelihood of disease, information that could be useful for early detection and diagnosis, planning surgical resection, monitoring treatment response, or screening for recurrence. A 50 x 50 pixel grid was used to divide the original fluorescence images from all the patients into new regions of interest. The classification algorithm described previously was applied to these regions in order to generate posterior probabilities (a value between zero and one) for all the new regions. The practical application of this strategy would be to help a clinician objectively identify areas with the highest likelihood of disease, including determination of the best place to take a biopsy in order to confirm

the presence of neoplasia. The regions with posterior probabilities from 0.80-1.00 were identified and compared to histopathology map information at that site. Regions with posterior probabilities from 0.60-0.79 were also identified as regions likely to be neoplastic, and this prediction was compared to the histopathology gold standard to assess performance of the algorithm. Only regions that contained epithelium throughout the entire 50 x 50 pixel region were evaluated, meaning that regions overlapping the edge of the tissue were not considered.

The same analysis was applied to the remaining specimens. Each region identified as having a high posterior probability was compared to the gold standard histopathology map to determine if more than 50% of the identified region contained neoplasia.

4.4 Results

Nine distinct clinical specimens from different patients were incubated with both 2-NBDG and EGF-Alexa 647 and imaged as described. Histopathology maps were created for these nine specimens to allow analysis of the fluorescence signal from different diagnostic categories. Figure 4-1 shows images from two representative clinical specimens: one with mild to moderate dysplasia and one with cancer. The figure includes a white light photograph of the tissue, post-incubation fluorescence images after application of 2-NBDG and EGF-Alexa 647, and the corresponding histopathology map. Qualitative comparison of the fluorescence images and the gold standard histopathology maps of both samples demonstrates that for both imaging agents, there is greater fluorescence intensity in areas of neoplasia, including areas of invasive carcinoma as well as in areas of mild to moderate dysplasia.
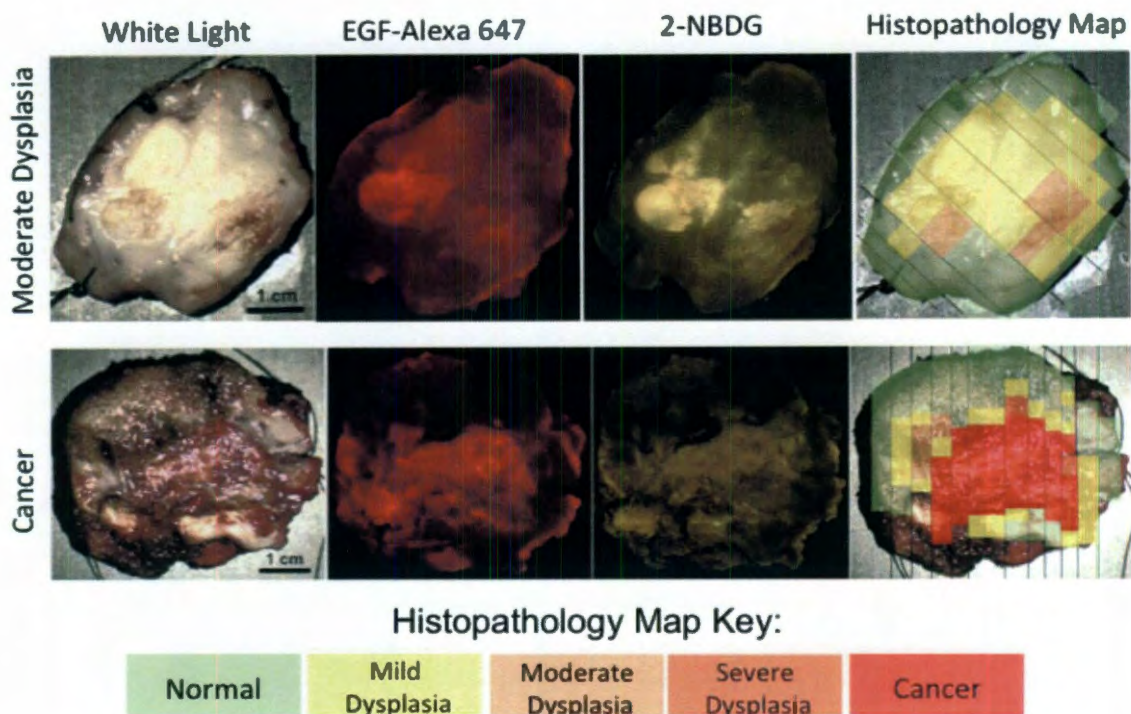
Figure 4-1. Two representative specimens. The tissue is shown first in white light, next in fluorescence after incubation with EGF-Alexa 647 to show EGFR expression, then in fluorescence after incubation with 2-NBDG to show metabolic activity, and finally with the corresponding histopathology map. Qualitative observation shows that areas of high fluorescence correspond to areas of neoplasia. Scale bars are 1 cm.

4.4.1 Immunohistochemistry to confirm EGFR expression

IHC staining for EGFR was performed on multiple slides from this set of specimens in order to confirm previously published findings. IHC staining intensity correlates well with fluorescence intensity, confirming specificity of EGF-Alexa 647 (images not shown).

4.4.2 Quantitative Analysis of Fluorescence Images

Figure 4-2 shows a representative sample with the outlines of the selected 50 x 50 pixel regions of interest. This example contains 4 normal regions, 3 regions of mild dysplasia, 9 regions of moderate dysplasia, and 3 regions of severe dysplasia. The

regions are oriented parallel to the pathology slices in order to maximize the number of regions that could be selected per sample. Table 4-1 details the number of regions that were selected per sample by diagnostic category. Overall, 286 total regions were selected and were categorized as follows: 87 normal regions, 57 regions with mild dysplasia, 26 regions with moderate dysplasia, 20 regions containing severe dysplasia, and 95 regions with cancer.
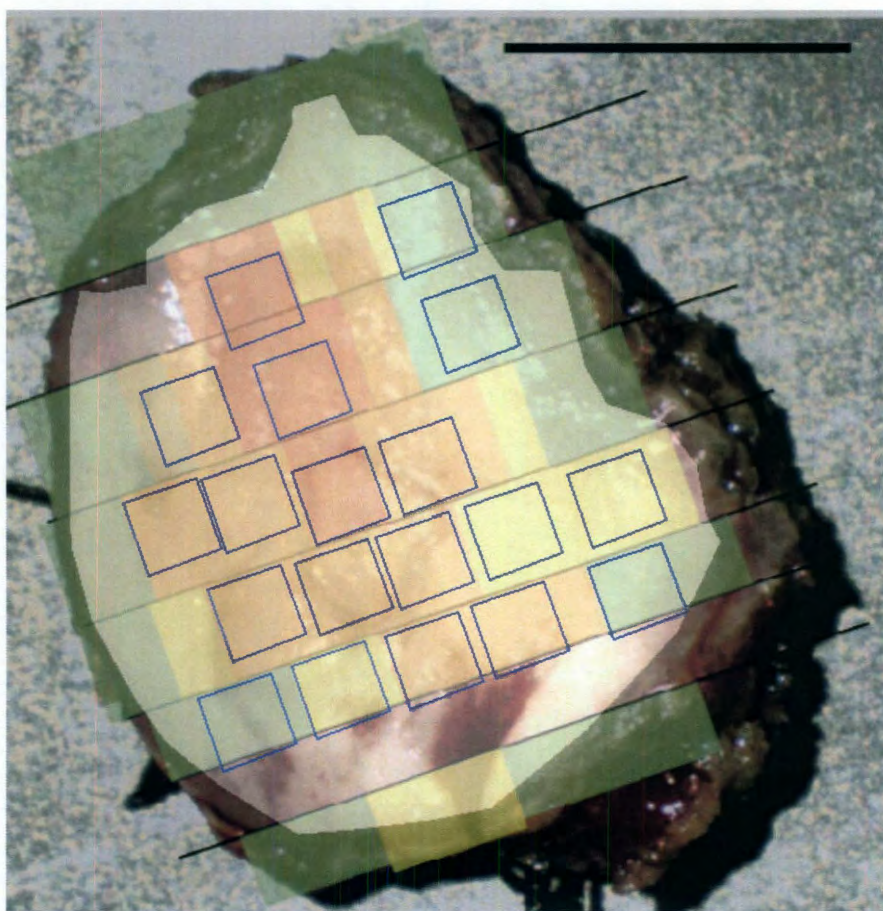
Figure 4-2. Representative example of how 50 x 50 pixel regions were selected. This sample contains 4 normal regions, 3 regions of mild dysplasia, 9 regions of moderate dysplasia, and 3 regions of severe dysplasia. Quantitative features were calculated from each region of interest. Scale bar is 1 cm.

Table 4-1. Number of analyzed regions by patient and diagnosis

Specimen #	Normal	Mild Dysplasia	Moderate Dysplasia	Severe Dysplasia	Cancer	Total
1	4	3	9	3	0	19
2	18v	1	1	0	12	32
3	14	3	0	15	4	36
4	12	33	8	0	0	53
5	9	6	3	2	17	37
6	9	3	3	0	23	38
7	3	2	1	0	2	8
8	6	1	1	0	23	31
9	12	5	0	0	15	32
Total	87	57	26	20	96	286

4.4.3 Development of a Classification Algorithm

For each region, statistical features including average intensity, standard deviation, skewness, kurtosis, maximum value and coefficient of variation were calculated from both kinds of post-incubation fluorescence images. Additionally, the length of the edge line detected using the Matlab edge function was calculated for each region using both fluorescence images. These statistical features were used to train and test a classification algorithm on the full set of 286 regions. Table 4-2 indicates the classification performance of the top six highest performing single features, ranked by AUC. Of the top six features, four features are calculated from the EGF-Alexa 647 signal and two features are calculated from the 2-NBDG signal. Normalized mean intensity of the EGF-Alexa 647 signal was the highest performing single feature with an AUC of 0.80. Table 4-2 also indicates the AUC of the three-feature algorithm developed from a combination of quantitative features as described below.

Table 4-2. Performance of single feature in classification algorithm

Feature	AUC of Single Feature
EGF Mean Intensity	0.80
EGF Entropy	0.76
EGF Standard Deviation	0.73
NBDG Mean Intensity	0.70
EGF Maximum Value	0.70
NBDG Maximum Value	0.68
NBDG Edge Detection (5x threshold)	0.68
NBDG Edge Detection (2x threshold)	0.67
EGF Edge Detection (original threshold)	0.66
NBDG Standard Deviation	0.65

Figure 4-3 shows scatter plots of four selected features of interest, with the y-axis indicating feature value and the x-axis sorted by pathologic diagnosis. Figure 4-3A shows normalized mean intensity of the 2-NBDG signal, Figure 4-3B shows normalized intensity of the EGF-Alexa 647 signal, Figure 4-3C shows the coefficient of variation from the 2-NBDG signal, and Figure 4-3D shows the length of the detected edge divided by number of pixels based on the 2-NBDG signal. Ultimately, three features were selected for use in the classification algorithm: (1) normalized mean intensity of the EGF-Alexa 647 signal, (2) coefficient of variation from the 2-NBDG signal, and (3) length of the detected edge based on 2-NBDG. The features were selected sequentially in that order for improving performance of the algorithm; normalized mean intensity of the EGF-Alexa 647 signal was the single best feature, and each of the subsequent features improved algorithm performance. Addition of a fourth feature to the algorithm did not significantly improve performance.

A.   2-NBDG Mean Intensity

B.   EGF-Alexa 647 Mean Intensity

C.   2-NBDG Coefficient of Variation

D.   2-NBDG Length of Edge

Color Key: **Normal**   Mild Dysplasia   Moderate Dysplasia   Severe Dysplasia   Cancer
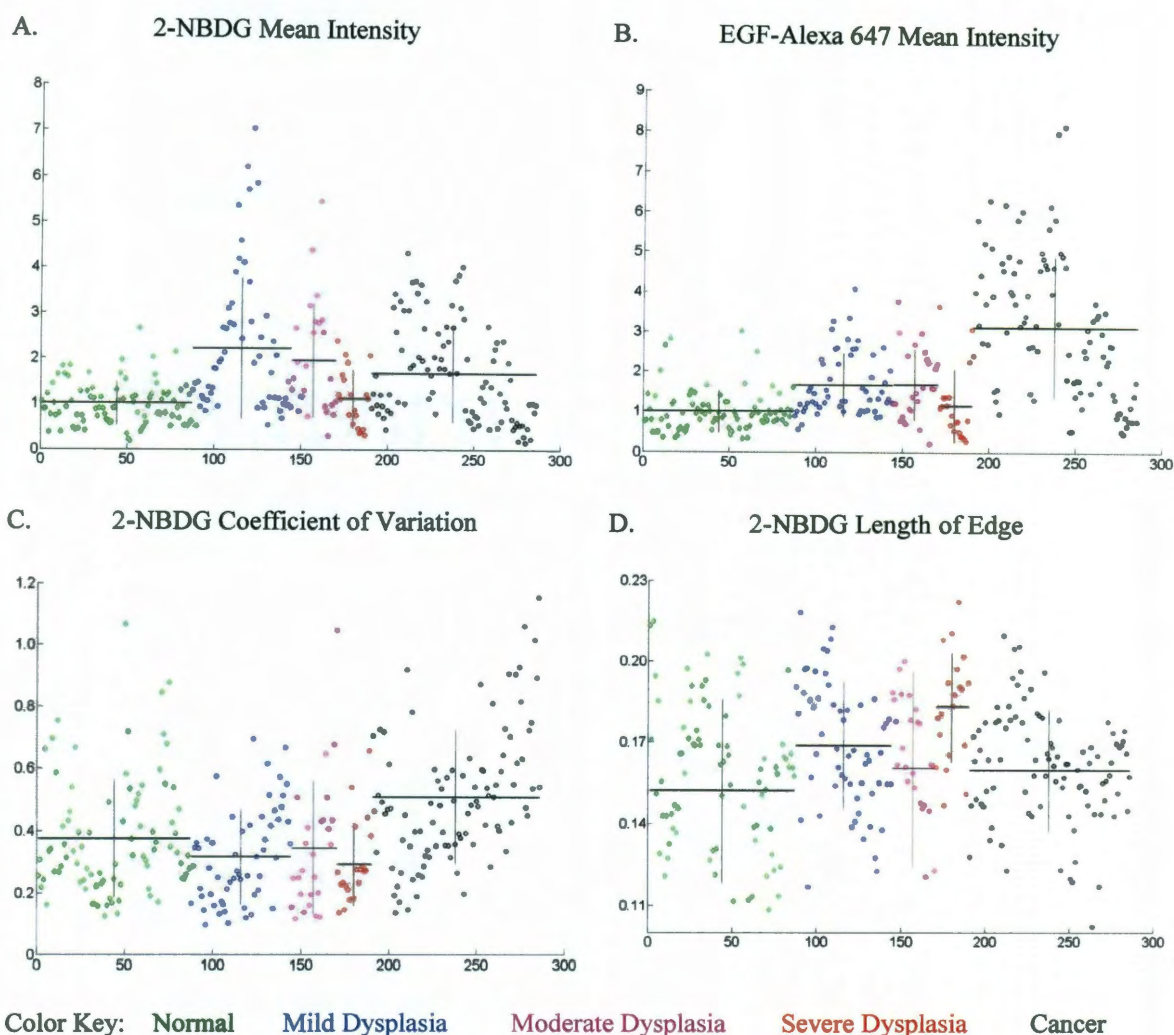
Figure 4-3. Scatter plots showing the distribution of feature values within the set of 286 regions, each point represents a single region. Regions are grouped by pathologic diagnosis with green indicating normal epithelium, blue indicating mild dysplasia, pink indicating moderate dysplasia, red indicating severe dysplasia, and black indicating cancer. Horizontal black lines indicate the mean feature value and vertical black lines indicate the standard deviation for each pathologic category. The scatter plots show the following features: (A) Mean intensity of the 2-NBDG signal, (B) Mean intensity of the EGF-Alexa 647 signal, (C) Coefficient of variation in the 2-NBDG signal, and (D) Length of edges detected by the Canny method in the 2-NBDG signal (helps with classification of severe dysplasia).

Figure 4-4A shows the resulting scatter plot of posterior probabilities grouped by histopathological diagnosis. The horizontal line at 0.41 indicates the cut-off point that

gives the best sensitivity and specificity of the algorithm. Any posterior probability above this value would be considered neoplastic by the classification algorithm, and any posterior probability below this value would be considered normal. This cut-off gives a sensitivity of 73% and a specificity of 77%. Figure 4-4B shows the receiver operator characteristic curve of the algorithm. The area under the curve (AUC) is 0.83, and the cut-off point yielding the highest sensitivity and specificity is marked with a blue circle.

A.

B.
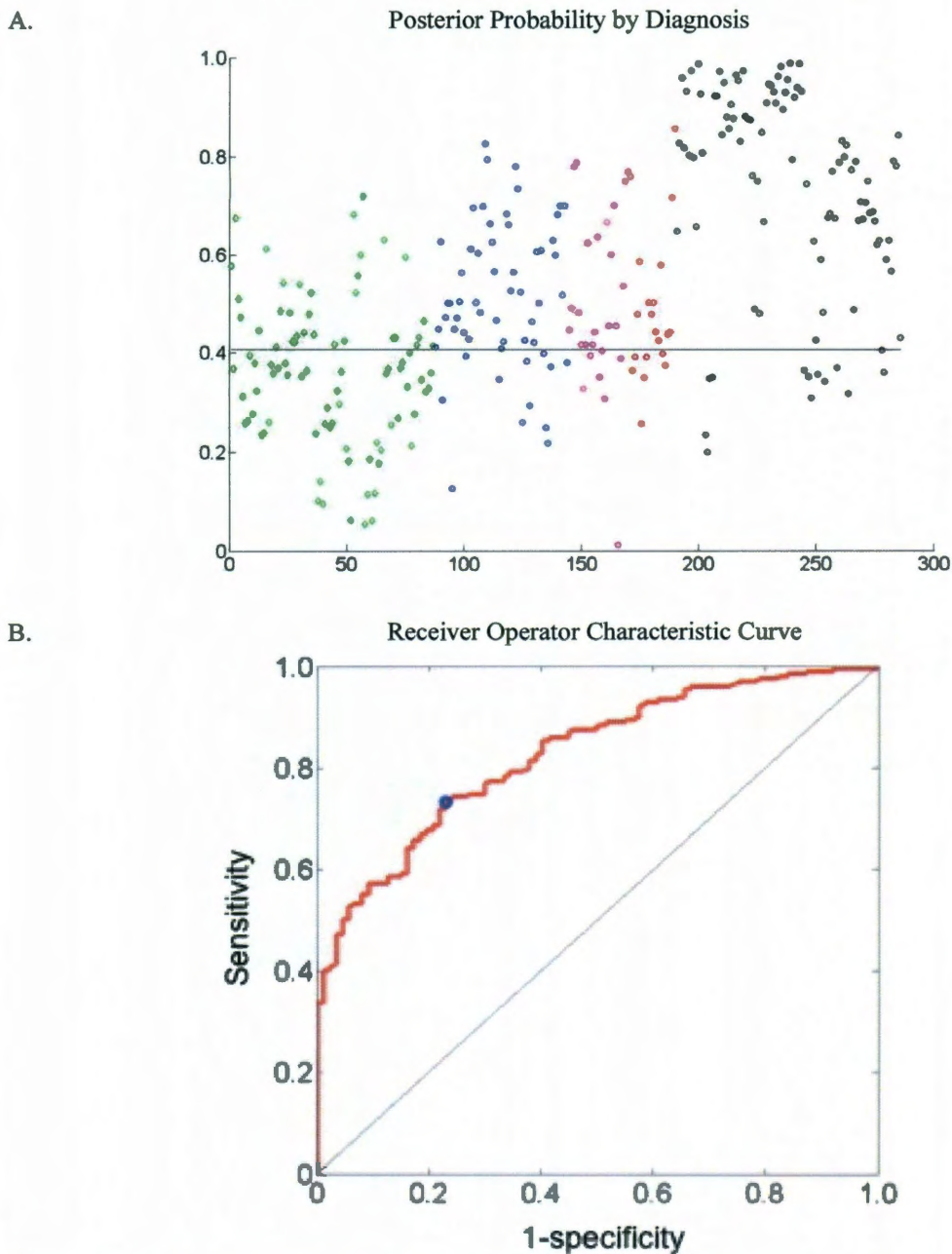
Figure 4-4. (A) Scatter plot of posterior probability by diagnosis using the algorithm. The horizontal line indicates the optimum cut-off at 0.41. (B) Receiver operator characteristic curve using a three feature classification algorithm. The operating point at the optimum cut-off is shown with a blue circle and results in a sensitivity of 73%, a specificity of 77%, and an area under the curve of 0.83.

Figure 4-5A displays the 50 x 50 pixel grid that was used to divide the image from a representative samples into new regions. While the originally evaluated regions as shown in Figure 4-2 were selected to contain only one diagnostic category and were oriented parallel to the pathology slices, the new evaluation grid is oriented parallel to the edges of the image and each region may contain multiple diagnostic categories. Figure 4-5B indicates the regions that were identified as having the highest posterior probability. Black stars indicate a posterior probability between 0.80-1.00 and gray stars indicate a posterior probability between 0.60-0.79. In this example, two adjacent regions have the highest level of posterior probability. According to the histopathology map, one of these regions contains mostly severe dysplasia, and the other contains mostly moderate dysplasia. Two regions with the second highest level of posterior probability were also identified, and these are also adjacent to one of the highest-level regions. Of these two regions, marked with a gray star, one contains mostly severe dysplasia and the other contains moderate dysplasia throughout. No part of any of these identified regions in this specimen contains normal epithelium.
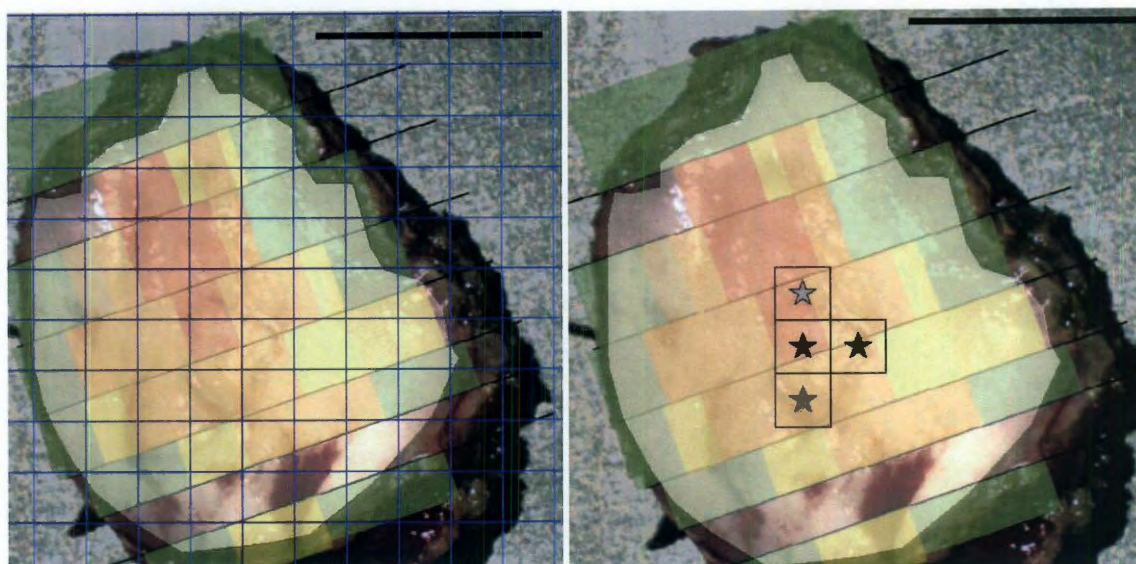
Posterior Probability Key: ★ 0.80-1.00 ⭐ 0.60-0.79

Figure 4-5. (A) Superimposed grid to divide each specimen into a new set of regions. Using the previously developed classification algorithm, posterior probabilities were calculated for each of these new regions of interest. (B) Based on two levels of posterior probability, regions identified as most likely to contain neoplasia were marked with black (posterior probability: 0.80-1.00) or gray (posterior probability: 0.60-0.79) stars. Scale bars are 1 cm.

Table 4-3 shows the results of how many 50 x 50 pixel regions were identified based on each posterior probability threshold, and how many of these regions contained mostly neoplasia. Out of the nine specimens, seven specimens contained at least one region that had a posterior probability between 0.80-1.00, for a total of 85 regions. Of these identified regions, 99% (84/85) contained >50% neoplasia. The remaining two specimens that did not have any regions identified within the highest-level category (#3 and #7) had multiple regions with posterior probabilities between 0.60-0.79. Among the 9 specimens, a total of 85 different regions were identified as having a posterior probability from 0.60-0.79. Of these regions, 95% (81/85) contained >50% neoplasia.

Table 4-3. Use of posterior probability to identify regions with the highest likelihood of disease

Specimen #	Regions with Posterior Probability of 0.80-1.00 Percent of regions containing >50% neoplasia	Regions with Posterior Probability of 0.60-0.79 Percent of regions containing >50% neoplasia
1	100% (2/2)	100% (2/2)
2	93% (13/14)	80% (4/5)
3	N/A	50% (1/2)
4	100% (1/1)	100% (15/15)
5	100% (25/25)	80% (8/10)
6	100% (31/31)	100% (8/8)
7	N/A	100% (3/3)
8	100% (11/11)	100% (24/24)
9	100% (1/1)	100% (16/16)
Total	99% (84/85)	95% (81/85)

Figure 4-6 shows for all the clinical samples the regions determined to have the highest posterior probability overlaid onto the corresponding histopathology maps. The black stars indicate the regions with posterior probability from 0.80-1.00, and the gray stars indicate the regions with posterior probability from 0.60-0.79. A few of the regions identified do not have corresponding gold standard histopathology information for the

entire area and so were not included in the analysis shown in Table 4-3. Use of posterior

probability to identify regions with the highest likelihood of disease, but are shown in

Figure 4-6.
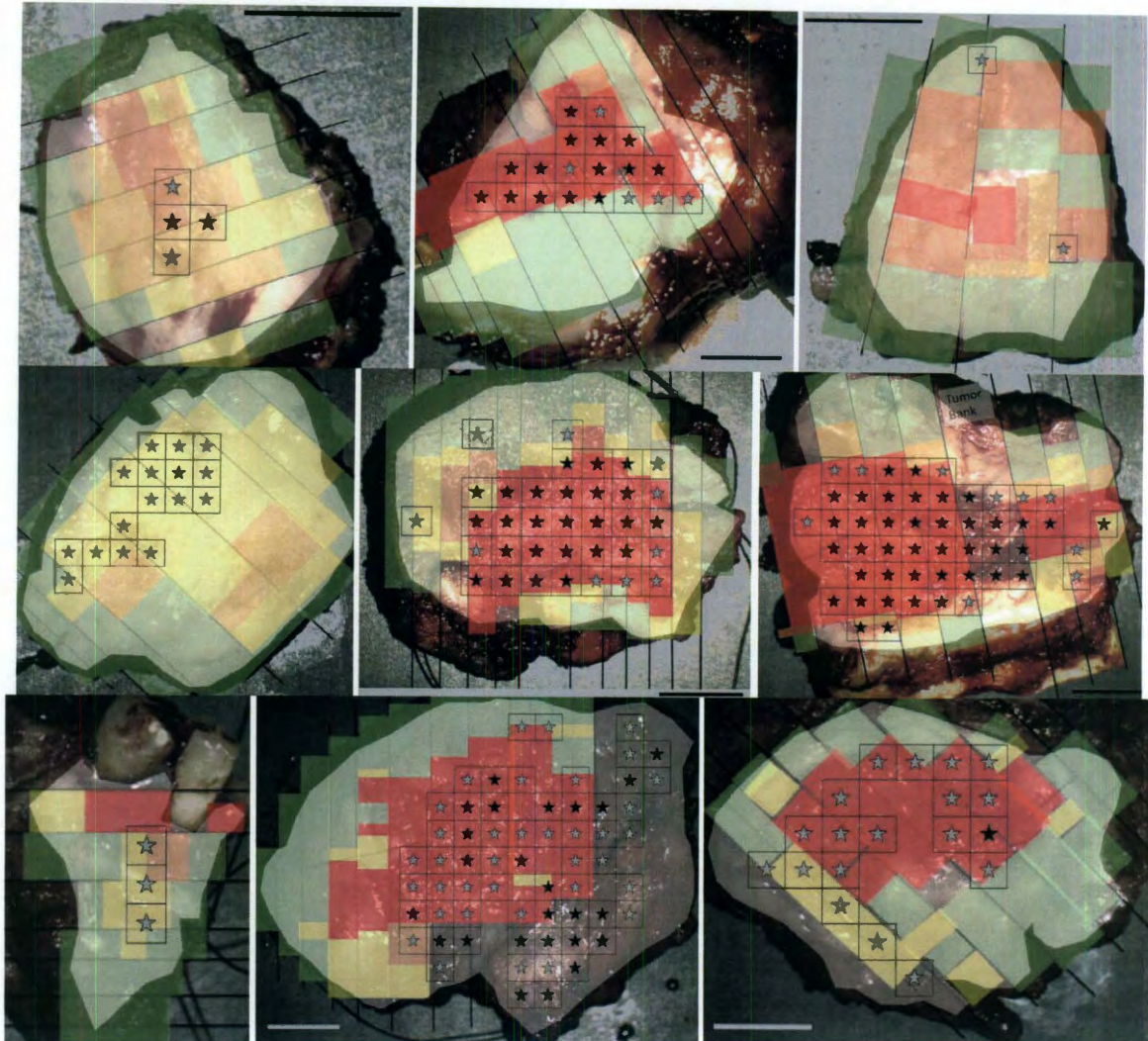
Figure 4-6. Based on two levels of posterior probability, regions identified as most likely to contain neoplasia were marked with black (posterior probability: 0.80-1.00) or gray (posterior probability: 0.60-0.79) stars. All clinical specimens examined are shown in this figure. Regions predicted to contain neoplasia have excellent agreement with the gold standard of histopathology. Scale bars are 1 cm.

This strategy has excellent agreement with histopathology, and while it does not identify all abnormal tissue, it identifies areas with the highest likelihood of disease in all samples.

4.5 Discussion

The optical imaging approach described in this study uses molecularly-targeted contrast agents to simultaneously assess two clinically relevant biomarkers in oral cancer: EGFR expression and metabolic activity. The benefit of this approach is that expression levels of multiple biomarkers can be assessed quantitatively over a large field of view and with high spatial resolution; this type of information cannot be obtained through the current practice of IHC or PET imaging. These targeted imaging agents can be topically applied to the epithelial surface, decreasing the dose required in comparison with intravenous injection and reducing consequent systemic toxicity concerns. This approach could be extended to include other biomarkers, if spectrally distinct imaging agents that specifically target the biomarker can be developed.

The classification algorithm described in this study identified regions with the highest likelihood of disease, areas that contained neoplasia 99% of the time. This objective assessment of accurately predicting the presence of disease has many clinical applications, including initial detection and diagnosis, selection of an appropriate biopsy site, monitoring treatment response, and monitoring patients for recurrence. This application is consistent with research recommended in 2010 in the Journal of the American Dental Association, which called for research projects to "identify factors that would increase clinicians' confidence and competence in identification and management

of potentially malignant lesions or early-stage malignancies, including the provision of surgical biopsies" [155].

Another potential use of a targeted optical imaging strategy could be in understanding the role of heterogeneity of biomarker expression in selection of therapy and predicting treatment response. EGFR expression is already a target in the FDA-approved monoclonal antibody therapy cetuximab, which is often used to treat recurrence of oral cancer. Other EGFR inhibitors (gefitinib, erlotinib, panatumumab, and lapatinib) have been approved for cancer treatment in other organ sites and are currently in clinical trials for head and neck cancer indications [156]. While in vitro data suggest a link between EGFR expression level and cytotoxicity of EGFR-targeted therapy, no definitive clinical correlation has yet been found [157-159]. As seen in the fluorescence images and IHC data shown here, EGFR expression is heterogeneous throughout a lesion. The ability to assess biomarker expression in vivo over a large sample using optical molecular imaging may elucidate the causes of this discrepancy and aid in the selection of patients who could benefit from EGFR-targeted therapy. For patients who respond, the benefits of EGFR-targeted therapy include the prevention of nodal metastases by blocking EGFR and potentially improved survival when combined with standard chemotherapy [160, 161]. As new EGFR-targeted therapies (such as nimotuzumab, zalutulumab, bevacizumab, and vandetanib) are developed and tested clinically for head and neck cancer indications, predicting which patients may benefit from a particular therapy will also aid in FDA approval [162, 163].

EGFR expression also has applications in other clinical settings. EGFR may help distinguish between leukoplakia with or without dysplasia since oral leukoplakia with

underlying dysplasia has increased expression of EGFR, which may be useful as an early marker of malignancy [143]. Additionally, EGFR mRNA levels were shown to be lower in non-malignant leukoplakias compared to contra-lateral normal appearing mucosa from the same patient, though both patient sites had significantly higher EGFR expression than healthy volunteers had [164]. This result and the idea of field cancerization help explain why it is important to normalize each patient's information to a normal site from the same patient. For optical imaging with topically applied contrast agents in vivo, a contra-lateral normal site could easily be assessed. Another clinical application of EGFR expression is in the identification of patients who would benefit from hyperfractionated accelerated radiotherapy [165, 166]. In pretreatment biopsies assessed for EGFR, patients with high EGFR expression had improved survival with hyperfractionated accelerated radiotherapy compared to a standard radiotherapy schedule. Identifying EGFR expression across the entire surface of the lesion may improve identification of patients who could benefit from this type of treatment. Finally, quantification of EGFR expression is difficult with current IHC methods, which may be one reason for conflicting findings in studies examining the prognostic value of EGFR in head and neck cancer [140]. Quantitative evaluation of optical molecular imaging of EGFR may help standardize measurement of EGFR expression level.

Metabolic activity as indicated by FDG-PET is currently used extensively in head and neck cancer for tumor staging, monitoring treatment response, and detecting residual or recurrent disease [167, 168]. FDG-PET has a high sensitivity and moderate specificity for detecting recurrent disease at the primary tumor site, but due to its inherently low spatial resolution, it is unable to detect lesions smaller than approximately 1 cm in size

[168]. FDG-PET is significantly better than clinical assessment and conventional imaging to monitor treatment response and has also been used as a marker of erlotinib response [169, 170]. Monitoring metabolic activity with FDG-PET can also identify residual disease and detect recurrence [168, 169, 171-173]. Although monitoring metabolic activity optically with 2-NBDG cannot accomplish any of the deep tissue applications of FDG-PET such as imaging of nodal metastases, it can be used to assess metabolic activity in the epithelium as shown in this study, a strategy which may be useful to detect residual or recurrent disease at the primary tumor site. The advantage of using 2-NBDG over FDG-PET is that optical imaging provides superior spatial and temporal resolution, does not expose the patient to ionizing radiation, and is far less expensive than PET imaging equipment and maintenance of cyclotron facilities.

Optical molecular imaging as applied in this study has some limitations, however. Though topical application of imaging agents may reduce dose and toxicity concerns, the agents are delivered only in the epithelium, preventing detection of submucosal disease. Inflammation in the oral cavity is a common confounder for detection aids, and inflammatory cells may also take up 2-NBDG, resulting in potential false positives from high metabolic activity of lymphocytes present in oral tissue due to benign conditions. Additionally, not all patients will have overexpression of EGFR, so that low fluorescence signal after application of EGF-Alexa 647 may not rule out the possibility of the presence of neoplasia. However, being able to obtain information from both agents in combination may help avoid the pitfalls of each agent alone. Another concern may arise from the idea of applying the epidermal growth factor, a mitogen, to a potentially neoplastic area. However, studies have demonstrated that pre-treatment of oral cancer lesions with EGF

actually improves the cytotoxicity of cisplatin, the most commonly used chemotherapy for head and neck cancer [174, 175].

Biomarkers have been studied for their potential use in detecting neoplasia, staging, selecting and monitoring therapy, detection of recurrence, and prognostic value, but the full picture of biomarker expression across an entire lesion is necessary to make accurate conclusions about the roles these biomarkers play in the disease process. Optical molecular imaging as demonstrated in this study of EGFR expression and metabolic activity in oral mucosa can reveal biomarker heterogeneity across a lesion and may serve as a research tool to understand cancer biology, develop new targeted therapies, or aid in the clinical management of cancer patients. With the proper imaging agents, this approach could be extended to monitor additional biomarkers in other types of epithelial neoplasia as well, and may eventually result in improved patient survival by allowing clinical care to be tailored to each patient's biomarker expression profile.

4.6 Acknowledgements

CHAPTER 5: HIGH-RESOLUTION FIBER OPTIC MICROSCOPY WITH FLUORESCENT CONTRAST ENHANCEMENT FOR THE IDENTIFICATION OF AXILLARY LYMPH NODE METASTASES IN BREAST CANCER: A PILOT STUDY[2]

5.1 Abstract

This prospective pilot study evaluates the potential of high-resolution fiber optic microscopy (HRFM) to identify lymph node metastases in breast cancer patients. 43 lymph nodes were collected from 14 consenting breast cancer patients. Proflavine dye was topically applied to lymph nodes ex vivo to allow visualization of nuclei. 242 images were collected at 105 sites with confirmed histopathologic diagnosis. Quantitative statistical features were calculated from images, assessed with one-way ANOVA, and were used to develop a classification algorithm with the goal of objectively discriminating between normal and metastatic tissue. A classification algorithm using mean image intensity and skewness achieved sensitivity of 79% (27/34) and specificity of 77% (55/71). This study demonstrates the technical feasibility and diagnostic potential of HRFM with fluorescent contrast in the ex vivo evaluation of lymph nodes from breast cancer patients [85].

5.2 Introduction

Breast cancer is the most common malignancy affecting women in North America and Europe, with approximately 200,000 new cases treated each year in the United States alone [176]. Treatment that involves surgical resection of the primary tumor often includes removal of axillary lymph nodes. The presence of axillary lymph node metastases is the most important prognostic factor for the patient, and determines appropriate adjuvant therapy after surgery [177]. However, axillary dissection is associated with significant short-term and long-term complications including lymphedema and upper extremity dysfunction in up to 50% of patients [178-180]. Identification and subsequent removal and assessment of the sentinel lymph node (SLN) has emerged as an alternative to full axillary dissection. This procedure has fewer complications than axillary dissection, however, there is potential for false negative events in 10-15% of patients [181-186]. This could result in understaging, which impacts adjuvant therapy recommendations, and the potential for regional recurrence in the axilla. An additional challenge for clinicians is the fact that touch imprint cytological analysis at the time of SLN surgery only identifies the presence of metastases in 50-80% of patients who have lymph node metastases [187]. A second surgical procedure is required when SLN metastases are identified on permanent histologic analysis in up to 35% of patients [188]. Therefore, additional methods to detect lymph node metastases intra-operatively have the potential to identify appropriate candidates for axillary dissection and avoid false negative events. Other clinical situations in which additional methods to detect lymph node metastases would be useful include patients with ductal carcinoma in situ for

whom operative removal of the SLN remains controversial or for pre-treatment staging of the axilla in patients who are candidates for neoadjuvant chemo- and endocrine therapy.

Current diagnostic approaches rely on optical imaging of stained cytological or histological specimens. Recent advances in optical imaging and optically active contrast agents allow high-resolution imaging of cell morphology and tissue architecture *in vivo* without the need for resection [188, 189]. High-resolution fiber optic microscopy (HRFM) is a new imaging technology that when used together with a fluorescent contrast agent, enables real time visualization of tissue with sub-cellular resolution *in vivo*. Proflavine is a fluorescent dye that stains nuclei [190]. HRFM with proflavine application has been investigated as a diagnostic tool to distinguish benign from malignant tissue in the oral cavity and esophagus [84, 86]. HRFM with proflavine staining has the potential to image cellular morphologic changes that are critical in the pathologic evaluation of lymph node metastases by exploiting the cell/nucleus size difference between carcinoma and lymphoid cells. Traditional histopathological analysis of lymph nodes in breast cancer patients identifies epithelial cell clusters, which are enlarged and crowded compared to normal lymphocytes, are hyperchromatic with hematoxylin and eosin (H&E) staining, and have an increased nuclear to cytoplasmic ratio [191]. In patients who have received preoperative chemotherapy, lymph nodes can contain stromal fibrosis and individual tumor cells may be embedded within the fibrosis.

The goal of this prospective study was to evaluate the potential of HRFM with proflavine staining for the detection of lymph node metastases in breast cancer patients. While this study was performed *ex vivo* as a proof of concept, HRFM with proflavine staining may eventually be performed *in vivo* and thus could play an important role in

clinical management of breast cancer patients, particularly for intra-operative assessment of lymph nodes in patients with early disease or for pre-treatment staging of the axilla.

5.3 Methods

The high-resolution microendoscope has previously been described in detail [84]. The HRFM instrument uses a light emitting diode (LED) with excitation light centered at 455 nm to excite proflavine fluorescence. A fiber-optic bundle composed of 30,000 fibers with a center-to-center spacing of approximately four μm transmits the light and is placed in direct contact with the surface to be imaged. The field of view comprises a circle that measures 750 μm in diameter. The system achieves a lateral resolution of 4.4 μm, sufficient to resolve individual cell nuclei. Figure 5-1 shows an optical diagram of the battery-powered HRFM instrument along with a photograph demonstrating the small size and portability of the instrument. The system can be assembled for $4,500.
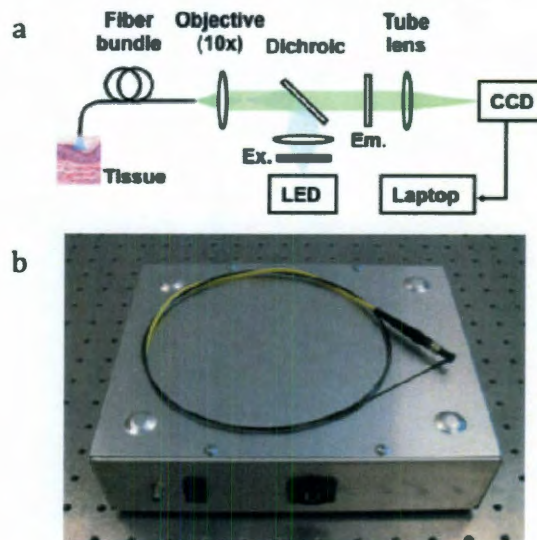
Figure 5-1. (a) Optical diagram of the high-resolution microendoscope (b) Photograph demonstrating the small size and portability of the battery-powered instrument

5.3.1 Clinical Study

Women 18 and older undergoing surgery for breast cancer that included a SLN biopsy followed by complete axillary lymph node dissection were eligible to participate in this study. Patients enrolled in this study gave written informed consent to participate, and the study was reviewed and approved by the institutional review boards at two academic institutions. To comply with HIPAA policies, patient data were labeled by accrual number.

Three to four representative fresh lymph node specimens were taken from each patient and prepared for imaging. To ensure that images were taken of areas representing normal lymphoid tissue and tumor metastases, a dedicated breast pathologist selected one lymph node that was grossly normal and one lymph node that showed gross metastasis. Other lymph nodes selected for imaging were grossly ambiguous. For some patients, all the lymph nodes appeared normal; in these cases three normal appearing nodes were imaged. A dedicated breast pathologist bisected each node to facilitate lymphoid tissue imaging.

Each lymph node was photographed and imaging sites were marked on the photograph to serve as reference points for histopathological correlation. A 0.01% solution (w/v) of proflavine hydrochloride (Sigma-Aldrich Corp., St. Louis, MO) was topically applied to the cut surface of the lymph nodes for approximately ten seconds. The fiber bundle of the HRFM instrument was placed in direct contact with the surface of the node for imaging. Multiple images were acquired from adjacent fields of view at each location on the specimen by translating the probe position approximately 1 mm. On

average, three nodes could be imaged at approximately ten sites within ten to fifteen minutes. Following imaging, the nodes were submitted for routine processing and H&E staining in specially labeled cassettes to facilitate direct imaging–histopathological correlation. A dedicated breast pathologist reviewed the axillary lymph nodes for metastases, and the final histopathological diagnosis was used as the gold standard for each imaging site. Imaging sites with unequivocal histopathological correlation were included in further analysis.

5.3.2 Image Analysis

Each image was reviewed to determine that quality control criteria were met. Images with motion artifacts or inadequate contact between fiber bundle and tissue were excluded from analysis. Each image that passed quality control was analyzed to identify quantitative features that could be useful to distinguish normal lymphoid tissue from metastases. Because adipose tissue is not useful in this distinction, all images were first cropped to remove regions of adipocytes and obtain a rectangular shaped field containing nuclei of lymphocytes or tumor cells. The dimensions of this field were variable because the region of each image containing nuclei of interest was also variable. A reference standard (captured in each image) was used to normalize pixel intensity values of the green channel of each corresponding image to account for any potential day-to-day variation in the HRFM instrument and to allow comparison between images with different exposure times.

Five image features were calculated from each normalized region (Matlab, Mathworks, CA). These features included: mean image intensity, standard deviation of image intensity, skewness, kurtosis, and entropy. Mean image intensity was selected as a

feature that may be useful to separate normal lymphoid tissue from metastatic tissue because malignant cells crowd together, are enlarged, and are hyperchromatic with H&E stain. Since proflavine stains nuclei, images containing malignant cells may have a higher intensity than images of normal lymphatic tissue. The remaining four features describe variations in pixel intensity throughout the image and were evaluated because the disruption of tissue architecture that occurs with metastasis may also alter the distribution of pixel intensity values. Standard deviation describes the spread of pixel values relative to the mean; high values of standard deviation correspond to a wider image histogram with a wide range of pixel intensities. Skewness describes asymmetry of the image histogram and indicates if pixel values are concentrated at low or high values. Positive skewness on a histogram occurs when there are more low values than high, negative skewness when there is a concentration on high values, and zero skewness describes a symmetric histogram. Kurtosis describes the peakedness of an image histogram and is sensitive to the size of the histogram tails. Entropy is a statistical measure of randomness that can be used to characterize the texture of an image. High values of entropy indicate greater randomness while low values of entropy result from a more uniform image. Each of these investigated features represents an objective, quantitative metric for assessing pixel intensity and distribution in an image.

Since multiple images of adjacent fields of view were obtained at each site in order to increase the region surveyed, the feature values calculated for each image were grouped by site and then averaged. A one-way ANOVA test was performed to compare average feature values from sites containing normal lymphoid tissue and sites containing metastases. For each feature, a classification algorithm was developed using linear

discriminant analysis to discriminate between normal lymphoid tissue and lymph nodes containing metastases, using histology as the gold standard. Because this was a pilot study with a relatively small number of measurements, the same data set was used to train the algorithm and test its performance. Sensitivity and specificity of classification were calculated for each of the five features. A receiver operator characteristic (ROC) curve was constructed and the area under the curve (AUC) was recorded. The two features with the best individual diagnostic performance were identified, and classification performance was also assessed when these two features were used together.

5.4 Results

A total of 43 lymph nodes were collected from 14 patients for imaging with HRFM; 13 patients had three nodes imaged and one had four nodes imaged. Of the 43 lymph nodes, 27 were normal and 16 were positive for metastases according to histopathology. A total of 126 independent sites were marked for diagnosis; at 105 of these sites the image was correlated with the histopathological diagnosis. 242 distinct images with adjacent fields of view were collected at these 105 sites. Of these images, 150 were of normal lymphoid tissue and 92 were of sites with metastases. Table 5-1 shows the distribution of data.

Table 5-1. Distribution of Collected Data from 43 Axillary Lymph Nodes in 14 Breast Cancer Patients

	Histologically Normal	Histologically Metastatic	Total
Axillary Lymph Nodes	27	16	43
Independent Sites with Histological Diagnosis	71	34	105
Images from Adjacent Fields of View	150	92	242

Figure 5-2 contains an HRFM image in which both adipose and lymphoid tissue are visible (Figure 5-2a). Adipocytes display a characteristic lobular structure, while lymphocytes are very small and more densely packed. Figure 5-2b shows the green channel of the field that was used to calculate feature values; the region containing adipocytes is cropped out. Figure 5-2c is the corresponding histology image.
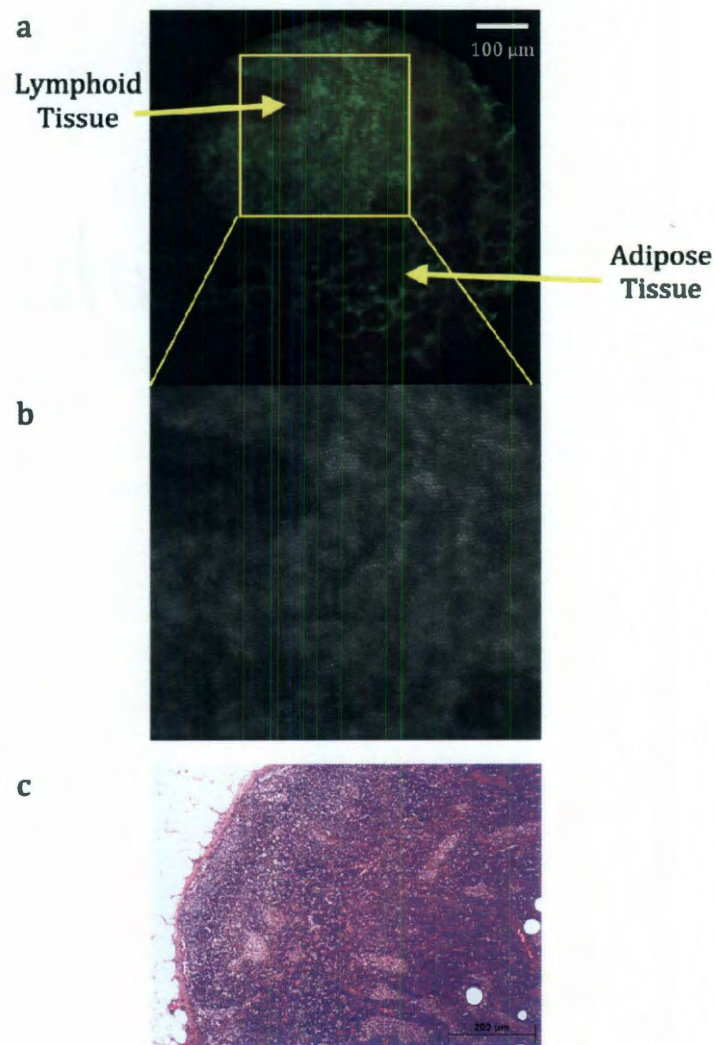
Figure 5-2. (a) High-resolution fiber optic microscopy (HRFM) image taken with from a histologically normal lymph node in a region containing both adipocytes and lymphocytes after application of proflavine to highlight cell nuclei (b) Green channel of

the image after cropping to remove adipocytes; quantitative features were calculated from this region (c) Corresponding histology at this site shows a normal lymph node. Capsule is thin and unremarkable. Fat surrounds the node. The node is populated with uniform, small, round lymphocytes.

Figure 5-3 illustrates representative results from a set of lymph nodes from a single patient. Figure 5-3a shows the photograph of three bisected nodes with eight imaging sites marked in blue for subsequent pathologic correlation. After examining the corresponding H&E slides, a dedicated breast pathologist determined that the node on the left was positive for metastases, with a negative periphery. The node in the middle was negative for metastases. Images collected from both of these nodes could be used in image analysis because the measurement site could be correlated to a histopathology gold standard. The node on the right was determined to be positive with very small subtle occasional single tumor cells with no dominant mass. Images from this node were not used in further analysis because it was difficult to determine if HRFM measured a site containing a few tumor cells or not. Figure 5-3b shows representative HRFM images collected at Sites 4 and 7 in the photograph. The HRFM image from site 7 has larger, more crowded nuclei and the average image intensity is greater as a result. The HRFM image from site 4 has smaller nuclei that are spaced farther apart; the average image intensity is lower because the cells are not as densely packed. The corresponding H&E images for these sites are shown in Figure 5-3c. The H&E image of site 7 indicates nests of tumor cells, while that of site 4 shows a normal node with sinus histiocytosis. Figure 5-3d depicts the image histograms that were obtained for each field shown in Figure 5-3b. The red histogram corresponds to the image obtained from site 7 (metastatic), while the blue histogram corresponds to the image obtained from site 4 (normal lymphoid

tissue). Calculated feature values for each image are indicated. The metastatic site has a higher mean intensity than the normal site as seen by the shift in the center of the image histogram. Low skewness is noted in the metastatic site, indicating a more symmetrical histogram, while high skewness is noted in the normal site as a result of more pixel values concentrated at lower intensities with a long tail at higher intensity values. Kurtosis is higher for the normal site as seen by the sharp, high peak in the histogram, while the histogram of the metastatic site has a broader peak with lower kurtosis. The metastatic site has higher entropy, which indicates that the image is more random than the normal site. Standard deviation is higher in the metastatic site as seen by the wider distribution of pixel values around the mean as compared to the normal site.
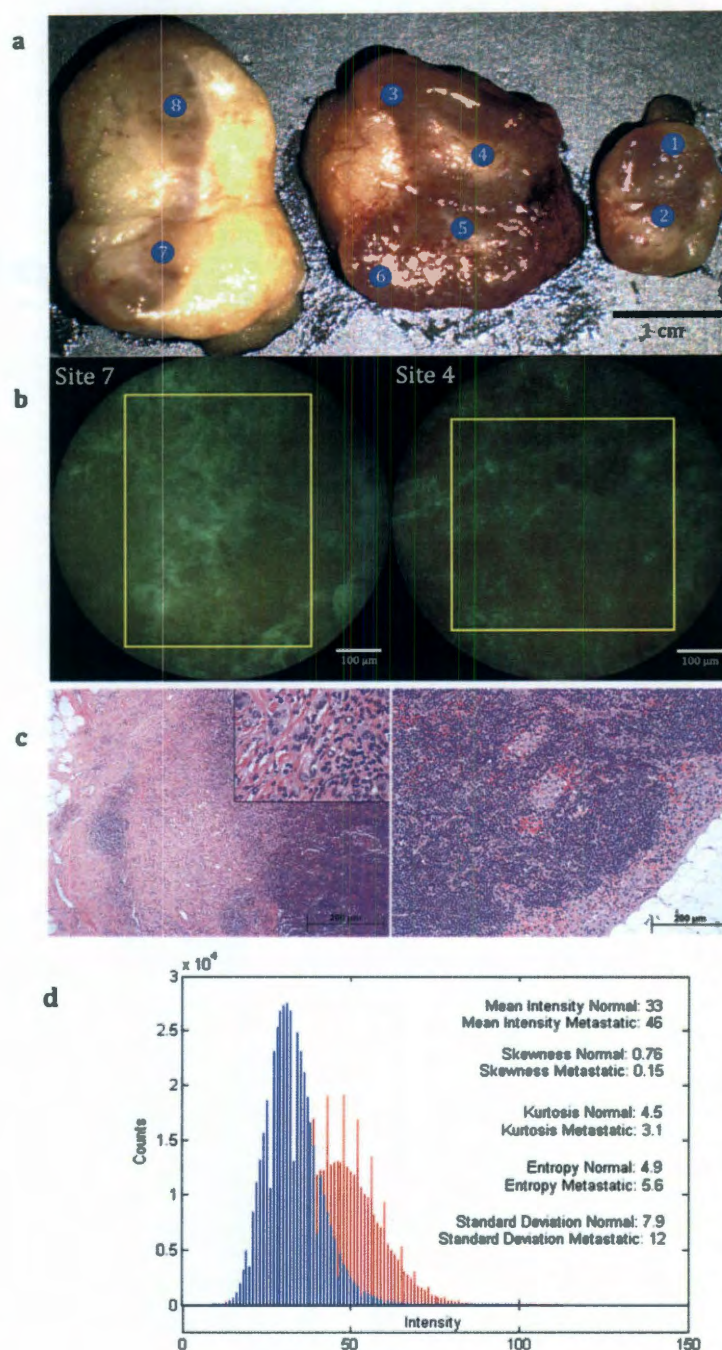
Figure 5-3. (a) Photograph of three lymph nodes from a single patient with imaging sites marked in blue for correlation to pathology (b) HRFM images collected from sites 7 and 4 with cropped region of interest indicated: site 7 contains metastases while site 4 is normal lymphatic tissue (c) Corresponding H&E images for these sites: The image from site 7 shows that metastatic carcinoma has replaced part of the lymph node. Dense fibrosis surrounds the metastatic tumor cells. Insert shows high power magnification (40X) of tumor cells. The neoplastic cells are arranged in nests and have amphophilic, vacuolated cytoplasms and prominent nuclei. The image from site 4 shows a normal

lymph node with sinus histiocytosis. The lymph node capsule is thin and the sub-
capsular sinus contains reactive histiocytes. (d) Image histograms from each region of
interest; site 7 is shown in red while site 4 is shown in blue. Calculated feature values for
each image are also indicated.

Figure 5-4 shows box plots of the average feature values for each diagnostic

category. Red boxes represent feature values from sites containing metastases, while

blue boxes represent normal sites. All feature values were normalized to the median

value of the normal lymphoid tissue set in order to show the range of values on a

consistent scale. P-values from a one-way ANOVA test for each feature are also

included in Figure 5-4, and the features are listed in order from lowest p-value to highest.

The average feature values of normal lymphoid tissue are statistically significantly

different from the feature values of metastatic tissue for all five features ($p < 0.05$).
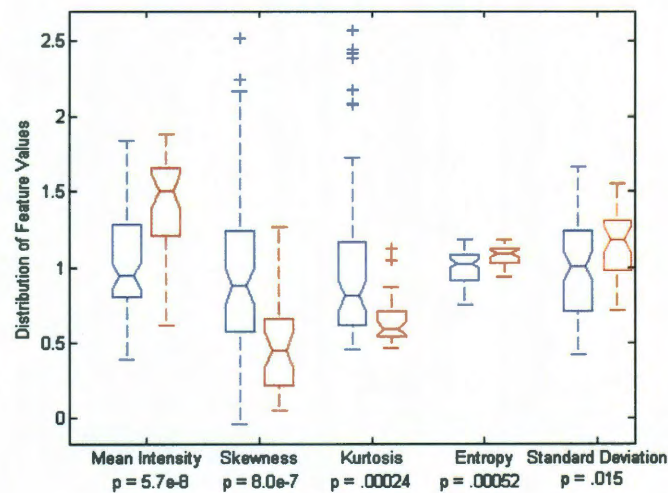
Figure 5-4. Box plots showing feature values for images separated by diagnostic
category. Values from images containing normal lymphatic tissue are shown in blue,
while values from images containing metastases are red. All values are normalized to the
median value of the normal set in order to show all features on the same scale. P-values
obtained from a one-way ANOVA test are listed for each feature.

Table 5-2 ranks the diagnostic performance of each of the five image features by linear discriminant analysis, listed in order from highest to lowest AUC. Mean image intensity and skewness were the two highest performing features, each with an AUC of 0.81. This order of performance is consistent with the p-values for each feature (Figure 5-4).

Table 5-2. Feature Performance

	Quantitative Feature	Sensitivity	Specificity	AUC
1	Mean image intensity	82% (28/34)	69% (49/71)	0.81
2	Skewness	85% (29/34)	66% (47/71)	0.81
3	Kurtosis	71% (24/34)	73% (52/71)	0.76
4	Entropy	59% (20/34)	76% (54/71)	0.70
5	Standard deviation	65% (22/34)	65% (46/71)	0.64

Figure 5-5 illustrates results when the top performing two individual features, mean image intensity and skewness, were combined. Figure 5-5a shows a scatter plot of mean intensity versus skewness for each image; both features provide discriminatory ability. Figure 5-5b shows the ROC curve for the algorithm developed using both features. The resulting AUC improved to 0.84. At the Q-point of the ROC curve, sensitivity and specificity with this two-feature algorithm were 79% (27/34) and 77% (55/71), respectively. An AUC value of 0.85 was obtained when the data were randomly divided into training and test groups by patient, with all images from a specific patient assigned to either testing or training. This simulates the process of collecting a training group to train the algorithm, and then collecting a separate patient set for testing, so it is encouraging that the performance is nearly identical to the results obtained when the entire data set was used for both training and testing. Although performance of the algorithm could improve slightly if all five of the investigated features were used in

combination, this would likely result in overtraining of the algorithm due to the small size of the data set from this pilot study, and so the algorithm was limited to only two combined features.
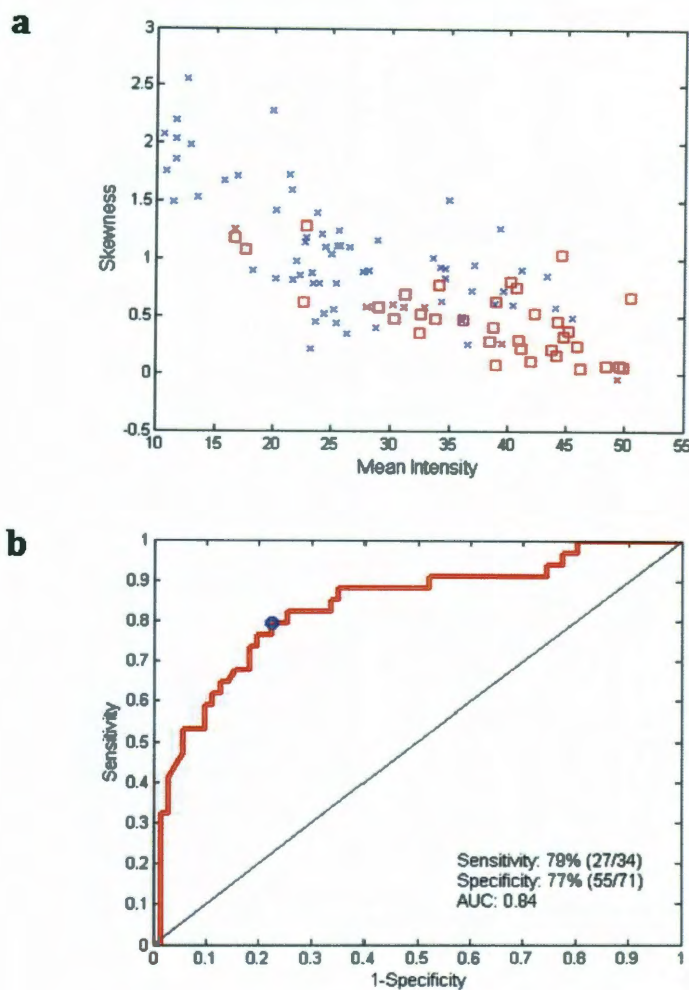
Figure 5-5. (a) Scatter plot by site of mean intensity and skewness: normal sites are shown as a blue 'x' while metastatic sites are shown as a red square. (b) ROC curve obtained from a classification algorithm using linear discriminant analysis with both mean intensity and skewness as features

5.5 Discussion

This pilot study demonstrates the technical feasibility of *ex vivo* HRFM with proflavine contrast enhanced fluorescence imaging to visualize cell nuclei in axillary lymph nodes from breast cancer patients. These preliminary results demonstrate encouraging diagnostic potential of this fluorescence molecular imaging modality to identify lymph nodes containing metastases. Using the image features of mean intensity and skewness, a classification algorithm separating normal lymphoid tissue from tissue containing metastases was developed that could achieve an AUC of 0.84. This compares with the reported sensitivity and specificity of current standard preoperative sonographic methods of evaluating axillary nodes; a recent review of 16 published studies described sensitivity ranging between 49-87%, and specificity between 56-97% [192]. One comparative advantage of optical imaging is the high resolution, which may make this technology more useful for detecting microscopic disease.

Differences observed in these image features are consistent with qualitative differences observed between images from normal lymphoid tissue and metastatic regions. Images obtained from metastatic sites appear brighter (higher mean image intensity) than images obtained from normal lymphoid tissue. This is due to the enlarged, crowded nuclei present in tumor cells, while normal lymphocytes have small nuclei that are spaced further apart. Higher mean intensity may also reflect the higher occurrence of diploidy and multiploidy and increased genetic material in cancer cells. Because images of normal lymph nodes have nuclei that are spaced further apart, there are more dark pixels, resulting in a positive skewness. Images of metastatic nodes have fewer low pixel values due to crowding and enlargement of nuclei and therefore have lower skewness.

Calculations to determine mean intensity and skewness of an image can be performed extremely rapidly, potentially allowing a classification prediction in near real time. The step of cropping the image is critical for quality control, as acellular regions of fibrosis or folding of the tissue were occasionally observed to also display brighter fluorescence signal. This demonstrates why the high resolution imaging itself is important; simple intensity measurements would not be able to distinguish between tissue types. Though choosing a region that contains only nuclei could potentially introduce some user bias, this step prevents some false positive results.

While this pilot study demonstrates encouraging results regarding the technical feasibility of HRFM with proflavine to visualize cell nuclei in axillary lymph nodes from breast cancer patients and the diagnostic potential of HRFM with proflavine to differentiate benign from malignant axillary lymph nodes using quantitative image features of mean intensity and skewness, future studies are needed to evaluate the diagnostic performance of the imaging method in a larger, independent validation set of patients. Additional improvements to this technique include increasing the size of the fiber bundle to twice the current diameter, thereby increasing the field of view four-fold. Expanding the area that can be optically interrogated could improve the ability to detect metastatic cells by more efficiently imaging a lymph node with decreased imaging time. Future clinical studies will also attempt to determine the minimum size of metastasis that can be detected with this system.

The prognostic relevance of isolated tumor cells and micrometastases in lymph nodes from patients with breast cancer has become a major area of interest in tandem with the increased identification of this low volume disease due to the practice of SLN

biopsy [193]. There is also heightened interest in the evaluation of the SLNs after neoadjuvant chemotherapy, where the proportion of micrometastases is reportedly higher, and the performance of intraoperative imprint cytology of SLNs is proportionately lower [194].

Many functional and molecular imaging techniques are being challenged to detect metastatic disease at the microscopic level in SLNs [195-197]. Noninvasive, non-ionizing, and high-resolution mapping of SLNs in conjunction with minimally invasive techniques, such as fine needle aspiration biopsy, is currently being investigated in multiple active preclinical protocols. While HRFM has good spatial resolution and high collection speed using current instrumentation, the current limitation for *in vivo* HRFM of lymph nodes is depth penetration. A potential resolution to this limitation is the in situ delivery of HRFM (i.e. endoscopy via a biopsy needle) for real-time *in vivo* interrogation of lymph nodes that are assessed preoperatively with ultrasound. The additional costs of performing imaging and imaging-guided biopsies may be balanced on average by cost savings from avoiding SLN evaluations for patients with documented nodal metastases preoperatively [198]. An aspect of this technique that may limit speed of translation to the clinic is the necessary approval process from the United States Food and Drug Administration (FDA) to use proflavine in human subjects. However, these pilot studies are necessary to provide the foundation for future pursuit of human trials. Optical imaging can be performed very rapidly, allowing a large area to be surveyed in a short time, making it an attractive technology for this application. An advantage of optical imaging over traditional histopathology is that this rapid imaging can be performed *in vivo*. However, the intent of this technology is to augment current standards of care, not

to attempt to replace the gold standard of histopathology. The role of HRFM in the future may be best suited for intra-operatively identifying candidates for full axillary dissection, thus preventing the need for a second surgery in some patients, or for preoperative staging of axilla.

These preliminary results demonstrate the technical feasibility and diagnostic potential of quantitative molecular imaging using HRFM with proflavine fluorescent staining to discriminate between normal and metastatic axillary lymph nodes *ex vivo* in breast cancer patients. This rapid technique is simple, inexpensive, and can potentially be exploited to augment patient care by providing an alternative technique for the detection of micrometastases while requiring fewer resources and expertise.

5.6 Acknowledgements

CHAPTER 6: MULTIMODAL CONTRAST AGENTS FOR MAGNETIC RESONANCE AND OPTICAL IMAGING

6.1 Abstract

Non-invasive imaging plays an important role in both fundamental cancer research and clinical management of patients. To exploit the advantages of non-invasive imaging as a tool in research and in the clinic, we have developed multimodal contrast agents that are functional for both magnetic resonance and optical imaging. Molecularly-targeted optical imaging is achieved by using an antibody to the epidermal growth factor receptor that has been conjugated to an Alexa Fluor 647 dye. Gadolinium-based contrast agents (Gd-CAs) such as the clinically approved agent Magnevist® and ultra-short carbon nanotubes (US-tubes) doped with gadolinium provide enhancement of signal for magnetic resonance imaging (MRI). Gd-CAs and antibody-dye conjugates were sequentially co-loaded into nanoporous structured silicon microparticles 1.0 micrometers in diameter. It has been previously demonstrated that loading Gd-CAs into silicon discs increases relaxivity, thus improving sensitivity of detection [199]. The loading efficiency of the antibody-dye conjugate into these silicon discs with and without Gd-CAs was quantified using a fluorometer. The highest loading efficiency of the antibody-dye conjugate obtained (27%) was achieved during co-loading with Magnevist(R) in small pore size silicon discs. The loading remained variable between samples; the standard deviation of cumulative loading in five samples was 47% of the mean. However, the optical signal within the silicon discs in all samples was easily visualized using a Zeiss

LSM 510 Meta Confocal Microscope. Eventually, the biodistribution of this agent in a tumor model could be explored for applications in cancer diagnostics and imaging.

6.2 Introduction

Non-invasive imaging plays an important role in both fundamental cancer research and clinical management of patients. While my previous research focused solely on optical imaging, several other types of non-invasive imaging are currently utilized in clinical practice. These include magnetic resonance imaging (MRI), positron emission tomography (PET), ultrasound (US), computed tomography (CT) and single positron emission computed tomography (SPECT). While some of these modalities can operate without exogenous contrast agents (MRI, US, CT), incorporation of exogenous agents can provide functional information or improve image contrast. Each modality has strengths and weaknesses such as the resolution or depth of penetration, so it is important to select an appropriate imaging modality for a clinical application [200, 201]. As described in the studies presented in previous chapters of this thesis, optical imaging can detect signal originating from the surface of tissue or explore deep tissue when an optical probe is inserted through a needle. However, it is difficult to apply optical techniques to imaging deep tissue because of limits to the depth of photon penetration through tissue.

In many cases, combining imaging modalities may allow you to draw from the strengths of each modality in order to get a better overall assessment of a clinical problem. Because of this potential, multimodal imaging is a rapidly growing field [202]. In this study, a multimodal contrast agent that is both optically active and improves contrast in magnetic resonance imaging is developed and characterized. By combining MRI and optical imaging, anatomic information can be obtained from the MRI signal,

and high resolution molecular-specific information can be obtained from the optical signal. Previously developed multimodal MRI and optical imaging agents have either physically conjugated an optical agent to an iron oxide core [203] or gadolinium-based compound [204, 205], or encapsulated different MRI and optical probes together within a liposome [206]. Physical conjugation results in a co-localized signal from both modalities (unless the linker molecule is enzymatically degraded), but agents encapsulated together may result in a distinct biodistribution pattern once the liposome or other carrier vesicle breaks down. In this study, MRI agents are co-loaded into a silicon disc carrier agent along with an optically active antibody. This approach is similar to liposomic encapsulation because the two agents are not physically conjugated. This study characterizes the efficiency and variability of loading of the antibody-dye conjugate into silicon discs and the release of the antibody over time.

6.3 Materials and Methods

An antibody to the epidermal growth factor receptor (Baylor College of Medicine Monoclonal Antibody Facility, Houston, TX) was conjugated to an Alexa Flour 647 carboxylic acid, succinimidyl-ester (Invitrogen, Carlsbad, CA). Excess free dye was removed using Zeba Spin Desalting columns with a 7 kDa molecular weight cut-off (Thermo Scientific Pierce, Rockford, IL). The final concentration of this antibody-dye conjugate was 0.83 mg/mL.

Two different gadolinium-based contrast agents (Gd-CAs) were investigated in this study: Magnevist®, a clinically approved Gd^{3+} polyaminocarboxylate complex, and gadonanotubes (GNTs), a nanoscale carbon-based tube structure doped with Gd^{3+} ions. Magnevist® is commercially available (Bayer Healthcare Pharmaceuticals, Wayne,

USA), and was used at a loading concentration of 1 mM. GNTs were obtained from Lon Wilson's lab in the Chemistry Department at Rice University, and were synthesized as described in previous literature [199, 207]. GNTs were used at a loading concentration of 0.2 mM.

Silicon discs with a diameter of 1 micrometer and height of 0.4 micrometers were obtained from Paolo Decuzzi's lab at the Methodist Hospital Research Institute in Houston, Texas. Small pore size discs had an average pore diameter of approximately 10 nanometers, and huge pore size discs had an average pore diameter of around 40 nanometers. The chemical fabrication of these silicon discs has been described previously [199, 208].

6.3.1 Co-loading of Silicon Discs

To load silicon discs with both the magnetically active contrast agent and the EGFR-targeted optical imaging agent, the following steps were performed:

(1) Begin with 10^8 silicon discs (dry)

(2) Loading: add 100 μL of Gd-CA

(3) Sonicate solution for 10 minutes

(4) Centrifuge for 10 minutes at 1000 rpm

(5) Remove supernatant containing free Gd-CAs

(6) Washing: add 100 μL of water

(7) Centrifuge for 10 minutes at 1000 rpm

(8) Remove supernatant containing free Gd-CAs

(9) Repeat steps 2-8 twice for a total of 3 loading and washing steps with Gd-CA

(10)   Loading: add 100 μL of antibody-dye solution

(11)   Sonicate solution for 10 minutes

(12)   Centrifuge for 10 minutes at 1000 rpm

(13)   Remove supernatant containing free antibody-dye

(14)   Washing: add 100 μL of water

(15)   Centrifuge for 10 minutes at 1000 rpm

(16)   Remove supernatant containing free antibody-dye

(17)   Repeat steps 2-8 twice for a total of 3 loading and washing steps with the antibody-dye

(18)   Reconstitute sample in 100 μL of water or phosphate buffered saline (PBS).

Control samples in which only antibody-dye conjugate was loaded into the silicon discs were also prepared. In this case, the steps to load the Gd-CA were skipped (steps 2-9), but the remaining steps were performed as indicated above. Control samples containing only Gd-CA and no optical agent were prepared by ending the previously described process after completion of step 9. When Magnevist® was co-loaded into the silicon discs with the antibody-dye, the loading steps were combined and equal parts (50 μL each) of Magnevist® and antibody-dye were added simultaneously to the particles.

6.3.2   Quantification of Antibody-Dye Loading

To quantify the efficiency of loading the antibody-dye conjugate into the pores in the silicon discs, the supernatant that was removed during the loading and washing steps was analyzed in the SPEX Fluorolog-3 fluorometer (Horiba Jobin Yvon Inc., Edison, NJ). 10 μL of supernatant was diluted in Milli-Q water (Millipore, Billerica, MA) to a total volume of 4 mL in a quartz cuvette. The original antibody-dye conjugate was used

as a control measurement of fluorescence to which each supernatant sample was normalized. Fluorescence intensity at peak emission (670 nm) was used. Based on the fraction of antibody-dye remaining in the supernatant as measured in the fluorometer, the fraction of antibody-dye that was loaded into the silicon discs could be calculated indirectly. The final sample containing the loaded silicon discs was also measured directly in the fluorometer.

6.3.3 Confirmation of Antibody-Dye Loading

To confirm that the optically active antibody-dye conjugate was loaded into the pores within the silicon disc, the samples were imaged with a Zeiss LSM 510 Meta Confocal Microscope with appropriate excitation and emission filters.

6.3.4 Monitoring Release of Antibody-Dye Over Time

The silicon discs used in this study will degrade over time in the presence of salts, releasing the optically active component of this multimodal imaging agent. To characterize the release of antibody-dye from the silicon discs over time, the samples were reconstituted in PBS and placed in an incubator to simulate a physiologically relevant environment. At time intervals including 0, 1, 4, 9, 24, 48, and 72 hours, the samples were centrifuged and the supernatant was removed and measured in the fluorometer as previously described. 100 uL of PBS was used to reconstitute the dry sample. The sample itself was also measured directly at each time point. An antibody-dye only control sample kept in the incubator was measured at each time point as a fluorescence reference.

6.4 Results

6.4.1 Quantification of Antibody-Dye Loading

Antibody-dye conjugate was co-loaded with Magnevist® in small pore (10 nm) sized silicon discs as described in the methods above. Based on the indirect method of determining efficiency of loading by measuring supernatants, this combination of Gd-CA and pore size resulted in 27% of the antibody-dye being incorporated into the silicon discs on average (n=5). The indirect method was chosen over the direct measurement of the loaded samples due to concerns of dye self-quenching while in close proximity within the silicon disc, and also possible quenching of the dye by the Gd-CA. Figure 6-1 shows the efficiency of loading by step in each of the five samples. The y-axis in this graph and the following graphs is the fraction of antibody that was loaded out of the amount added in each step. On average, step 1 loaded 40% of the available antibody-dye with a standard deviation that was 55% of the mean, step 2 loaded 14% with a standard deviation that was 53% of the mean, and step 3 loaded 26% of the available antibody dye with a standard deviation that was 63% of the mean. Figure 6-2 shows the average loading efficiency per step.
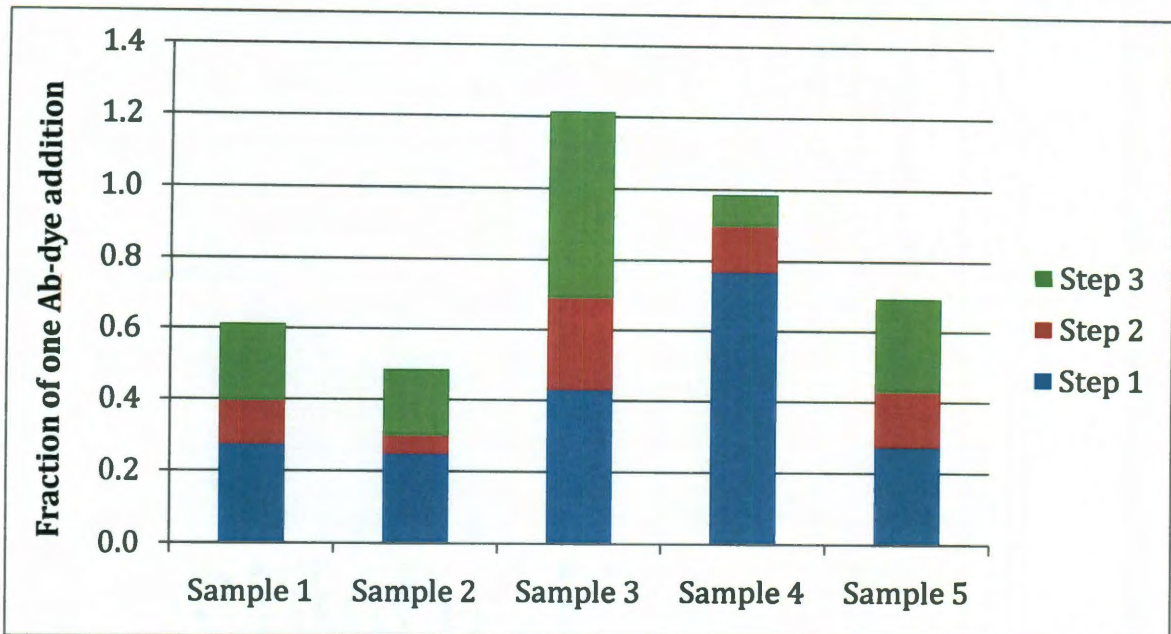
Figure 6-1. Efficiency of antibody-dye loading in small pore sized silicon discs co-loaded with Magnevist®
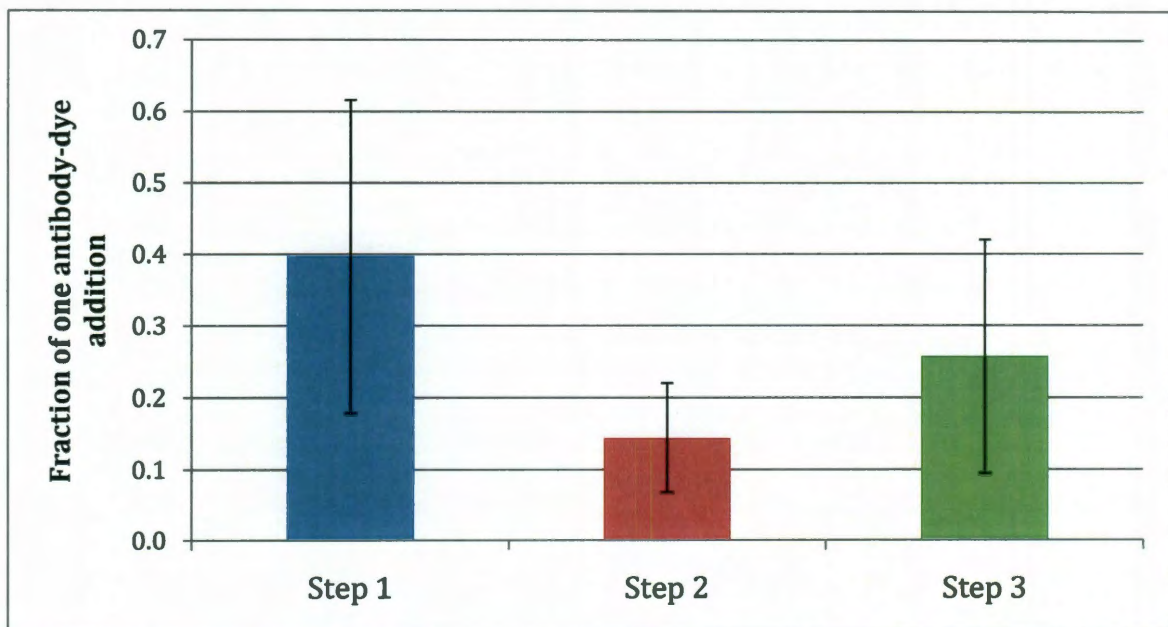
Figure 6-2. Average loading efficiency of the antibody-dye by step in small pore sized silicon discs co-loaded with Magnevist®

When the cumulative efficiency of loading was examined to determine the overall variability of loading between different samples, the final variability after step 3 was 47% of the mean. Figure 6-3 shows the cumulative loading fraction after each step.
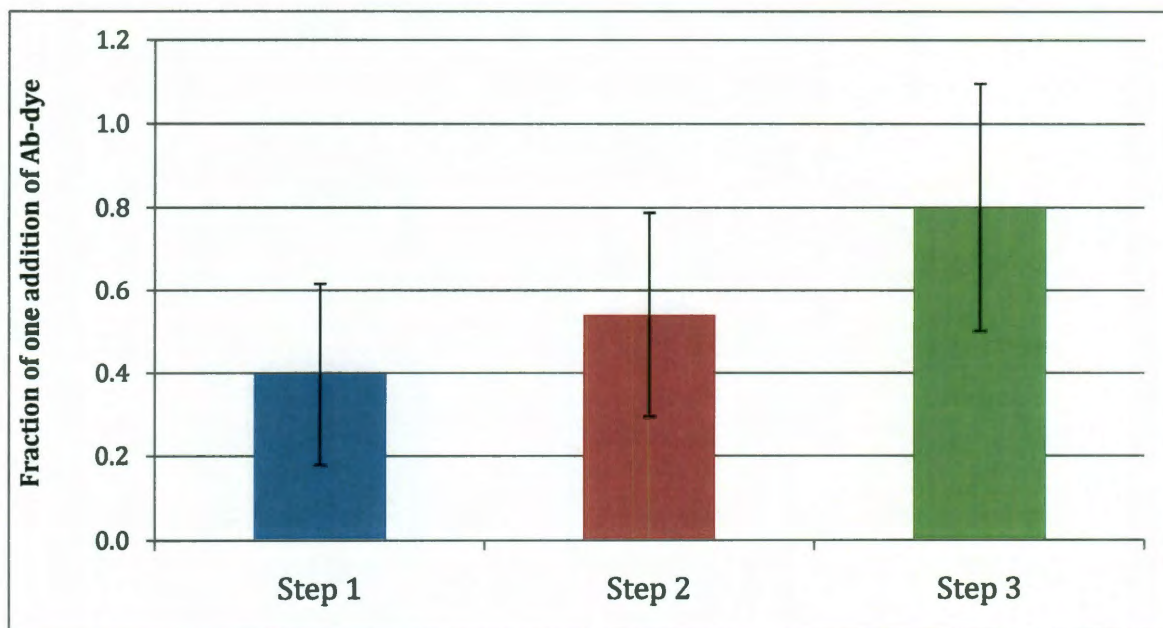
Figure 6-3. Cumulative fraction of antibody-dye loaded after each step in small pore sized silicon discs co-loaded with Magnevist ®

The antibody-dye conjugate was also loaded into silicon discs with huge size pores of about 40 nm in diameter, both alone and with co-loading of GNTs. The efficiency of loading in these combinations was just as variable and but less efficient than the results shown previously, and will not be detailed in this thesis.

6.4.2 Confirmation of Antibody-Dye Loading

Confocal imaging was used to confirm that the multimodal imaging agents were optically active as expected. All samples loaded with antibody-dye conjugate were easily visualized using the fluorescence microscope, whether or not Gd-CAs were also loaded.

Control samples of silicon discs alone or silicon discs with only Gd-CA (Magnevist® or GNTs) had no detectable fluorescence signal. Figure 6-4 shows an example image from a small pore size silicon disc sample co-loaded with antibody-dye and Magnevist®. 633 nm laser power was 50% and gain was 450.
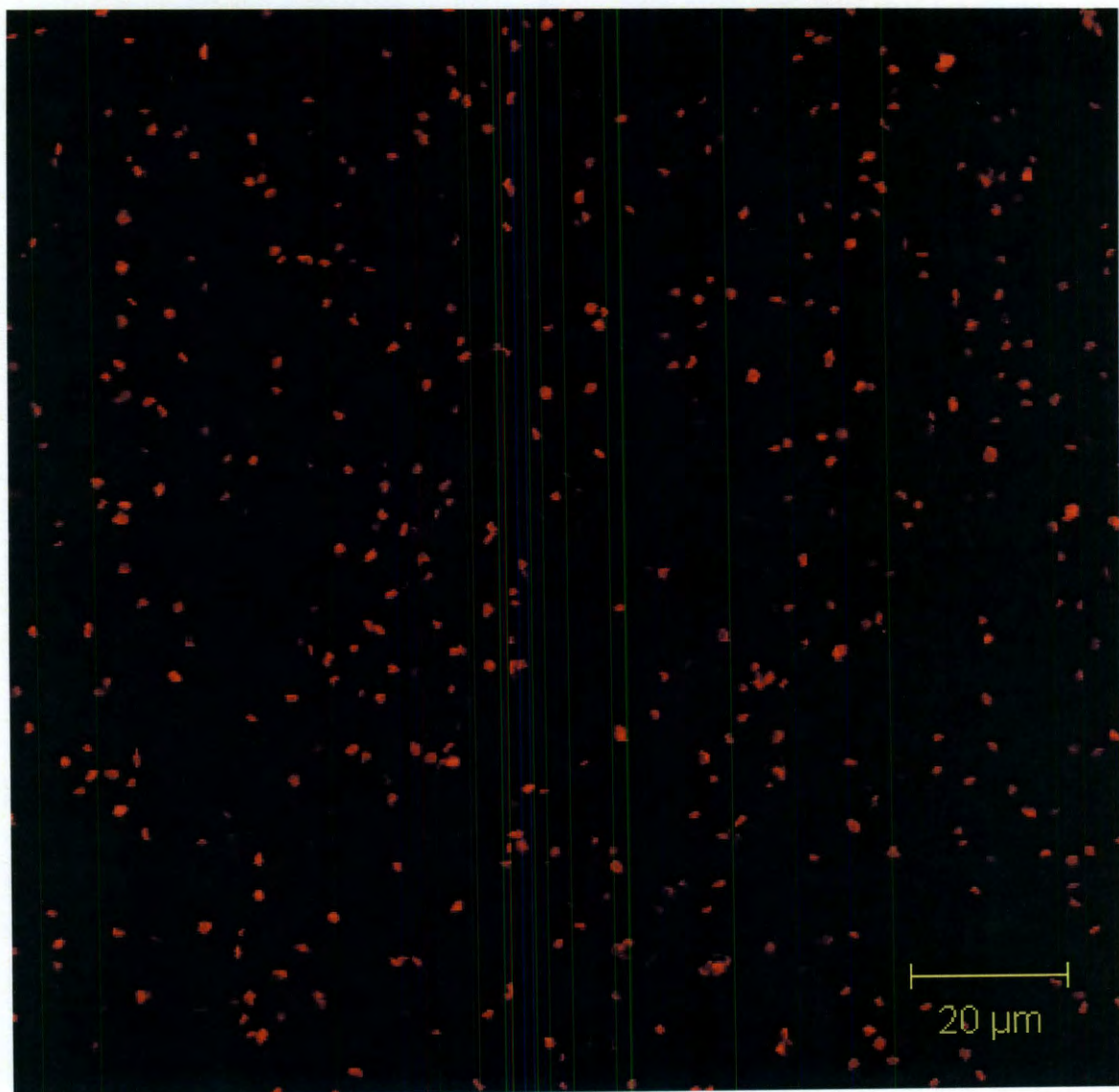
Figure 6-4. Representative fluorescence confocal image of silicon discs loaded with an optically active antibody

6.4.3 Monitoring Release of Antibody-Dye Over Time

When a sample was monitored over time to determine the profile of release of the antibody-dye component from the silicon discs, it appeared that the majority of antibody was released within the first 9 hours. The time-course profile of a representative sample is shown in Figure 6-5. Other samples had similar profiles but on a different fluorescence intensity scale. This example sample has antibody-dye co-loaded with GNTs in huge sized pore silicon discs.
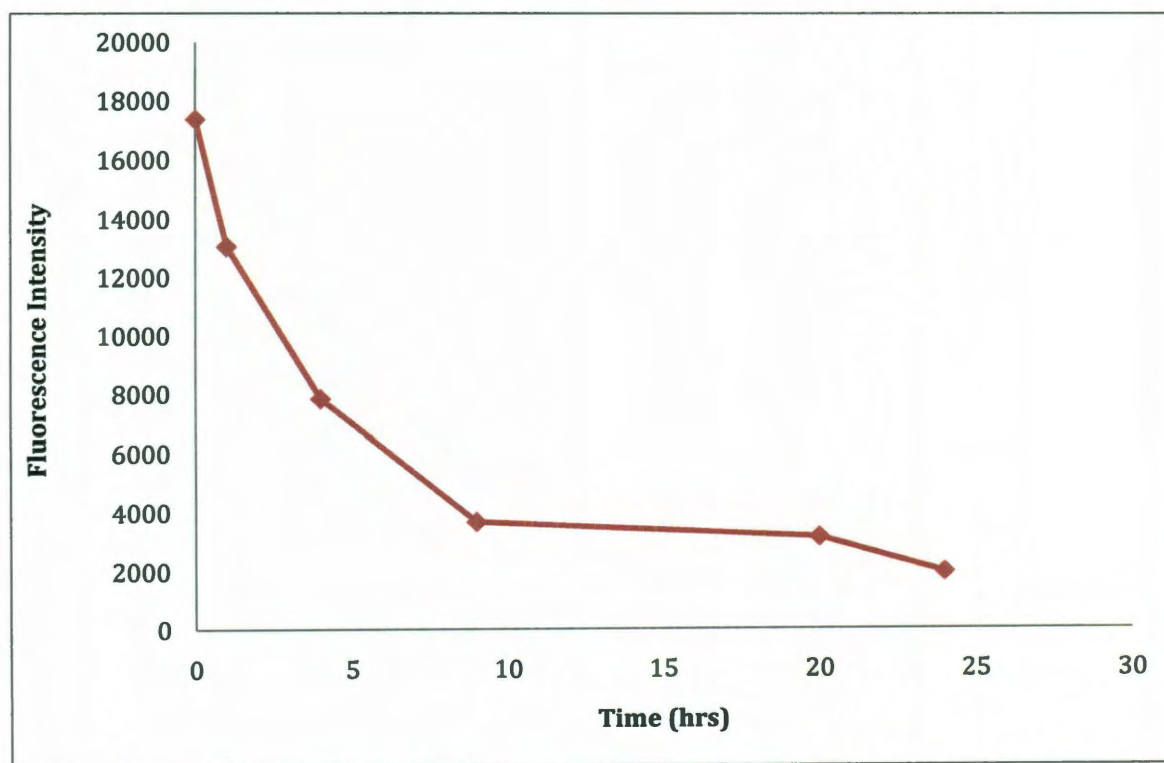
Figure 6-5. Fluorescence intensity of sample over time while exposed to physiologically relevant conditions, indicates release of optically active component of the multimodal imaging agent

6.5 Discussion

These preliminary characterization studies have demonstrated the technical feasibility of combining MRI and optical imaging agents by co-loading in nanoporous silicon discs. The amount of loading was estimated based on the removed supernatant, and loading was confirmed by confocal imaging. It's possible that the amount of loading could be overestimated by measuring the supernatant, but this indirect measurement was chosen because of the likelihood of dye self-quenching while in close proximity within the silicon particle. Additionally, the Gd-CA could cause fluorescence to be quenched. GNTs have a broad absorbance spectrum as measured in the Cary 50 UV-Vis Spectrophotometer, including in the range of the Alexa Fluor 647 dye's excitation and emission. When GNTs were added into the antibody-dye conjugate control and measured in the fluorometer, the fluorescence decreased. Therefore, measuring the loaded silicon disc sample directly has inherent measurement inaccuracies.

Although the fluorescence may have been quenched from either dye-dye interactions or absorbance of the Gd-CAs, the loaded silicon particles were still easily visualized with fluorescence confocal imaging. This result helps confirm the presence of the optical agent within the silicon discs, and confirms that the antibody-dye conjugate remains optically active. As the antibody is released from the disc, it should retain its optical properties as well.

The time-release profile of the antibody indicates that the majority of the optically active component is released within the first 9 hours. Previous results in a rodent tumor model have indicated that due to their unique size and shape, the silicon discs used here accumulate in the tumor tissue following intravenous injection, likely due to the

enhanced permeability and retention (EPR) effect in tumors. The observed time-release profile may allow these silicon discs to serve as a carrier for the targeted antibody-dye conjugate, locally delivering them near the tumor tissue to decrease the non-tumor-specific effects of binding to EGFR in other organ sites. Whole body MRI could be used to locate the tumor and distant metastases, and guide optical probe positioning, and then optical imaging through an inserted probe could be used to obtain molecular-specific information about the tumor. Optical imaging could also be performed intra-operatively to ensure removal of all tumor tissue and also locate metastases for removal.

6.6 Future Experiments

The studies described here have only developed and characterized antibody loading in silicon discs, with and without the presence of Gd-CAs. The next steps required to achieve the potential applications described in the discussion are to first improve the consistency of loading between samples and batches. Altering steps of the loading method may result in more consistent or more efficient loading. The loading process was originally developed for gadolinium-based contrast agents and may need to be altered for an antibody. More sets of samples co-loaded with Magnevist® in small pore sized silicon discs could help determine which loading steps could be altered to improve loading reproducibility.

If loading remains consistent, it will be important to confirm the efficiency of loading in a way other than by measuring the supernatant. One potential technique could be to degrade the silicon discs, dilute the sample so that dye-dye interactions and Gd-CA quenching is minimized, and measure this solution in the fluorometer. Confocal imaging of this sample could confirm that the silicon discs are degraded; degradation may be

achieved by heat or chemical methods. However, the degradation method should not affect the structure of the antibody-dye conjugate in a way that affects fluorescence intensity. Reconstituting the silicon discs in PBS and leaving them in an incubator for a few days should achieve degradation without compromising the chemical integrity of the antibody or dye.

Once the loading amount is confirmed by another method, the multimodal imaging agents could be applied in an in vitro setting to ensure that the targeting ability of the antibody is still functioning as expected. EGFR positive and negative cell lines could be used to demonstrate molecular-specific targeting ability. From discussions with Paolo Decuzzi, it appears that these silicon discs will enter cells through endocytosis in a non-targeted manner. Therefore, to distinguish molecular-specific targeting from random endocytosis, the silicon discs should be exposed to physiologic conditions to release the antibody, and this resulting solution could be incubated with EGFR positive and negative cell lines over ice to prevent endocytosis. The need to first release the antibody from the silicon discs is because the antibody is trapped within the pores and its targeting moiety is not exposed, and therefore will not be able to bind to EGFR molecules on the cell surface. The cells could be imaged using confocal microscopy to confirm molecular specificity.

Finally, the multimodal imaging agent could be intravenously injected into a rodent tumor model to examine the biodistribution of the agent, observe if MRI contrast of the tumor is enhanced, and determine if optical imaging of EGFR in the tumor can be achieved. More time-release studies would be necessary to determine the optimum time

frame to image the animal, but the steps described in this section provide a potential outline for future experiments using the this new multimodal imaging agent.

6.7 Acknowledgements

CHAPTER 7: SUMMARY AND CONCLUSIONS

7.1 Summary of Results

This thesis describes how quantitative optical molecular imaging techniques were developed and evaluated for multiple applications in the field of oncology. First, molecular-specific optical imaging with targeted contrast agents was used to examine biomarker expression near the tissue surface for the clinical application of early detection, using oral squamous cell carcinoma as a relevant example. Next, optical imaging was used to classify lymph nodes from breast cancer patients as either normal or metastatic; this applies to the clinical application of staging and would require an optical probe to be inserted through a needle to achieve imaging of sub-surface tissue. Finally, to address the clinical application of imaging of deeper tissues that may not be immediately accessible to optical imaging, a multimodal imaging agent was developed that is both optically active and enhances contrast in magnetic resonance imaging. The work presented here identifies applications of optical molecular imaging across a broad range of problems in oncology, both as a research tool and to enhance the clinical management of cancer patients.

The second chapter provided background on the problem of oral cancer and acknowledged the limitations of current detection aids, which motivated the targeted imaging studies presented in chapters three and four. Current methods of detection lack specificity due to the high prevalence of confounding lesions in the oral cavity. In chapter three, EGF-Alexa 647, an imaging agent that specifically targets EGFR, was described, validated, and tested in multiple excised human specimens of oral cancer and

dysplasia. In widefield fluorescence images of fresh oral tissue diagnosed as moderate or severe dysplasia, we observed an average 2.3 fold increase in the fluorescence signal in neoplastic tissue as compared to normal tissue. For samples diagnosed as cancer, we observed an average 3.8 fold increase in fluorescence signal.

Chapter four extends the work described in chapter three by examining multiple biomarkers in oral tissue. The addition of imaging metabolic activity with 2-NBDG to imaging EGFR expression provides another clinically relevant marker of neoplasia. Because optical imaging allows separation of signals due to unique spectral properties of the dyes, the relationship of one biomarker to another and how each correlates to the presence of disease can also be investigated. A classification algorithm was developed based on features from fluorescence images from each imaging agent. Including features from both agents in the algorithm resulted in better overall performance and a final AUC of 0.83. While the classification performance is not extremely high, optical molecular imaging may serve as an important research tool to understand the implications of biomarker expression, heterogeneity, and co-localization. This may translate into better understanding of cancer biology and have implications for clinical management of cancer patients or development of targeted therapeutic agents.

Chapter five applied optical molecular imaging to the clinical setting of patient staging. The presence of axillary lymph node metastases is the most important prognostic factor for a patient with breast cancer, and determines appropriate adjuvant therapy after surgery. Accessing lymph nodes with optical imaging would require threading a small diameter optical probe through a needle. Quantitative image analysis resulted in a classification algorithm to distinguish normal lymphoid tissue from

metastatic tissue with an AUC of 0.84. The ability to recognize metastatic nodes in vivo with optical imaging would identify affected nodes for removal, while allowing normal nodes to remain, thus reducing the side effects common in full axillary dissection.

Chapter six described preliminary results from a project that augments the information obtained from optical imaging by combining it with magnetic resonance imaging through the development of a multimodal imaging agent. High efficiency, consistent loading of the antibody-dye conjugate was achieved in small pore size silicon discs co-loaded with Magnevist. This imaging agent could be used for imaging of deep tissue, since MRI is able to achieve full body contrast. After using MRI to identify the location of a tumor, an optical probe could be guided to the appropriate location to obtain high resolution, molecular-specific information. Combining optical imaging with other modalities may extend its usefulness as both a cancer research tool and clinically relevant technique.

7.2 Future Directions

The studies presented in this thesis lay the groundwork for optical molecular imaging in several different settings by presenting proof of concept design and ex vivo experiments with human tissue. The eventual goal of all of these projects, however, is to perform optical molecular imaging in vivo to gain knowledge about an individual patient's neoplasia and more effectively tailor diagnosis and treatment options. This type of personalized medicine may result in better outcomes for individuals affected by cancer by improving early diagnosis, determining extent of tumor spread so ideal surgical resection is achieved, or understanding which subset of patients will respond to a particular therapy.

Some progress has already be made to move this type of research from ex vivo to in vivo, for example, in 2008, Thomas Wang's group at Stanford reported the in vivo use of a targeted optical imaging agent for the detection of dysplasic colonocytes [209]. In this case, a heptapeptide selected through phage display and panning with excised tissue was conjugated to fluorescein and applied topically through the instrument channel in a standard colonoscope. A few lessons can be learned from this example. First, fluorescein was used as the dye because it is already FDA approved for in vivo use, which likely aided the approval by the Stanford IRB. Unfortunately, fluorescein's excitation and emission occur within the same wavelengths as in vivo autofluorescence. Another dye that is FDA approved for in vivo use, indocyanine green (ICG), has spectral features in the near infrared, which are less likely to overlap with tissue autofluorescence. However, the lack of a multitude of approved optical dyes currently limits the in vivo use of multiplexed optical imaging, and is something that will need to be addressed for optical molecular imaging to reach its full clinical potential. This will require in vivo toxicity studies in animals and humans before new dyes can be approved.

An aspect of the heptapeptide study that is encouraging for future extension of the research presented in this thesis is the effective transition of the targeting ability of the imaging agent from ex vivo, resected colonic tissue to in vivo, intact colons. The peptide was selected for its high affinity to dysplastic colon tissue during sequential panning studies, and the same peptide was able to effectively target dysplastic colonocytes in vivo as well. The research presented here is based on ex vivo studies, with the hope that ex vivo results will translate to in vivo situations, and this study provides one encouraging example that ex vivo tissue is a good model for future in vivo work.

2-NBDG, one of the imaging agents used in the studies in resected oral mucosa, provides a way to monitor metabolic activity of tissue. While this agent still shows contrast in freshly resected tissue, using it in vivo may only enhance its ability to detect metabolic activity due to neoplasia. In vivo, the tissue will still be connected to vasculature that will supply nutrients and keep the tissue viable, but after the tissue has been removed, it lacks support and the cells will quickly die. The EGFR-targeted imaging agents may also result in improved optical contrast in vivo, where active cells will internalize the EGF receptors along with the imaging agent and therefore continually accumulate optical signal within the cytoplasm. In vivo tests will of course have to be conducted to determine if this is the case, but it seems unlikely that in vivo tissue would have decreased optical contrast from ex vivo tissue.

A very recent study has implications for the research presented in this thesis related to staging in breast cancer. In February of this year, a phase 3 noninferiority trial was published in the Journal of the American Medical Association comparing overall and disease-free survival in breast cancer patients with sentinel lymph node metastases who did or did not undergo full axillary dissection [210]. The nearly 1000 patients included in this study had breast tumors less than five centimeters in diameter that were removed with lumpectomy that achieved clear margins. The patients all had positive sentinel lymph nodes (between one and three positive SLNs), with "micrometastases" less than two millimeters in diameter. All patients also received radiation therapy. The study observed no significant difference in five-year disease-free or overall survival, indicating that full axillary dissection may not be required for patients who have small tumors, achieve good surgical results, and have only micrometastases in the sentinel node. Due

to the side effects associated with full axillary dissection, clear guidelines of which patients may or may not benefit from additional removal of lymph nodes will help prevent unnecessary adverse effects while still achieving maximal survival benefits.

After the pilot study of using HRFM with proflavine contrast demonstrated the technical feasibility of detecting lymph node metastases with optical imaging techniques, planning for future studies with HRFM centered around the goal of determining the size limit of metastases that could be detected. However, in light of this recently published study, improving the size limit of nodal metastases detection may not be the best direction for the project. The diameter of the optical probe used in the pilot study was 750 micrometers, which is below the two millimeter cut-off size used in the noninferiority study. Instead, HRFM could potentially be used to measure metastasis size to see if nodal metastases are above or below two millimeters in diameter to determine if full axillary dissection is necessary. Staging of axilla could be performed preoperatively through a needle as an adjunct to fine needle aspiration, or intraoperatively.

The studies described in this thesis demonstrate the potential benefit of optical molecular imaging in a variety of clinical settings. While future in vivo toxicity tests will be required to move these imaging agents from ex vivo tissue to patients, these studies help validate targeting ability of the imaging agents and suggest roles for optical molecular imaging as both a research tool and in clinical management of cancer patients. Translation of these imaging agents and techniques to the clinic may result in improved survival and personalized patient care.

REFERENCES

[1]   WHO Cancer, Available at http://www.who.int/cancer/en/, (2008).

[2]   Parkin DM, Bray F, Ferlay J, and Pisani P (2005). Global cancer statistics, 2002. *CA Cancer J Clin* **55**, 74-108.

[3]   Moore SR, Johnson NW, Pierce AM, and Wilson DF (2000). The epidemiology of mouth cancer: a review of global incidence. *Oral Dis* **6**, 65-74.

[4]   Altekruse SF, Kosary CL, Krapcho M, Neyman N, Aminou R, Waldron W, Ruhl J, Howlader N, Tatalovich Z, Cho H, Mariotto A, Eisner MP, Lewis DR, Cronin K, Chen HS, Feuer EJ, Stinchcomb DG, Edwards BK (eds). SEER Cancer Statistics Review, 1975-2007, National Cancer Institute. Bethesda, MD, http://seer.cancer.gov/csr/1975_2007/, based on November 2009 SEER data submission, posted to the SEER web site, 2010.

[5]   Mehrotra R, Singh M, Kumar D, Pandey AN, Gupta RK, and Sinha US (2003). Age specific incidence rate and pathological spectrum of oral cancer in Allahabad. *Indian J Med Sci* **57**, 400-404.

[6]   Rumboldt Z, Day TA, and Michel M (2006). Imaging of oral cavity cancer. *Oral Oncol* **42**, 854-865.

[7]   Tsantoulis PK, Kastrinakis NG, Tourvas AD, Laskaris G, and Gorgoulis VG (2007). Advances in the biology of oral cancer. *Oral Oncol* **43**, 523-534.

[8]   National Cancer Institute Oral Cavity and Pharynx Cancer: Trends in SEER incidence and U.S. mortality using the joinpoint regression program, 1973-1998, Available at http://seer.cancer.gov/csr/1973_1998/oralcav.pdf.

[9]   Black RJ, Bray F, Ferlay J, and Parkin DM (1997). Cancer incidence and mortality in the European Union: cancer registry data and estimates of national incidence for 1990. *Eur J Cancer* **33**, 1075-1107.

[10]   Sciubba JJ (2001). Oral cancer. The importance of early diagnosis and treatment. *Am J Clin Dermatol* **2**, 239-251.

[11]   Lingen MW, Kalmar JR, Karrison T, and Speight PM (2008). Critical evaluation of diagnostic aids for the detection of oral cancer. *Oral Oncol* **44**, 10-22.

[12]   Michael H. Ross WP (2006) *Histology: A text and atlas* (Lippincott Williams & Wilkins, Baltimore).

[13]   Waldron CA, and Shafer WG (1975). Leukoplakia revisited. A clinicopathologic study 3256 oral leukoplakias. *Cancer* **36**, 1386-1392.

[14]   Alan Stevens JSL, Barbara Young (2002) *Wheater's Basic Histopathology: A colour atlas and text* (Churchill Livingstone, Edinburgh).

[15]   Rubin P (2001) Clinical Oncology: a multidisciplinary approach for physicians and students (W.B. Saunders Company, Philadelphia).

[16]   Shiboski CH, Shiboski SC, and Silverman S, Jr. (2000). Trends in oral cancer rates in the United States, 1973-1996. Community Dent Oral Epidemiol **28**, 249-256.

[17]   Downer MC, Moles DR, Palmer S, and Speight PM (2004). A systematic review of test performance in screening for oral cancer and precancer. Oral Oncol **40**, 264-273.

[18]   Warnakulasuriya S, and Pindborg JJ (1990). Reliability of oral precancer screening by primary health care workers in Sri Lanka. Community Dent Health **7**, 73-79.

[19]   Mehta FS, Gupta PC, Bhonsle RB, Murti PR, Daftary DK, and Pindborg JJ (1986). Detection of oral cancer using basic health workers in an area of high oral cancer incidence in India. Cancer Detect Prev **9**, 219-225.

[20]   Ikeda N, Downer MC, Ishii T, Fukano H, Nagao T, and Inoue K (1995). Annual screening for oral cancer and precancer by invitation to 60-year-old residents of a city in Japan. *Community Dent Health* **12**, 133-137.

[21]   Mathew B, Sankaranarayanan R, Sunilkumar KB, Kuruvila B, Pisani P, and Nair MK (1997). Reproducibility and validity of oral visual inspection by trained health workers in the detection of oral precancer and cancer. *Br J Cancer* **76**, 390-394.

[22]   Shugars DC, and Patton LL (1997). Detecting, diagnosing, and preventing oral cancer. *Nurse Pract* **22**, 105, 109-110, 113-105 passim.

[23]   Silverman S, Jr. (1988). Early diagnosis of oral cancer. *Cancer* **62**, 1796-1799.

[24]   Downer MC, Evans AW, Hughes Hallet CM, Jullien JA, Speight PM, and Zakrzewska JM (1995). Evaluation of screening for oral cancer and precancer in a company headquarters. *Community Dent Oral Epidemiol* **23**, 84-88.

[25]   Jullien JA, Downer MC, Zakrzewska JM, and Speight PM (1995). Evaluation of a screening test for the early detection of oral cancer and precancer. *Community Dent Health* **12**, 3-7.

[26]   Bouquot JE (1986). Common oral lesions found during a mass screening examination. *J Am Dent Assoc* **112**, 50-57.

[27]   Burzynski NJ, Firriolo FJ, Butters JM, and Sorrell CL (1997). Evaluation of oral cancer screening. *J Cancer Educ* **12**, 95-99.

[28]   Malaovalla AM, Silverman S, Mani NJ, Bilimoria KF, and Smith LW (1976). Oral cancer in 57,518 industrial workers of Gujarat, India: a prevalence and followup study. *Cancer* **37**, 1882-1886.

[29]   van der Meij EH, Mast H, and van der Waal I (2007). The possible premalignant character of oral lichen planus and oral lichenoid lesions: a prospective five-year follow-up study of 192 patients. *Oral Oncol* **43**, 742-748.

[30]   Bagan JV, and Scully C (2008). Recent advances in Oral Oncology 2007: epidemiology, aetiopathogenesis, diagnosis and prognostication. *Oral Oncol* **44**, 103-108.

[31]   Thomson PJ (2002). Field change and oral cancer: new evidence for widespread carcinogenesis? *Int J Oral Maxillofac Surg* **31**, 262-266.

[32]   Poh CF, Ng S, Berean KW, Williams PM, Rosin MP, and Zhang L (2008). Biopsy and histopathologic diagnosis of oral premalignant and malignant lesions. *J Can Dent Assoc* **74**, 283-288.

[33]   Brouha XD, Tromp DM, Koole R, Hordijk GJ, Winnubst JA, and de Leeuw JR (2007). Professional delay in head and neck cancer patients: analysis of the diagnostic pathway. *Oral Oncol* **43**, 551-556.

[34]   Mehrotra R, Gupta A, Singh M, and Ibrahim R (2006). Application of cytology and molecular biology in diagnosing premalignant or malignant oral lesions. *Mol Cancer* **5**, 11.

[35]   Eisen D, and Frist S (2005). The relevance of the high positive predictive value of the oral brush biopsy. *Oral Oncol* **41**, 753-755; author reply 756.

[36]   Eisen D (2002). Brush biopsy 'saves lives'. *J Am Dent Assoc* **133**, 688, 690, 692.

[37]   Svirsky JA, Burns JC, Page DG, and Abbey LM (2001). Computer-assisted analysis of the oral brush biopsy. *Compend Contin Educ Dent* **22**, 99-102, 104, 106; quiz 108.

[38]   Navone R, Burlo P, Pich A, Pentenero M, Broccoletti R, Marsico A, and Gandolfo S (2007). The impact of liquid-based oral cytology on the diagnosis of oral squamous dysplasia and carcinoma. *Cytopathology* **18**, 356-360.

[39]   Mehrotra R, Hullmann M, Smeets R, Reichert TE, and Driemel O (2009). Oral cytology revisited. *Journal of oral pathology & medicine : official publication of the International Association of Oral Pathologists and the American Academy of Oral Pathology* **38**, 161-166.

[40]   Gupta A, Singh M, Ibrahim R, and Mehrotra R (2007). Utility of toluidine blue staining and brush biopsy in precancerous and cancerous oral lesions. *Acta Cytol* **51**, 788-794.

[41]   Barrellier P, Babin E, Louis MY, and Meunier-Guttin A (1993). [The use of toluidine blue in the diagnosis of neoplastic lesions of the oral cavity]. *Rev Stomatol Chir Maxillofac* **94**, 51-54.

[42]   Mashberg A (1983). Final evaluation of tolonium chloride rinse for screening of high-risk patients with asymptomatic squamous carcinoma. *J Am Dent Assoc* **106**, 319-323.

[43]   Martin IC, Kerawala CJ, and Reed M (1998). The application of toluidine blue as a diagnostic adjunct in the detection of epithelial dysplasia. *Oral Surg Oral Med Oral Pathol Oral Radiol Endod* **85**, 444-446.

[44]   Onofre MA, Sposto MR, and Navarro CM (2001). Reliability of toluidine blue application in the detection of oral epithelial dysplasia and in situ and invasive squamous cell carcinomas. *Oral Surg Oral Med Oral Pathol Oral Radiol Endod* **91**, 535-540.

[45]   Warnakulasuriya KA, and Johnson NW (1996). Sensitivity and specificity of OraScan (R) toluidine blue mouthrinse in the detection of oral cancer and precancer. *J Oral Pathol Med* **25**, 97-103.

[46]   Huber MA, Bsoul SA, and Terezhalmy GT (2004). Acetic acid wash and chemiluminescent illumination as an adjunct to conventional oral soft tissue examination for the detection of dysplasia: a pilot study. *Quintessence Int* **35**, 378-384.

[47]   Ram S, and Siar CH (2005). Chemiluminescence as a diagnostic aid in the detection of oral cancer and potentially malignant epithelial lesions. *Int J Oral Maxillofac Surg* **34**, 521-527.

[48]   Epstein JB, Gorsky M, Lonky S, Silverman S, Jr., Epstein JD, and Bride M (2006). The efficacy of oral lumenoscopy (ViziLite) in visualizing oral mucosal lesions. *Spec Care Dentist* **26**, 171-174.

[49]   Kerr AR, Sirois DA, and Epstein JB (2006). Clinical evaluation of chemiluminescent lighting: an adjunct for oral mucosal examinations. *J Clin Dent* **17**, 59-63.

[50]   Farah CS, and McCullough MJ (2007). A pilot case control study on the efficacy of acetic acid wash and chemiluminescent illumination (ViziLite) in the visualisation of oral mucosal white lesions. *Oral Oncol* **43**, 820-824.

[51]   Mehrotra R, Singh M, Thomas S, Nair P, Pandya S, Nigam NS, and Shukla P (2010). A cross-sectional study evaluating chemiluminescence and

autofluorescence in the detection of clinically innocuous precancerous and cancerous oral lesions. *Journal of the American Dental Association* **141**, 151-156.

[52]   Oh ES, and Laskin DM (2007). Efficacy of the ViziLite system in the identification of oral lesions. *Journal of oral and maxillofacial surgery : official journal of the American Association of Oral and Maxillofacial Surgeons* **65**, 424-426.

[53]   Muller MG, Valdez TA, Georgakoudi I, Backman V, Fuentes C, Kabani S, Laver N, Wang Z, Boone CW, Dasari RR, *et al.* (2003). Spectroscopic detection and evaluation of morphologic and biochemical changes in early human oral carcinoma. *Cancer* **97**, 1681-1692.

[54]   Ramanujam N (2000). Fluorescence spectroscopy of neoplastic and non-neoplastic tissues. *Neoplasia* **2**, 89-117.

[55]   Wagnieres GA, Star WM, and Wilson BC (1998). In vivo fluorescence spectroscopy and imaging for oncological applications. *Photochem Photobiol* **68**, 603-632.

[56]   De Veld DC, Witjes MJ, Sterenborg HJ, and Roodenburg JL (2005). The status of in vivo autofluorescence spectroscopy and imaging for oral oncology. *Oral Oncol* **41**, 117-131.

[57]   Poh CF, Zhang L, Anderson DW, Durham JS, Williams PM, Priddy RW, Berean KW, Ng S, Tseng OL, MacAulay C, *et al.* (2006). Fluorescence visualization detection of field alterations in tumor margins of oral cancer patients. *Clin Cancer Res* **12**, 6716-6722.

[58]   Lane PM, Gilhuly T, Whitehead P, Zeng H, Poh CF, Ng S, Williams PM, Zhang L, Rosin MP, and MacAulay CE (2006). Simple device for the direct visualization of oral-cavity tissue fluorescence. *J Biomed Opt* **11**, 024006.

[59]   Poh CF, Ng SP, Williams PM, Zhang L, Laronde DM, Lane P, Macaulay C, and Rosin MP (2007). Direct fluorescence visualization of clinically occult high-risk oral premalignant disease using a simple hand-held device. *Head Neck* **29**, 71-76.

[60]   Awan KH, Morgan PR, and Warnakulasuriya S (2011). Evaluation of an autofluorescence based imaging system (VELscope) in the detection of oral potentially malignant disorders and benign keratoses. *Oral oncology*.

[61]   Hsu ER, Gillenwater AM, Hasan MQ, Williams MD, El-Naggar AK, and Richards-Kortum RR (2006). Real-time detection of epidermal growth factor receptor expression in fresh oral cavity biopsies using a molecular-specific contrast agent. *Int J Cancer* **118**, 3062-3071.

[62]   Heintzelman DL, Utzinger U, Fuchs H, Zuluaga A, Gossage K, Gillenwater AM, Jacob R, Kemp B, and Richards-Kortum RR (2000). Optimal excitation wavelengths for in vivo detection of oral neoplasia using fluorescence spectroscopy. *Photochem Photobiol* **72**, 103-113.

[63]   Carpenter G (1987). Receptors for epidermal growth factor and other polypeptide mitogens. *Annu Rev Biochem* **56**, 881-914.

[64]   Santini J, Formento JL, Francoual M, Milano G, Schneider M, Dassonville O, and Demard F (1991). Characterization, quantification, and potential clinical value of the epidermal growth factor receptor in head and neck squamous cell carcinomas. *Head Neck* **13**, 132-139.

[65]   Christensen ME, Engbaek F, Therkildsen MH, Bretlau P, and Nexo E (1995). A sensitive enzyme-linked immunosorbent assay used for quantitation of epidermal growth factor receptor protein in head and neck carcinomas: evaluation, interpretations and limitations. *Br J Cancer* **72**, 1487-1493.

[66]   Ang KK, Berkey BA, Tu X, Zhang HZ, Katz R, Hammond EH, Fu KK, and Milas L (2002). Impact of epidermal growth factor receptor expression on survival and pattern of relapse in patients with advanced head and neck carcinoma. *Cancer Res* **62**, 7350-7356.

[67]   Ishitoya J, Toriyama M, Oguchi N, Kitamura K, Ohshima M, Asano K, and Yamamoto T (1989). Gene amplification and overexpression of EGF receptor in squamous cell carcinomas of the head and neck. *Br J Cancer* **59**, 559-562.

[68]   Kawamoto T, Takahashi K, Nishi M, Kimura T, Matsumura T, and Taniguchi S (1991). Quantitative assay of epidermal growth factor receptor in human squamous cell carcinomas of the oral region by an avidin-biotin method. *Jpn J Cancer Res* **82**, 403-410.

[69]   Shin DM, Ro JY, Hong WK, and Hittelman WN (1994). Dysregulation of epidermal growth factor receptor expression in premalignant lesions during head and neck tumorigenesis. *Cancer Res* **54**, 3153-3159.

[70]   Hanahan D, and Weinberg RA (2000). The hallmarks of cancer. *Cell* **100**, 57-70.

[71]   Ke S, Wen X, Gurfinkel M, Charnsangavej C, Wallace S, Sevick-Muraca EM, and Li C (2003). Near-infrared optical imaging of epidermal growth factor receptor in breast cancer xenografts. *Cancer Res* **63**, 7870-7875.

[72]   Adams KE, Ke S, Kwon S, Liang F, Fan Z, Lu Y, Hirschi K, Mawad ME, Barry MA, and Sevick-Muraca EM (2007). Comparison of visible and near-infrared wavelength-excitable fluorescent dyes for molecular imaging of cancer. *J Biomed Opt* **12**, 024017.

[73] Rosenthal EL, Kulbersh BD, King T, Chaudhuri TR, and Zinn KR (2007). Use of fluorescent labeled anti-epidermal growth factor receptor antibody to image head and neck squamous cell carcinoma xenografts. *Mol Cancer Ther* **6**, 1230-1238.

[74] Carlson AL, Gillenwater AM, Williams MD, El-Naggar AK, and Richards-Kortum RR (2007). Confocal microscopy and molecular-specific optical contrast agents for the detection of oral neoplasia. *Technol Cancer Res Treat* **6**, 361-374.

[75] Hsu ER, Anslyn EV, Dharmawardhane S, Alizadeh-Naderi R, Aaron JS, Sokolov KV, El-Naggar AK, Gillenwater AM, and Richards-Kortum RR (2004). A far-red fluorescent contrast agent to image epidermal growth factor receptor expression. *Photochem Photobiol* **79**, 272-279.

[76] Hsu ER, Gillenwater AM, and Richards-Kortum RR (2005). Detection of the molecular changes associated with oral cancer using a molecular-specific fluorescent contrast agent and single-wavelength spectroscopy. *Appl Spectrosc* **59**, 1166-1173.

[77] Yoshioka K, Takahashi H, Homma T, Saito M, Oh KB, Nemoto Y, and Matsuoka H (1996). A novel fluorescent derivative of glucose applicable to the assessment of glucose uptake activity of Escherichia coli. *Biochim Biophys Acta* **1289**, 5-9.

[78] Yoshioka K, Oh KB, Saito M, Nemoto Y, and Matsuoka H (1996). Evaluation of 2-[N-(7-nitrobenz-2-oxa-1,3-diazol-4-yl)amino]-2-deoxy-D-glucose, a new fluorescent derivative of glucose, for viability assessment of yeast Candida albicans. *Appl Microbiol Biotechnol* **46**, 400-404.

[79] O'Neil RG, Wu L, and Mullani N (2005). Uptake of a fluorescent deoxyglucose analog (2-NBDG) in tumor cells. *Mol Imaging Biol* **7**, 388-392.

[80] Ide T, Nakane M, and Ando T (1975). Recovery of a DNA-protein complex in cultured mammalian cells from damage caused by 4-nitroquinoline 1-oxide. *Cancer Res* **35**, 3146-3153.

[81] Polglase AL, McLaren WJ, Skinner SA, Kiesslich R, Neurath MF, and Delaney PM (2005). A fluorescence confocal endomicroscope for in vivo microscopy of the upper- and the lower-GI tract. *Gastrointest Endosc* **62**, 686-695.

[82] Muldoon TJ, Thekkek N, Roblyer D, Maru D, Harpaz N, Potack J, Anandasabapathy S, and Richards-Kortum R (2010). Evaluation of quantitative image analysis criteria for the high-resolution microendoscopic detection of neoplasia in Barrett's esophagus. *Journal of biomedical optics* **15**, 026027.

[83] Roblyer D, Richards-Kortum R, Sokolov K, El-Naggar AK, Williams MD, Kurachi C, and Gillenwater AM (2008). Multispectral optical imaging device for in vivo detection of oral neoplasia. *J Biomed Opt* **13**, 024019.

[84]   Muldoon TJ, Pierce MC, Nida DL, Williams MD, Gillenwater A, and Richards-Kortum R (2007). Subcellular-resolution molecular imaging within living tissue by fiber microendoscopy. *Opt Express* **15**, 16413-16423.

[85]   Rosbach KJ, Shin D, Muldoon TJ, Quraishi MA, Middleton LP, Hunt KK, Meric-Bernstam F, Yu TK, Richards-Kortum RR, and Yang W (2010). High-resolution fiber optic microscopy with fluorescent contrast enhancement for the identification of axillary lymph node metastases in breast cancer: a pilot study. *Biomedical optics express* **1**, 911-922.

[86]   Muldoon TJ, Anandasabapathy S, Maru D, and Richards-Kortum R (2008). High-resolution imaging in Barrett's esophagus: a novel, low-cost endoscopic microscope. *Gastrointest Endosc* **68**, 737-744.

[87]   Nitin N, Rosbach KJ, El-Naggar A, Williams M, Gillenwater A, and Richards-Kortum RR (2009). Optical molecular imaging of epidermal growth factor receptor expression to improve detection of oral neoplasia. *Neoplasia* **11**, 542-551.

[88]   Blasberg RG, and Tjuvajev JG (2003). Molecular-genetic imaging: current and future perspectives. *J Clin Invest* **111**, 1620-1629.

[89]   Gelovani Tjuvajev J, and Blasberg RG (2003). In vivo imaging of molecular-genetic targets for cancer therapy. *Cancer Cell* **3**, 327-332.

[90]   Massoud TF, and Gambhir SS (2003). Molecular imaging in living subjects: seeing fundamental biological processes in a new light. *Genes Dev* **17**, 545-580.

[91]   Massoud TF, and Gambhir SS (2007). Integrating noninvasive molecular imaging into molecular medicine: an evolving paradigm. *Trends Mol Med* **13**, 183-191.

[92]   Pomper MG (2005). Translational molecular imaging for cancer. *Cancer Imaging* **5 Spec No A**, S16-26.

[93]   Sokolov K, Aaron J, Hsu B, Nida D, Gillenwater A, Follen M, MacAulay C, Adler-Storthz K, Korgel B, Descour M, *et al.* (2003). Optical systems for in vivo molecular imaging of cancer. *Technol Cancer Res Treat* **2**, 491-504.

[94]   Weissleder R (2006). Molecular imaging in cancer. *Science* **312**, 1168-1171.

[95]   Bankfalvi A, and Piffko J (2000). Prognostic and predictive factors in oral cancer: the role of the invasive tumour front. *J Oral Pathol Med* **29**, 291-298.

[96]   Bettendorf O, Piffko J, and Bankfalvi A (2004). Prognostic and predictive factors in oral squamous cell cancer: important tools for planning individual therapy? *Oral Oncol* **40**, 110-119.

[97]   Chimenos-Kustner E, Font-Costa I, and Lopez-Lopez J (2004). Oral cancer risk and molecular markers. *Med Oral Patol Oral Cir Bucal* **9**, 381-384; 377-380.

[98]   Macluskey M, and Ogden GR (2000). An overview of the prevention of oral cancer and diagnostic markers of malignant change: 2. Markers of value in tumour diagnosis. *Dent Update* **27**, 148-152.

[99]   Schliephake H (2003). Prognostic relevance of molecular markers of oral cancer--a review. *Int J Oral Maxillofac Surg* **32**, 233-245.

[100]   Banerjee AG, Bhattacharyya I, and Vishwanatha JK (2005). Identification of genes and molecular pathways involved in the progression of premalignant oral epithelia. *Mol Cancer Ther* **4**, 865-875.

[101]   Braakhuis BJ, Leemans CR, and Brakenhoff RH (2004). A genetic progression model of oral cancer: current evidence and clinical implications. *J Oral Pathol Med* **33**, 317-322.

[102]   Califano J, Ahrendt SA, Meininger G, Westra WH, Koch WM, and Sidransky D (1996). Detection of telomerase activity in oral rinses from head and neck squamous cell carcinoma patients. *Cancer Res* **56**, 5720-5722.

[103]   Ha PK, Pilkington TA, Westra WH, Sciubba J, Sidransky D, and Califano JA (2002). Progression of microsatellite instability from premalignant lesions to tumors of the head and neck. *Int J Cancer* **102**, 615-617.

[104]   Lippman SM, Sudbo J, and Hong WK (2005). Oral cancer prevention and the evolution of molecular-targeted drug development. *J Clin Oncol* **23**, 346-356.

[105]   Mankoff DA, Shields AF, and Krohn KA (2005). PET imaging of cellular proliferation. *Radiol Clin North Am* **43**, 153-167.

[106]   Muzi M, Mankoff DA, Grierson JR, Wells JM, Vesselle H, and Krohn KA (2005). Kinetic modeling of 3'-deoxy-3'-fluorothymidine in somatic tumors: mathematical studies. *J Nucl Med* **46**, 371-380.

[107]   Stokkel MP, ten Broek FW, and van Rijk PP (1998). The role of FDG PET in the clinical management of head and neck cancer. *Oral Oncol* **34**, 466-471.

[108]   Onizawa K, Saginoya H, Furuya Y, Yoshida H, and Fukuda H (1999). Usefulness of fluorescence photography for diagnosis of oral cancer. *Int J Oral Maxillofac Surg* **28**, 206-210.

[109]   Onizawa K, Okamura N, Saginoya H, and Yoshida H (2003). Characterization of autofluorescence in oral squamous cell carcinoma. *Oral Oncol* **39**, 150-156.

[110]   Betz CS, Stepp H, Janda P, Arbogast S, Grevers G, Baumgartner R, and Leunig A (2002). A comparative study of normal inspection, autofluorescence and 5-

ALA-induced PPIX fluorescence for oral cancer diagnosis. *Int J Cancer* **97**, 245-252.

[111] Leunig A, Betz CS, Mehlmann M, Stepp H, Arbogast S, Grevers G, and Baumgartner R (2000). Detection of squamous cell carcinoma of the oral cavity by imaging 5-aminolevulinic acid-induced protoporphyrin IX fluorescence. *Laryngoscope* **110**, 78-83.

[112] McLoone N, Donnelly RF, Walsh M, Dolan OM, McLoone S, McKenna K, and McCarron PA (2008). Aminolaevulinic acid diffusion characteristics in 'in vitro' normal human skin and actinic keratosis: implications for topical photodynamic therapy. *Photodermatol Photoimmunol Photomed* **24**, 183-190.

[113] Frangioni JV (2006). Translating in vivo diagnostics into clinical reality. *Nat Biotechnol* **24**, 909-913.

[114] Simon LL, and Rubinstein D (2006). Imaging of oral cancer. *Otolaryngol Clin North Am* **39**, 307-317, vi.

[115] Wilder-Smith P, Krasieva T, Jung WG, Zhang J, Chen Z, Osann K, and Tromberg B (2005). Noninvasive imaging of oral premalignancy and malignancy. *J Biomed Opt* **10**, 051601.

[116] Ekberg T, Nestor M, Engstrom M, Nordgren H, Wester K, Carlsson J, and Anniko M (2005). Expression of EGFR, HER2, HER3, and HER4 in metastatic squamous cell carcinomas of the oral cavity and base of tongue. *Int J Oncol* **26**, 1177-1185.

[117] Kuttan NA, and Bhakthan NM (1997). Epidermal growth factor receptor (EGFR) in oral squamous cell carcinomas: overexpression, localization and therapeutic implications. *Indian J Dent Res* **8**, 9-18.

[118] Richter P, Bohmer FD, Hindermann W, Borsi L, Hyckel P, Schleier P, Katenkamp D, Kosmehl H, and Berndt A (2005). Analysis of activated EGFR signalling pathways and their relation to laminin-5 gamma2 chain expression in oral squamous cell carcinoma (OSCC). *Histochem Cell Biol* **124**, 151-160.

[119] Todd R, and Wong DT (1999). Epidermal growth factor receptor (EGFR) biology and human oral cancer. *Histol Histopathol* **14**, 491-500.

[120] Chen IH, Chang JT, Liao CT, Wang HM, Hsieh LL, and Cheng AJ (2003). Prognostic significance of EGFR and Her-2 in oral cavity cancer in betel quid prevalent area cancer prognosis. *Br J Cancer* **89**, 681-686.

[121] Wahl MI, and Carpenter G (1987). Role of growth factors and their receptors in the control of normal cell proliferation and cancer. *Clin Physiol Biochem* **5**, 130-139.

[122]   Perez-Soler R, Donato NJ, Shin DM, Rosenblum MG, Zhang HZ, Tornos C, Brewer H, Chan JC, Lee JS, Hong WK, *et al.* (1994). Tumor epidermal growth factor receptor studies in patients with non-small-cell lung cancer or head and neck cancer treated with monoclonal antibody RG 83852. *J Clin Oncol* **12**, 730-739.

[123]   Scambia G, Panici PB, Battaglia F, Ferrandina G, Almadori G, Paludetti G, Maurizi M, and Mancuso S (1991). Receptors for epidermal growth factor and steroid hormones in primary laryngeal tumors. *Cancer* **67**, 1347-1351.

[124]   Sokolov K, Galvan J, Myakov A, Lacy A, Lotan R, and Richards-Kortum R (2002). Realistic three-dimensional epithelial tissue phantoms for biomedical optics. *J Biomed Opt* **7**, 148-156.

[125]   De Rosa FS, Marchetti JM, Thomazini JA, Tedesco AC, and Bentley MV (2000). A vehicle for photodynamic therapy of skin cancer: influence of dimethylsulphoxide on 5-aminolevulinic acid in vitro cutaneous permeation and in vivo protoporphyrin IX accumulation determined by confocal microscopy. *J Control Release* **65**, 359-366.

[126]   Kurihara-Bergstrom T, Flynn GL, and Higuchi WI (1987). Physicochemical study of percutaneous absorption enhancement by dimethyl sulfoxide: dimethyl sulfoxide mediation of vidarabine (ara-A) permeation of hairless mouse skin. *J Invest Dermatol* **89**, 274-280.

[127]   Xu DH, Zhang Q, Feng X, Xu X, and Liang WQ (2007). Synergistic effects of ethosomes and chemical enhancers on enhancement of naloxone permeation through human skin. *Pharmazie* **62**, 316-318.

[128]   Pavlova I, Williams M, El-Naggar A, Richards-Kortum R, and Gillenwater A (2008). Understanding the biological basis of autofluorescence imaging for oral cancer detection: high-resolution fluorescence microscopy in viable tissue. *Clin Cancer Res* **14**, 2396-2404.

[129]   Lee SH, Lee S, Youn YS, Na DH, Chae SY, Byun Y, and Lee KC (2005). Synthesis, characterization, and pharmacokinetic studies of PEGylated glucagon-like peptide-1. *Bioconjug Chem* **16**, 377-382.

[130]   Powell MF, Grey H, Gaeta F, Sette A, and Colon S (1992). Peptide stability in drug development: a comparison of peptide reactivity in different biological media. *J Pharm Sci* **81**, 731-735.

[131]   Li K, Thomasson D, Ketai L, Contag C, Pomper M, Wright M, and Bray M (2005). Potential applications of conventional and molecular imaging to biodefense research. *Clin Infect Dis* **40**, 1471-1480.

[132]   Nakamura T, Takasugi H, Aizawa T, Yoshida M, Mizuguchi M, Mori Y, Shinoda H, Hayakawa Y, and Kawano K (2005). Peptide mimics of epidermal growth factor (EGF) with antagonistic activity. *J Biotechnol* **116**, 211-219.

[133]   Lippman SM, and Hong WK (2001). Molecular markers of the risk of oral cancer. *N Engl J Med* **344**, 1323-1326.

[134]   Shah NG, Trivedi TI, Tankshali RA, Goswami JA, Shah JS, Jetly DH, Kobawala TP, Patel KC, Shukla SN, Shah PM, *et al.* (2007). Molecular alterations in oral carcinogenesis: significant risk predictors in malignant transformation and tumor progression. *Int J Biol Markers* **22**, 132-143.

[135]   Mashberg A, and Samit AM (1989). Early detection, diagnosis, and management of oral and oropharyngeal cancer. *CA Cancer J Clin* **39**, 67-88.

[136]   Ludwig JA, and Weinstein JN (2005). Biomarkers in cancer staging, prognosis and treatment selection. *Nat Rev Cancer* **5**, 845-856.

[137]   Hornick JL, and Fletcher CD (2007). The role of KIT in the management of patients with gastrointestinal stromal tumors. *Hum Pathol* **38**, 679-687.

[138]   Guppy AE, and Rustin GJ (2002). CA125 response: can it replace the traditional response criteria in ovarian cancer? *Oncologist* **7**, 437-443.

[139]   Themelis G, Yoo JS, and Ntziachristos V (2008). Multispectral imaging using multiple-bandpass filters. *Optics letters* **33**, 1023-1025.

[140]   Atkins D, Reiffen KA, Tegtmeier CL, Winther H, Bonato MS, and Storkel S (2004). Immunohistochemical detection of EGFR in paraffin-embedded tumor tissues: variation in staining intensity due to choice of fixative and storage time of tissue sections. *J Histochem Cytochem* **52**, 893-901.

[141]   Mydlarz WK, Hennessey PT, and Califano JA (2010). Advances and Perspectives in the Molecular Diagnosis of Head and Neck Cancer. *Expert Opin Med Diagn* **4**, 53-65.

[142]   Rubin Grandis J, Melhem MF, Barnes EL, and Tweardy DJ (1996). Quantitative immunohistochemical analysis of transforming growth factor-alpha and epidermal growth factor receptor in patients with squamous cell carcinoma of the head and neck. *Cancer* **78**, 1284-1292.

[143]   Srinivasan M, and Jewell SD (2001). Evaluation of TGF-alpha and EGFR expression in oral leukoplakia and oral submucous fibrosis by quantitative immunohistochemistry. *Oncology* **61**, 284-292.

[144]   Kannan S, Chandran GJ, Balaram P, Chidambaram S, and Nair MK (1996). Potential biological markers for the staging of tumor progression in oral mucosa: a multivariate analysis. *Int J Biol Markers* **11**, 67-76.

[145]   Rubin Grandis J, Tweardy DJ, and Melhem MF (1998). Asynchronous modulation of transforming growth factor alpha and epidermal growth factor receptor protein expression in progression of premalignant lesions to head and neck squamous cell carcinoma. *Clin Cancer Res* **4**, 13-20.

[146]   Mellanen P, Minn H, Grenman R, and Harkonen P (1994). Expression of glucose transporters in head-and-neck tumors. *Int J Cancer* **56**, 622-629.

[147]   Kunkel M, Moergel M, Stockinger M, Jeong JH, Fritz G, Lehr HA, and Whiteside TL (2007). Overexpression of GLUT-1 is associated with resistance to radiotherapy and adverse prognosis in squamous cell carcinoma of the oral cavity. *Oral Oncol* **43**, 796-803.

[148]   Ayala FR, Rocha RM, Carvalho KC, Carvalho AL, da Cunha IW, Lourenco SV, and Soares FA (2010). GLUT1 and GLUT3 as potential prognostic markers for Oral Squamous Cell Carcinoma. *Molecules* **15**, 2374-2387.

[149]   Tian M, Zhang H, Nakasone Y, Mogi K, and Endo K (2004). Expression of Glut-1 and Glut-3 in untreated oral squamous cell carcinoma compared with FDG accumulation in a PET study. *Eur J Nucl Med Mol Imaging* **31**, 5-12.

[150]   Ohba S, Fujii H, Ito S, Fujimaki M, Matsumoto F, Furukawa M, Yokoyama J, Kusunoki T, Ikeda K, and Hino O (2010). Overexpression of GLUT-1 in the invasion front is associated with depth of oral squamous cell carcinoma and prognosis. *J Oral Pathol Med* **39**, 74-78.

[151]   Sheth RA, Josephson L, and Mahmood U (2009). Evaluation and clinically relevant applications of a fluorescent imaging analog to fluorodeoxyglucose positron emission tomography. *J Biomed Opt* **14**, 064014.

[152]   Nitin N, Carlson AL, Muldoon T, El-Naggar AK, Gillenwater A, and Richards-Kortum R (2009). Molecular imaging of glucose uptake in oral neoplasia following topical application of fluorescently labeled deoxy-glucose. *Int J Cancer* **124**, 2634-2642.

[153]   Atkins D, Reiffen KA, Tegtmeier CL, Winther H, Bonato MS, and Storkel S (2004). Immunohistochemical detection of EGFR in paraffin-embedded tumor tissues: variation in staining intensity due to choice of fixative and storage time of tissue sections. *The journal of histochemistry and cytochemistry : official journal of the Histochemistry Society* **52**, 893-901.

[154]   Li SJ, Guo W, Ren GX, Huang G, Chen T, and Song SL (2008). Expression of Glut-1 in primary and recurrent head and neck squamous cell carcinomas, and compared with 2-[18F]fluoro-2-deoxy-D-glucose accumulation in positron emission tomography. *Br J Oral Maxillofac Surg* **46**, 180-186.

[155]   Rethman MP, Carpenter W, Cohen EE, Epstein J, Evans CA, Flaitz CM, Graham FJ, Hujoel PP, Kalmar JR, Koch WM, *et al.* (2010). Evidence-based

clinical recommendations regarding screening for oral squamous cell carcinomas. *J Am Dent Assoc* **141**, 509-520.

[156]   Modjtahedi H, and Essapen S (2009). Epidermal growth factor receptor inhibitors in cancer treatment: advances, challenges and opportunities. *Anticancer Drugs* **20**, 851-855.

[157]   Rogers SJ, Box C, Chambers P, Barbachano Y, Nutting CM, Rhys-Evans P, Workman P, Harrington KJ, and Eccles SA (2009). Determinants of response to epidermal growth factor receptor tyrosine kinase inhibition in squamous cell carcinoma of the head and neck. *J Pathol* **218**, 122-130.

[158]   Hickinson DM, Marshall GB, Beran GJ, Varella-Garcia M, Mills EA, South MC, Cassidy AM, Acheson KL, McWalter G, McCormack RM, *et al.* (2009). Identification of biomarkers in human head and neck tumor cell lines that predict for in vitro sensitivity to gefitinib. *Clin Transl Sci* **2**, 183-192.

[159]   Sharafinski ME, Ferris RL, Ferrone S, and Grandis JR Epidermal growth factor receptor targeted therapy of squamous cell carcinoma of the head and neck. *Head Neck* **32**, 1412-1421.

[160]   Hamakawa H, Nakashiro K, Sumida T, Shintani S, Myers JN, Takes RP, Rinaldo A, and Ferlito A (2008). Basic evidence of molecular targeted therapy for oral cancer and salivary gland cancer. *Head Neck* **30**, 800-809.

[161]   Kondo N, Tsukuda M, Ishiguro Y, Kimura M, Fujita K, Sakakibara A, Takahashi H, Toth G, and Matsuda H (2010). Antitumor effects of lapatinib (GW572016), a dual inhibitor of EGFR and HER-2, in combination with cisplatin or paclitaxel on head and neck squamous cell carcinoma. *Oncol Rep* **23**, 957-963.

[162]   Basavaraj C, Sierra P, Shivu J, Melarkode R, Montero E, and Nair P (2010). Nimotuzumab with chemoradiation confers a survival advantage in treatment-naive head and neck tumors over expressing EGFR. *Cancer Biol Ther* **10**, 673-681.

[163]   Williams MD (2010). Integration of biomarkers including molecular targeted therapies in head and neck cancer. *Head Neck Pathol* **4**, 62-69.

[164]   Prado SM, Cedrun JL, Rey RL, Villaamil VM, Garcia AA, Ayerbes MV, and Aparicio LA (2010). Evaluation of COX-2, EGFR, and p53 as biomarkers of non-dysplastic oral leukoplakias. *Exp Mol Pathol* **89**, 197-203.

[165]   Bentzen SM, Atasoy BM, Daley FM, Dische S, Richman PI, Saunders MI, Trott KR, and Wilson GD (2005). Epidermal growth factor receptor expression in pretreatment biopsies from head and neck squamous cell carcinoma as a predictive factor for a benefit from accelerated radiation therapy in a randomized controlled trial. *J Clin Oncol* **23**, 5560-5567.

[166]   Suwinski R, Jaworska M, Nikiel B, Grzegorz W, Bankowska-Wozniak M, Wojciech M, Krzysztof S, and Dariusz L (2010). Predicting the effect of accelerated fractionation in postoperative radiotherapy for head and neck cancer based on molecular marker profiles: data from a randomized clinical trial. *Int J Radiat Oncol Biol Phys* **77**, 438-446.

[167]   Scarfone C, Lavely WC, Cmelak AJ, Delbeke D, Martin WH, Billheimer D, and Hallahan DE (2004). Prospective feasibility trial of radiotherapy target definition for head and neck cancer using 3-dimensional PET and CT imaging. *J Nucl Med* **45**, 543-552.

[168]   Al-Ibraheem A, Buck A, Krause BJ, Scheidhauer K, and Schwaiger M (2009). Clinical Applications of FDG PET and PET/CT in Head and Neck Cancer. *J Oncol* **2009**, 208725.

[169]   Martin RC, Fulham M, Shannon KF, Hughes C, Gao K, Milross C, Tin MM, Jackson M, Clifford A, Boyer MJ, *et al.* (2009). Accuracy of positron emission tomography in the evaluation of patients treated with chemoradiotherapy for mucosal head and neck cancer. *Head Neck* **31**, 244-250.

[170]   Vergez S, Delord JP, Thomas F, Rochaix P, Caselles O, Filleron T, Brillouet S, Canal P, Courbon F, and Allal BC (2010). Preclinical and clinical evidence that Deoxy-2-[18F]fluoro-D-glucose positron emission tomography with computed tomography is a reliable tool for the detection of early molecular responses to erlotinib in head and neck cancer. *Clin Cancer Res* **16**, 4434-4445.

[171]   Ito K, Yokoyama J, Kubota K, Morooka M, Shiibashi M, and Matsuda H (2010). 18F-FDG versus 11C-choline PET/CT for the imaging of advanced head and neck cancer after combined intra-arterial chemotherapy and radiotherapy: the time period during which PET/CT can reliably detect non-recurrence. *Eur J Nucl Med Mol Imaging* **37**, 1318-1327.

[172]   de Bree R, van der Putten L, Brouwer J, Castelijns JA, Hoekstra OS, and Leemans CR (2009). Detection of locoregional recurrent head and neck cancer after (chemo)radiotherapy using modern imaging. *Oral Oncol* **45**, 386-393.

[173]   Zundel MT, Michel MA, Schultz CJ, Maheshwari M, Wong SJ, Campbell BH, Massey BL, Blumin J, Wilson JF, and Wang D (2011). Comparison of Physical Examination and Fluorodeoxyglucose Positron Emission Tomography/Computed Tomography 4-6 Months After Radiotherapy to Assess Residual Head-and-Neck Cancer. *Int J Radiat Oncol Biol Phys*.

[174]   Ahsan A, Hiniker SM, Ramanand SG, Nyati S, Hegde A, Helman A, Menawat R, Bhojani MS, Lawrence TS, and Nyati MK (2010). Role of epidermal growth factor receptor degradation in cisplatin-induced cytotoxicity in head and neck cancer. *Cancer Res* **70**, 2862-2869.

[175]   Nouri AM, Thompson C, Cannell H, Symes M, Purkiss S, and Amirghofran Z (2000). Profile of epidermal growth factor receptor (EGFr) expression in human malignancies: effects of exposure to EGF and its biological influence on established human tumour cell lines. *Int J Mol Med* **6**, 495-500.

[176]   Group USCSW (2009) (U.S. Department of Health and Human Services, Centers for Disease Control and Prevention and National Cancer Institute, Atlanta).

[177]   Kennedy RJ, Bradley J, Parks RW, and Kirk SJ (2001). Prospective evaluation of the morbidity of axillary clearance for breast cancer (Br J Surg 2001; 88: 114-7). *Br J Surg* **88**, 891.

[178]   Kwan W, Jackson J, Weir LM, Dingee C, McGregor G, and Olivotto IA (2002). Chronic arm morbidity after curative breast cancer treatment: prevalence and impact on quality of life. *J Clin Oncol* **20**, 4242-4248.

[179]   Engel J, Kerr J, Schlesinger-Raab A, Sauer H, and Holzel D (2003). Axilla surgery severely affects quality of life: results of a 5-year prospective study in breast cancer patients. *Breast Cancer Res Treat* **79**, 47-57.

[180]   Norman SA, Localio AR, Potashnik SL, Simoes Torpey HA, Kallan MJ, Weber AL, Miller LT, Demichele A, and Solin LJ (2009). Lymphedema in breast cancer survivors: incidence, degree, time course, treatment, and symptoms. *J Clin Oncol* **27**, 390-397.

[181]   Albertini JJ, Lyman GH, Cox C, Yeatman T, Balducci L, Ku N, Shivers S, Berman C, Wells K, Rapaport D, *et al.* (1996). Lymphatic mapping and sentinel node biopsy in the patient with breast cancer. *JAMA* **276**, 1818-1822.

[182]   Krag D, Weaver D, Ashikaga T, Moffat F, Klimberg VS, Shriver C, Feldman S, Kusminsky R, Gadd M, Kuhn J, *et al.* (1998). The sentinel node in breast cancer--a multicenter validation study. *N Engl J Med* **339**, 941-946.

[183]   McMasters KM, Giuliano AE, Ross MI, Reintgen DS, Hunt KK, Byrd DR, Klimberg VS, Whitworth PW, Tafra LC, and Edwards MJ (1998). Sentinel-lymph-node biopsy for breast cancer--not yet the standard of care. *N Engl J Med* **339**, 990-995.

[184]   Orr RK, Hoehn JL, and Col NF (1999). The learning curve for sentinel node biopsy in breast cancer: practical considerations. *Arch Surg* **134**, 764-767.

[185]   Veronesi U, Paganelli G, Galimberti V, Viale G, Zurrida S, Bedoni M, Costa A, de Cicco C, Geraghty JG, Luini A, *et al.* (1997). Sentinel-node biopsy to avoid axillary dissection in breast cancer with clinically negative lymph-nodes. *Lancet* **349**, 1864-1867.

[186]   Veronesi U, Paganelli G, Viale G, Galimberti V, Luini A, Zurrida S, Robertson C, Sacchini V, Veronesi P, Orvieto E, *et al.* (1999). Sentinel lymph node biopsy and axillary dissection in breast cancer: results in a large series. *J Natl Cancer Inst* **91**, 368-373.

[187]   Lee A, Krishnamurthy S, Sahin A, Symmans WF, Hunt K, and Sneige N (2002). Intraoperative touch imprint of sentinel lymph nodes in breast carcinoma patients. *Cancer* **96**, 225-231.

[188]   Gmitro AF, and Aziz D (1993). Confocal microscopy through a fiber-optic imaging bundle. *Opt Lett* **18**, 565.

[189]   Flusberg BA, Cocker ED, Piyawattanametha W, Jung JC, Cheung EL, and Schnitzer MJ (2005). Fiber-optic fluorescence imaging. *Nat Methods* **2**, 941-950.

[190]   Ferguson LR, and Denny WA (1991). The genetic toxicology of acridines. *Mutat Res* **258**, 123-160.

[191]   Edlow DW, and Carter D (1973). Heterotopic epithelium in axillary lymph nodes: report of a case and review of the literature. *Am J Clin Pathol* **59**, 666-673.

[192]   Alvarez S, Anorbe E, Alcorta P, Lopez F, Alonso I, and Cortes J (2006). Role of sonography in the diagnosis of axillary lymph node metastases in breast cancer: a systematic review. *AJR Am J Roentgenol* **186**, 1342-1348.

[193]   de Boer M, van Dijck JA, Bult P, Borm GF, and Tjan-Heijnen VC Breast cancer prognosis and occult lymph node metastases, isolated tumor cells, and micrometastases. *J Natl Cancer Inst* **102**, 410-425.

[194]   Gimbergues P, Dauplat MM, Durando X, Abrial C, Le Bouedec G, Mouret-Reynier MA, Cachin F, Kwiatkowski F, Tchirkov A, Dauplat J, *et al.* Intraoperative imprint cytology examination of sentinel lymph nodes after neoadjuvant chemotherapy in breast cancer patients. *Ann Surg Oncol* **17**, 2132-2137.

[195]   Crippa F, Gerali A, Alessi A, Agresti R, and Bombardieri E (2004). FDG-PET for axillary lymph node staging in primary breast cancer. *Eur J Nucl Med Mol Imaging* **31 Suppl 1**, S97-102.

[196]   Pramanik M, Song KH, Swierczewska M, Green D, Sitharaman B, and Wang LV (2009). In vivo carbon nanotube-enhanced non-invasive photoacoustic mapping of the sentinel lymph node. *Phys Med Biol* **54**, 3291-3301.

[197]   Song KH, Kim C, Maslov K, and Wang LV (2009). Noninvasive in vivo spectroscopic nanorod-contrast photoacoustic mapping of sentinel lymph nodes. *Eur J Radiol* **70**, 227-231.

[198]   Boughey JC, Moriarty JP, Degnim AC, Gregg MS, Egginton JS, and Long KH Cost modeling of preoperative axillary ultrasound and fine-needle aspiration to guide surgery for invasive breast cancer. *Ann Surg Oncol* **17**, 953-958.

[199]   Ananta JS, Godin B, Sethi R, Moriggi L, Liu X, Serda RE, Krishnamurthy R, Muthupillai R, Bolskar RD, Helm L, *et al.* (2010). Geometrical confinement of gadolinium-based contrast agents in nanoporous particles enhances T1 contrast. *Nature nanotechnology* **5**, 815-821.

[200]   Fass L (2008). Imaging and cancer: a review. *Molecular oncology* **2**, 115-152.

[201]   Weissleder R, and Pittet MJ (2008). Imaging in the era of molecular oncology. *Nature* **452**, 580-589.

[202]   Marti-Bonmati L, Sopena R, Bartumeus P, and Sopena P (2010). Multimodality imaging techniques. *Contrast media & molecular imaging* **5**, 180-189.

[203]   Kircher MF, Mahmood U, King RS, Weissleder R, and Josephson L (2003). A multimodal nanoparticle for preoperative magnetic resonance imaging and intraoperative optical brain tumor delineation. *Cancer research* **63**, 8122-8125.

[204]   Nam T, Park S, Lee SY, Park K, Choi K, Song IC, Han MH, Leary JJ, Yuk SA, Kwon IC, *et al.* (2010). Tumor targeting chitosan nanoparticles for dual-modality optical/MR cancer imaging. *Bioconjugate chemistry* **21**, 578-582.

[205]   Koyama Y, Talanov VS, Bernardo M, Hama Y, Regino CA, Brechbiel MW, Choyke PL, and Kobayashi H (2007). A dendrimer-based nanosized contrast agent dual-labeled for magnetic resonance and optical fluorescence imaging to localize the sentinel lymph node in mice. *Journal of magnetic resonance imaging : JMRI* **25**, 866-871.

[206]   Shan L, Wang S, Sridhar R, Bhujwalla ZM, and Wang PC (2007). Dual probe with fluorescent and magnetic properties for imaging solid tumor xenografts. *Molecular imaging : official journal of the Society for Molecular Imaging* **6**, 85-95.

[207]   Sitharaman B, Kissell KR, Hartman KB, Tran LA, Baikalov A, Rusakova I, Sun Y, Khant HA, Ludtke SJ, Chiu W, *et al.* (2005). Superparamagnetic gadonanotubes are high-performance MRI contrast agents. *Chemical communications*, 3915-3917.

[208]   Tasciotti E, Liu X, Bhavane R, Plant K, Leonard AD, Price BK, Cheng MM, Decuzzi P, Tour JM, Robertson F, *et al.* (2008). Mesoporous silicon particles as a multistage delivery system for imaging and therapeutic applications. *Nature nanotechnology* **3**, 151-157.

[209]   Hsiung PL, Hardy J, Friedland S, Soetikno R, Du CB, Wu AP, Sahbaie P, Crawford JM, Lowe AW, Contag CH, *et al.* (2008). Detection of colonic

dysplasia in vivo using a targeted heptapeptide and confocal microendoscopy. *Nature medicine* **14**, 454-458.

[210]   Giuliano AE, Hunt KK, Ballman KV, Beitsch PD, Whitworth PW, Blumencranz PW, Leitch AM, Saha S, McCall LM, and Morrow M (2011). Axillary dissection vs no axillary dissection in women with invasive breast cancer and sentinel node metastasis: a randomized clinical trial. *JAMA : the journal of the American Medical Association* **305**, 569-575.